METAL-INSULATOR-SEMICONDUCTOR TUNNEL JUNCTIONS AND THEIR APPLICATION TO PHOTOVOLTAIC ENERGY CONVERSION

by

C NICHOLAS GARRY TARR

B.Sc., The University of British Columbia, 1977

A THESIS SUBMITTED IN PARTIAL FULFILMENT OF

THE REQUIREMENTS FOR THE DEGREE OF

DOCTOR OF PHILOSOPHY

in

THE FACULTY OF GRADUATE STUDIES

Department of Electrical Engineering

We accept this thesis as conforming

to the required standard

THE UNIVERSITY OF BRITISH COLUMBIA

May, 1981

In presenting this thesis in partial fulfilment of the requirements for an advanced degree at the University of British Columbia, I agree that the Library shall make it freely available for reference and study. I further agree that permission for extensive copying of this thesis for scholarly purposes may be granted by the head of my department or by his or her representatives. It is understood that copying or publication of this thesis for financial gain shall not be allowed without my written permission.

Department of Electrical Engineering

The University of British Columbia
2075 Wesbrook Place
Vancouver, Canada
V6T 1W5

Date July 7, 1981

ABSTRACT

This thesis is concerned primarily with an experimental and theoretical investigation of the properties of the metal-insulator-semiconductor (MIS) tunnel junction. Particular emphasis is placed on those properties which might be of use in the production of photovoltaic cells. The MIS junctions studied are divided into two basic classes: those in which the semiconductor surface is depleted or strongly inverted at equilibrium, and those in which the surface is accumulated at equilibrium. Junctions falling in the former category are termed positive barriers, while those in the latter group are termed negative barriers.

Recent theoretical studies have predicted that it should be possible to form positive barrier MIS junctions in which the dark current flow at moderate forward bias is dominated by the injection of minority carriers into the bulk semiconductor. This prediction is quite remarkable, in that it appears to contradict the abundant experimental evidence indicating that the dark current in non-ideal Schottky diodes is dominated by majority carrier thermionic emission. In this thesis two independent experiments providing the first incontrovertible evidence for the existence of minority carrier MIS diodes are reported. The first of these experiments involved the measurement of the current-voltage characteristics of Al-SiO_x-pSi diodes at various temperatures. From these measurements, an activation energy describing the temperature dependence of the dark current was extracted. This activation energy was found to agree exactly with that expected for a minority carrier injection-diffusion current, and to be significantly larger than that possible for a majority carrier thermionic emission current. In the second experiment, it was shown that an alloyed aluminum back surface field region could be used

to enhance the open-circuit voltages of Al-SiO_x-pSi solar cells. This demonstration that a modification to the rear surface of an MIS solar cell could alter the cell open-circuit voltage provided further irrefutable evidence for the existence of minority carrier MIS diodes.

Negative barrier MIS junctions do not function as rectifiers. Instead, these junctions are of use in forming low-resistance contacts to semiconductors. A simple analytic model of current flow in the negative barrier MIS junction is developed here. This model predicts that with a suitable choice of insulator thickness and barrier metal work function, it should be possible to form a negative barrier MIS contact which presents a very low effective surface recombination velocity to minority carriers, yet which offers negligible impedance to the flow of majority carriers. The minority carrier reflecting properties of the negative barrier MIS junction were demonstrated experimentally by incorporating this structure as the back contact in induced back surface field solar cells. Induced back surface field cells were successfully fabricated on both n- and p-type silicon. For both types of substrate, it was found that the minority carrier reflecting negative barrier MIS back contact could provide an enhancement in cell open-circuit voltage comparable to that obtained with a conventional back surface field formed by diffusion or alloying.

In addition to the studies of the MIS tunnel junction outlined above, this thesis includes a comprehensive investigation of the conditions under which the principle of dark current and photocurrent superposition provides an accurate description of the characteristics of homojunction solar cells. In particular, it is shown that the superposition principle should apply even if a significant fraction of both recombination and photogeneration occur in the depletion region. This contradicts the

conclusions drawn recently by other investigators. It is also found that the superposition principle may seriously overestimate the efficiency of cells fabricated on substrates with very poor lifetimes and low mobilities, a point which had not been appreciated previously.

TABLE OF CONTENTS

PAGE:

PAGE:

LIST OF TABLES

LIST OF FIGURES

ACKNOWLEDGEMENT

The research program described in this thesis could never have been completed without the help of many others. I am particularly grateful for the assistance of Peter A. Iles of Applied Solar Energy Corporation, who supplied the substrates used in many of the experiments. Special thanks are also due to my supervisor, Prof. David L. Pulfrey, for his enthusiastic encouragement throughout the project. Numerous discussions with fellow graduate students Daniel S. Camporese, Timothy P. Lester, Jürgen K. Kleta and David J. Smith, and with Prof. Lawrence Young, helped refine experimental techniques and clarify the theory of the MIS junction. Specialized circuitry for the measurement of solar cell characteristics designed and built by Alan Kot greatly simplified the task of data recording. Much of the vacuum system fixturing was built by technicians David G. Fletcher and Derek G. Daines. Finally, the financial support of the Natural Sciences and Engineering Research Council is gratefully acknowledged.

LIST OF SYMBOLS†

D_n (D_p)	electron (hole) diffusion coefficient [m^2s^{-1}]
E_C	energy of conduction band edge
E_V	energy of valence band edge
E_{FM}	metal fermi energy level
E_{Fn} (E_{Fp})	electron (hole) quasi-fermi energy level
h	Planck's constant [Js]
$\hbar$	$h/2\pi$
J_n (J_p)	electron (hole) current density [Am^{-2}]
k	Boltzmann's constant [$J\ °K^{-1}$]
L_n (L_p)	electron (hole) diffusion length [m]
n (p)	electron (hole) concentration [m^{-3}]
N_A	acceptor concentration [m^{-3}]
N_D	donor concentration [m^{-3}]
n_i	intrinsic carrier concentration [m^{-3}]
q	electron charge [C]
S_B	back surface recombination velocity [ms^{-1}]
S_F	front surface recombination velocity [ms^{-1}]
T	absolute temperature [°K]
V	terminal voltage [V]
W	depletion region width [m]
ε	permittivity [Fm^{-1}]
ε_I	permittivity of insulating layer
ε_S	permittivity of semiconductor
μ_n (μ_p)	electron (hole) mobility [$m^2V^{-1}s^{-1}$]
τ_n (τ_p)	electron (hole) lifetime [s]

ψ	electrostatic potential	[V]
$\mathcal{E}$	electric field	[Vm^{-1}]

† includes only those symbols not defined in text

CHAPTER 1

INTRODUCTION

In the past decade the need to develop new energy supplies to replace rapidly diminishing oil and natural gas reserves has become the world's foremost technological problem. Although many alternative energy sources are available, perhaps none is more acceptable from an enviromental viewpoint than the direct generation of electricity from sunlight through the photovoltaic effect. Photovoltaic cells have supplied electrical energy to virtually all spacecraft ever launched, but the high cost of these devices has so far prevented their use for the generation of large amounts of electricity on Earth. In order to make photovoltaics economically competitive with coal-fired or fission plants for the generation of electricity on a massive scale, it is estimated that the cost of solar cells must be reduced by more than an order of magnitude from present levels [1-3]. If this cost reduction is to be brought about, a technology for solar cell production radically different from that now employed in industry must be developed. This new technology must incorporate both an inexpensive substrate and a simple means of forming the rectifying junction at which the photogenerated carriers are collected.

Virtually all solar cells produced commercially today are fabricated on single crystal semiconductor-grade silicon slices suitable for use in the microelectronics industry. The amount of energy consumed in the purification and crystallization of these high quality substrates is so large it has been estimated that a typical cell would have to generate electricity for over a dozen years just to repay the energy used to refine the silicon it contains [4]. Before large-scale photovoltaic power gen-

eration can become a reality, it is essential that an inexpensive substrate be developed on which solar cells of greater than 10% efficiency and with an energy payback time on the order of months can be fabricated. Although there has as yet been no single, dramatic breakthrough in the search for such a substrate, steady progress has been made in devising low-cost techniques for the refining and crystallization of silicon which do not require excessive energy inputs [5]. At present prospects appear good for the eventual development of an inexpensive silicon substrate capable of meeting the efficiency and energy payback-time goals outlined above. There is a fairly high probability that such a future low-cost "solar grade" silicon substrate will have a large-grained polycrystalline (so-called granular) structure.

Even if an inexpensive silicon substrate becomes available, significant reductions in solar cell fabrication costs will still be required to make photovoltaics competitive with conventional power generation technologies. All present day commercial silicon cells are homojunction devices -- that is, they contain a metallurgical junction formed between p- and n-type regions of the same semiconductor. The process of solid state diffusion is currently used to form this pn junction. The diffusion is normally carried out in quartz-tube furnaces at temperatures ranging from 850 to 1000°C. In order to avoid contamination of the silicon with unwanted impurities, all substrates must be subjected to elaborate cleaning procedures before they are exposed to these high temperatures. Due to this requirement for extreme cleanliness, and because it is a relatively slow and labor-intensive process, it is unlikely that solid state diffusion could be a viable means of junction formation for future high-throughput, low-cost cell production. Moreover, solid state diffusion

may prove to be incompatible with granular silicon substrates due to the preferential diffusion of dopants along grain boundaries, which leads to shorting of the cell [6]. Even if this problem is not encountered, exposure to the high temperatures necessary for diffusion invariably reduces minority carrier lifetimes in a substrate [7], and thus lowers the efficiency of the finished cell.

One promising alternative technique for solar cell fabrication involves the replacement of the diffused pn junction with a metal-semiconductor junction, or Schottky barrier. Schottky diodes are now routinely produced in the electronics industry by the deposition of metal onto clean silicon surfaces under high vacuum conditions. Since the metal deposition is carried out at or near room temperature, the complications associated with high temperature processing outlined above are avoided completely. Further, the technology of vacuum deposition is far more readily adapted to automated mass production than is solid state diffusion. Because of these inherent advantages, the possibility of utilizing Schottky barriers to form the rectifying junction in silicon solar cells has been given serious consideration in recent years [8].

Schottky barrier diodes formed on silicon substrates were studied intensively in the 1960's. By the end of the decade an essentially complete understanding of the mechanisms responsible for conduction in these devices had been achieved [9]. It was determined that under moderate forward bias the diode current is dominated by the flow of majority carriers from the semiconductor into the metal. For junctions formed on moderately doped substrates, this majority carrier flow was shown to be accurately described by Bethe's thermionic emission theory [10]. It was also established that at forward bias part of the diode current results from the

flow of minority carriers from the metal into the semiconductor. These minority carriers can either recombine in the depletion region or diffuse into the quasi-neutral base. Experiments performed by Yu and Snow revealed that under reverse bias or small forward bias depletion region recombination -generation processes often dominate the current flow in silicon Schottky diodes [11]. In contrast, a theoretical analysis undertaken by Scharfetter indicated that only a negligible fraction of the current flow should result from injected minority carriers diffusing into the base [12]. This prediction was later confirmed experimentally by Yu and Snow, who directly measured the magnitude of this minority carrier injection-diffusion current by constructing transistors with Schottky barrier emitters [13]. Yu and Snow found that the minority carrier injection ratio -- that is, the ratio of the minority carrier injection-diffusion current to the total diode current -- was less than 10^{-4} over the normal range of diode operation.

The electrical characteristics of Schottky barriers can be conveniently summarized by comparing the current flows in a Schottky diode with those in a one-sided diffused junction pn diode formed on an identical substrate. (In a one-sided pn diode the diffused surface layer, or emitter, is much more heavily doped than the substrate). At moderate forward bias the current in the pn diode is dominated by the flow of minority carriers supplied from the emitter into the depletion region and quasi-neutral base. Under the same bias conditions there is an identical minority carrier flow into the depletion region and base of the Schottky diode, except in this device these carriers are supplied through electron transfer between the minority carrier band and the metal. However, in the Schottky diode there exists an additional and far larger current component

arising from the emission of majority carriers from the semiconductor into the metal. This thermionic emission current has no counterpart in the homojunction device, so at a given forward bias the dark current density in the Schottky diode is far larger than in the pn diode. For reasons which will be made clear in Chapter 2, from this result it follows that the open-circuit voltage and hence the energy conversion efficiency of a Schottky barrier solar cell must always be substantially lower than that of a pn junction solar cell formed on a similar substrate [14].

In the early 1970's it was discovered empirically that the open-circuit voltages of silicon Schottky barrier solar cells could be greatly increased if a very thin oxide layer were deliberately introduced between the metal and the substrate to form a metal-insulator-semiconductor (MIS) junction. In particular, Anderson, Delahoy and Milano found that MIS solar cells formed by depositing chromium on p-type silicon oxidized for a few minutes at 600°C could give efficiencies and open-circuit voltages only slightly lower than those of typical diffused junction cells [15]. A Schottky barrier solar cell fabricated by conventional techniques on a p-type silicon substrate would, in contrast, have had an energy conversion efficiency close to zero.

A plausible explanation for the remarkably high efficiencies reported by Anderson *et al.* for their Cr-SiO_x-pSi solar cells was first provided in 1974 by Green, Shewchun and several co-workers at McMaster University. The McMaster group employed numerical methods to solve for the conduction characteristics of the MIS diode, assuming that current flows in these devices as a result of electrons tunnelling directly between the metal and the semiconductor bands [16,17]. The numerical

analysis was applied only to those MIS diodes formed on silicon substrates with silicon dioxide insulating layers, but a wide variety of metal work functions, insulator thicknesses, and substrate doping levels was considered. The most interesting results were obtained when the metal work function was selected to give strong inversion of the semiconductor surface at equilibrium. In such cases it was found that over the range from reverse bias to small forward bias the diode current would be dominated by the flow of carriers between the metal and the minority band in the semiconductor [16]. Within this bias range the MIS junction would thus be electrically equivalent to a one-sided metallurgical pn junction. MIS diodes in which the main component of current flow at moderate forward bias results from the injection of minority carriers into the semiconductor were termed minority carrier MIS, or minMIS, diodes.

The prospect of producing a junction with the electrical properties of a pn diode by the simple deposition of metal on silicon is of obvious importance not only in the development of photovoltaic power generation, but for the microelectronics industry as a whole. However, conclusive experimental support for the existence of minority carrier MIS diodes is clearly required. The suggestion that the introduction of a very thin, tunnellable interfacial insulating layer in a metal-semiconductor junction can somehow eliminate the thermionic emission current and thus allow minority carrier flows to dominate the diode characteristic appears paradoxical when it is recalled that most Schottky barriers contain an interfacial layer of native oxide unintentionally introduced during processing. In a typical fabrication procedure for commercial silicon Schottky diodes, the substrate is etched in hydrofluoric acid to remove all traces of oxide from the surface, and then quickly transferred in air to the vacuum

system used for metal deposition. Ellipsometry reveals that a new native oxide layer roughly 10 Å thick is formed almost immediately upon exposure of the etched silicon surface to the atmosphere [18], and thus incorporated into the junction. Despite the presence of this thin interfacial layer, there is overwhelming experimental evidence indicating that the dark current in silicon Schottky diodes is dominated by majority carrier thermionic emission. Indeed, the metal-emitter transistors which Yu and Snow employed in their minority carrier injection ratio measurements [13] were fabricated on chemically etched substrates, and so almost certainly contained interfacial native oxide layers.

Since the majority of Schottky diodes contain interfacial oxide layers, the distinction between these devices and MIS diodes may appear unclear at this point. For the moment, those junctions in which an interfacial layer is deliberately introduced between the metal and the semiconductor will be termed MIS junctions, while all other junctions between a metal and a semiconductor will be referred to as Schottky barriers. Schottky diodes containing an interfacial layer will be termed non-ideal. In Chapter 3 a more precise criterion for distinguishing between Schottky and MIS junctions is suggested. The insulator thickness in the MIS diodes considered here will always be small enough that appreciable tunnel currents can flow between the metal and the semiconductor; thick-insulator MOS capacitors constitute a completely different class of device.

By mid-1978, at the commencement of the research program described in this thesis, a substantial body of experimental data on MIS junctions had been published [19]. However, no incontrovertible evidence for the existence of minority carrier MIS diodes had ever been reported. The first goal of the present research program was therefore to establish unequiv-

ocally that minMIS diodes with properties suitable for photovoltaic energy conversion could in fact be made. The two independent experiments undertaken to accomplish this goal are described in Chapter 4. In the first of these experiments, the temperature dependence of the current-voltage characteristics of Al-SiO_x-pSi diodes formed on 10 Ωcm substrates was investigated [20]. This study revealed that over the bias range of interest for solar cell operation the dark current in these diodes is indeed dominated by the injection of minority carrier electrons from the metal into the semiconductor. The second experiment involved the fabrication of MIS solar cells on 10 Ωcm substrates incorporating back surface fields [21]. A back surface field is simply a high-low junction formed at the rear of a solar cell; the structure is frequently employed to increase the open-circuit voltage of commercial diffused-junction devices. For the Al-SiO_x-pSi cells examined here, the use of a back surface field was found to increase the open-circuit voltage by as much as 50 mV over the value recorded with an ohmic back contact. The fact that a modification to the rear surface of an MIS solar cell could produce such a dramatic change in open-circuit voltage provides further irrefutable evidence for the existence of minMIS diodes.

Chapter 4 closes with an investigation of the relationship between insulator thickness and electrical characteristics in Al-SiO_x-pSi solar cells. Particular attention is paid to the rather bizarre illuminated current-voltage characteristics of cells with relatively thick insulating layers, a feature which has been largely overlooked by other investigators. The results of this experiment are in reasonably good agreement with the predictions of the models presently used to describe the MIS tunnel junction. In addition, the data obtained may provide some guidance

in the design of practical MIS devices.

The theoretical background for the experiments described in Chapter 4 is presented in Chapters 2 and 3. In Chapter 3 a unified theory of current flow in Schottky barrier and MIS junctions is developed, drawing heavily on both the results Green et al. obtained through numerical analysis [16, 17, 22-25] and on earlier theoretical work by Card and Rhoderick [26-28]. The material presented in Chapter 3 differs from these earlier treatments in that purely analytic methods are used in the development of the theory, and that allowance is made for strong inversion of the semiconductor surface. (Although Card and Rhoderick chose an analytic approach, their results are valid only for the case in which the semiconductor surface is depleted). Chapter 3 includes the first detailed theoretical investigation of the properties of MIS solar cells with relatively thick insulating layers. It is found that the analytic model can explain the unusual illuminated current-voltage characteristics reported for thick-insulator MIS cells in Chapter 4.

Since all the experiments described in this thesis involve the use of MIS junctions in solar cells, Chapter 2 is devoted to a fundamental discussion of photovoltaic device theory. Particular emphasis is placed on the principle of dark current and photocurrent superposition, which states that the current flowing in an illuminated cell subject to a bias V is given by the algebraic sum of the short-circuit photocurrent and the current which would flow at bias V in the dark. This principle has served as the theoretical foundation of photovoltaics since the early 1950's [29]. Previous attempts to justify the superposition principle [30,31] are reviewed in Chapter 2, and found to contain serious flaws. In the course of correcting these flaws, a simple argument is developed establishing

the validity of the superposition principle for typical homojunction cells operated in unconcentrated sunlight [32,33]. The conclusions drawn in this analytic argument are then confirmed by direct numerical solution of the basic semiconductor equations for representative silicon and gallium arsenide solar cells. Chapter 2 thus makes an important contribution to present understanding of homojunction solar cell operation.

By depositing a low work function metal on an n-type silicon substrate, or a high work function metal on a p-type substrate, it is possible to form an MIS junction in which the semiconductor surface is accumulated at equilibrium. Junctions of this type will be referred to here as negative barrier MIS contacts, to distinguish them from conventional positive barrier Schottky and MIS junctions in which the semiconductor surface is depleted or inverted. It has long been recognized that negative barrier metal-semiconductor junctions should offer little resistance to current flow, and thus be of use in forming ohmic contacts to semiconductors [34]. In 1976 Green, Godfrey and Davies postulated that negative barrier MIS contacts could be produced which would present essentially no impedance to the flow of majority carriers, but which would have an extremely low effective surface recombination velocity for minority carriers [35]. Contacts of this type would thus have electrical characteristics analogous to those of metallurgical high-low junctions, and could therefore be used to form induced back surface field regions in solar cells. Experimentally, Green et al. found that negative barrier MIS junctions could provide low resistance ohmic contacts to silicon, but never observed the predicted induced back surface field action [36].

In Chapter 5, the first successful fabrication of minority carrier reflecting negative barrier MIS contacts is reported. As suggested by

Green et al. [35,36], evidence for the low effective surface recombination velocity of these junctions was obtained by employing them as back contacts in induced back surface field solar cells. The first experiment carried out in this area involved the use of negative barrier Mg-SiO_x-nSi back contacts to form induced back surface fields on P^+N cells with diffused front junctions [37]. Later, negative barrier platinum-MIS contacts were used to create induced back surface fields on p-type silicon substrates. In this latter experiment both diffused N^+P and Al-SiO_x-pSi minMIS front junctions were employed. For all the device structures considered it was found that the negative barrier MIS back contact could provide an enhancement in open-circuit voltage comparable to that obtained with a conventional back surface field formed by diffusion or alloying. Chapter 5 includes a simple theoretical analysis of current flow in the negative barrier MIS contact based on a straightforward extension of the results obtained in Chapter 3.

CHAPTER 2

PHOTOVOLTAIC DEVICE THEORY

This chapter is intended primarily to provide the fundamental theoretical background for the experiments on photovoltaic devices described in Chapters 4 and 5. However, it should be emphasized that the material on the superposition principle presented in Section 2.2 constitutes a significant advance in present understanding of homojunction solar cell operation, and is thus of importance in its own right. Section 2.1 offers a short introduction to the terminology used in the study of photovoltaics. Section 2.3 closes the chapter with a brief examination of the properties of back surface field structures.

2.1 Introduction to Photovoltaic Devices

A photovoltaic cell or solar cell is simply a large area photodiode which is normally operated to supply power to a load. The vast majority of cells produced today are planar N^+P devices formed by diffusing phosphorus into uniformly doped p-type silicon substrates. The heavily doped surface layer is customarily termed the emitter, while the bulk substrate is referred to as the base. Although silicon cells have been studied most intensively in the past and are the mainstay of the present photovoltaics industry, it should be noted that a variety of other semiconductors can be used for photovoltaic energy conversion [3].

The current-voltage characteristics of a typical commercial silicon solar cell exposed to terrestrial sunlight are shown in Fig. 2.1. Following convention, the axes have been oriented so that power output is obtained for operation in the first quadrant. The maximum power point (V_{mp}, J_{mp}) is defined as the operating point at which the power supplied

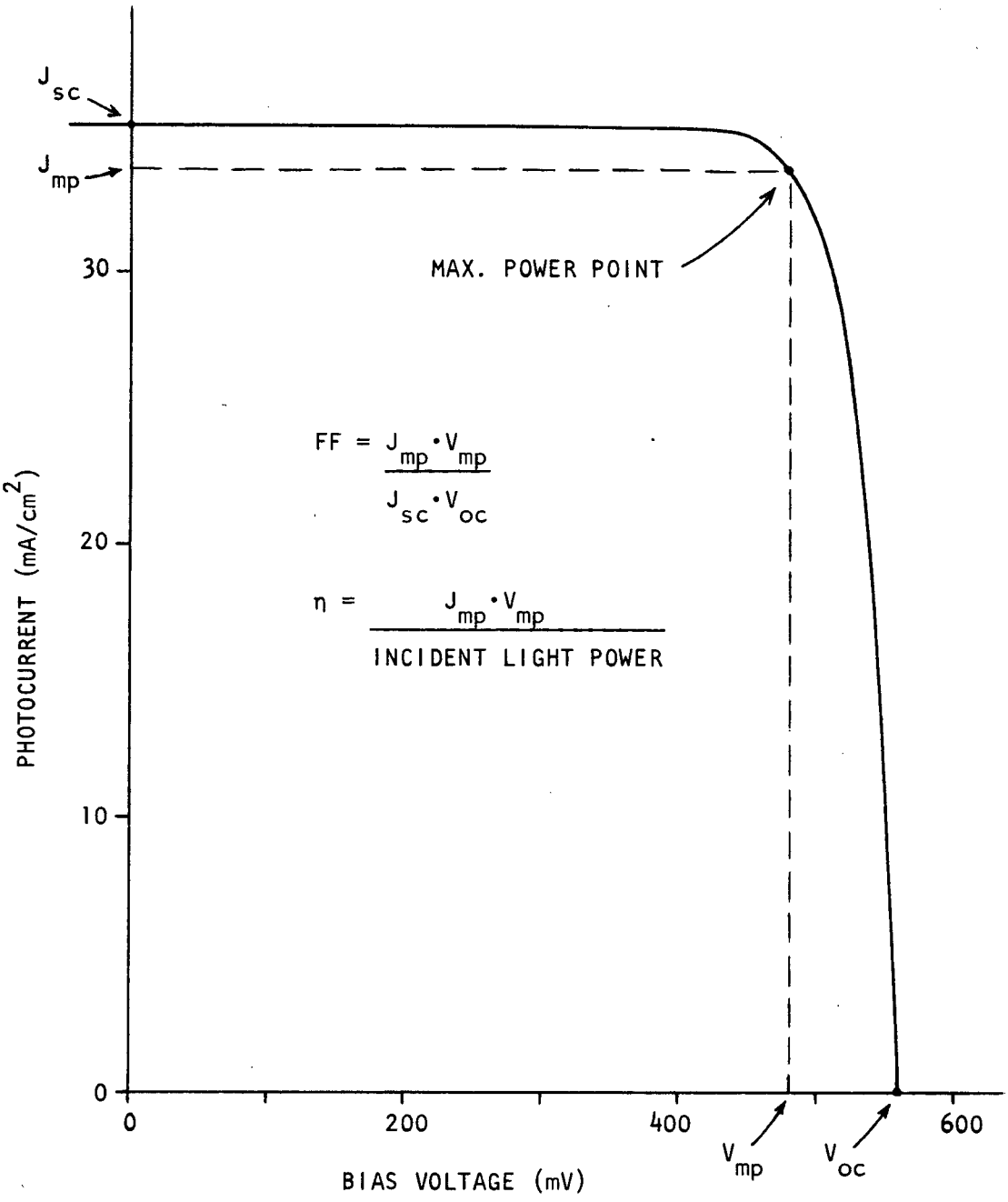

Figure 2.1 Current-voltage characteristic under one-sun illumination for a typical commercial silicon solar cell, illustrating the parameters used to describe cell performance.

by the cell is greatest. The performance of a solar cell is normally summarized in terms of four parameters: the short-circuit current J_{sc}, the open-circuit voltage V_{oc}, the fill factor FF and the energy conversion efficiency η. The fill factor is defined as the ratio of the maximum output power to the product of the short-circuit current and open-circuit voltage, and usually lies between 0.65 and 0.8 for a well designed device. η is simply the ratio of the maximum output power to the total incident light power.

For the purpose of measuring and comparing solar cell performance, various standardized representations of natural sunlight have been devised [38]. Cells designed for use in space are normally tested under "air mass zero" (AM0) illumination, which is equivalent to the solar irradiance just outside the atmosphere when the earth is at its mean distance from the sun. The choice of a standard illumination condition for testing terrestrial cells is more complicated, since sunlight is attenuated and filtered on its passage through the atmosphere. The performance of terrestrial cells is often measured under "air mass one" (AM1) illumination, which is obtained when AM0 sunlight is filtered by passage at normal incidence through an atmosphere of specified composition. The AM1 spectrum is thus meant to simulate typical illumination conditions when the sun is directly overhead. When the sun is not at the zenith, its light must traverse a longer path through the atmosphere before reaching the ground, and is therefore attenuated more severely. This situation is represented by spectra with higher air mass numbers. For example, AM2 illumination results when AM0 sunlight is passed through the standard atmosphere at an angle of 60° to the vertical, so that the path traversed by the light in the atmosphere is twice as long as when the

sun is overhead. Cells under test are always illuminated with light at normal incidence to their front surfaces. For cells used in conjunction with focussing mirrors or lenses, the ratio of the incident light intensity to that of unfocussed sunlight is termed the concentration ratio, or "number of suns". One-sun illumination thus refers to unconcentrated sunlight.

Assuming unit quantum efficiency, the photogeneration rate G at a distance x below the surface of an illuminated solar cell is given by [39]

$$G(x) = \int_0^{\lambda_{gap}} d\lambda \; [1 - R(\lambda)] \; M(\lambda) \; \alpha(\lambda) \; e^{-\alpha(\lambda)x} \qquad (2.1)$$

where $M(\lambda)$ is the incident photon flux spectral density, $R(\lambda)$ gives the fraction of incident photons reflected by the cell surface, and $\alpha(\lambda)$ is the absorption coefficient for the substrate material used. λ_{gap} is the wavelength of a photon with energy equal to the semiconductor bandgap. In order to minimize $R(\lambda)$, an antireflection coating is normally deposited on the front surface of the cell. The magnitude of $\alpha(\lambda)$ is determined largely by the band structure of the semiconductor. For direct bandgap materials such as gallium arsenide (GaAs), $\alpha(\lambda)$ is of the order of 10^5 cm^{-1} for visible light, and rises almost discontinuously as λ decreases through λ_{gap} [40]. In contrast, in an indirect gap material such as silicon, $\alpha(\lambda)$ rises much more slowly with decreasing wavelength, and is of the order of 10^4 cm^{-1} for visible light [40].

2.2 The Superposition Principle

The ultimate goal of any theoretical study of photovoltaic devices is to relate the terminal current-voltage characteristics of an illuminated device to its basic material properties. In the past, virtually

all theoretical investigations of solar cell performance have been based on the assumption that the current $J_L(V)$ flowing in an illuminated cell with a voltage V maintained across its terminals is given by

$$J_L(V) = J_{sc} - J_D(V) \tag{2.2}$$

where $J_D(V)$ is the current which would flow at bias V in the dark. Equation (2.2) is embodied in the simplified equivalent circuit commonly drawn for a solar cell, which models the illuminated cell by an ideal current source in parallel with a diode (Fig. 2.2). Equation (2.2) has been referred to variously as the "superposition principle" [32,33,41] or as the "shifting approximation" [31], the latter term arising from a graphical interpretation in which the illuminated J-V characteristic is obtained by shifting the dark characteristic through an amount J_{sc} along the current axis.

The superposition principle is a powerful tool in the design and analysis of photovoltaic cells, for when it applies the terminal current-voltage characteristics of a device are specified at any illumination level once the photocurrent corresponding to that illumination level and the single dark current-voltage characteristic are determined. For homojunction cells, well-known expressions are available for computation of the dark current, while an analytic technique for computing the photocurrent has been proposed by Hovel [39]. The superposition principle largely reduces the task of designing an optimally efficient cell to that of creating a diode structure which is effective in collecting photogenerated carriers, yet which has the minimum possible dark current. An example of the use of the superposition principle has already been

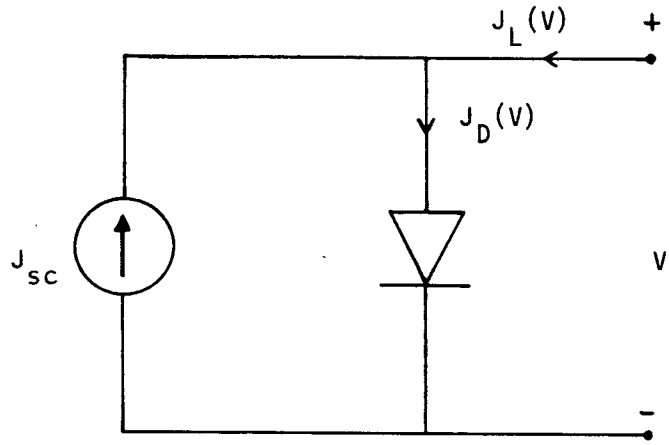

Figure 2.2 Simplified solar cell equivalent circuit.

encountered in Chapter 1. There it was noted that at a given forward bias the dark current flowing in a Schottky barrier diode is invariably orders of magnitude greater than that which would flow in a pn diode. Since it is expected that the short-circuit current in well-designed Schottky and pn junction solar cells will be comparable [8], it follows from (2.2) that a Schottky cell will have far lower maximum power point and open-circuit voltages than a pn cell, and will thus be much less efficient.

2.2.1 Previous Research on the Superposition Principle

In view of the fundamental importance of the superposition principle to the study of photovoltaics, it is remarkable that a rigorous investigation of the conditions required for (2.2) to apply was not carried out until very recently. Although the pioneers in the field of photovoltaics recognized that the parasitic shunt and series resistances associated with real cells could lead to deviations from (2.2), they simply assumed a posteriori that an "ideal" cell with no contact resistance and no shunt leakage paths could always be represented by the equivalent circuit of Fig. 2.2 [29]. Cummerow did derive an equation of the form of (2.2) from first principles [30], but this derivation was restricted to the case in which only negligible amounts of recombination and photogeneration occur in the depletion region. In most practical cells the junction is formed so close to the surface that a significant fraction of the photogeneration inevitably occurs in the depletion region.

In 1976 Lindholm, Fossum and Burgess [31] conducted the first comprehensive investigation of the range of validity of (2.2), and concluded that the superposition principle would apply to any homojunction solar cell provided three basic conditions were satisfied. The first of these conditions, that the internal shunt and series resistances associated

with the cell should be negligible, had been appreciated since the time of the first research on photovoltaics in the 1950's [29]. The second condition was that the minority carrier concentrations in the quasi-neutral regions of the cell should not exceed low injection levels -- that is, the minority carrier concentrations in these regions should be much less than the majority carrier concentration. This condition is usually satisfied for devices exposed to one-sun illumination, although high-level injection is frequently encountered in cells used in concentrator systems. The final condition was that the depletion region should not contribute substantially to both photogeneration and recombination.

The last condition listed above is of considerable importance, since it is likely to be violated in a device fabricated on a GaAs substrate. Of all semiconductors, this material has the highest potential photovoltaic conversion efficiency for operation in AM1 sunlight [1]. Because GaAs has a relatively wide bandgap, under normal operating conditions much of the recombination in a typical GaAs solar cell occurs in the depletion region [42]. Further, GaAs is a direct bandgap material, and so strongly absorbs all photons with energies greater than E_g. Since efficient GaAs homojunction cells have very shallow front junctions, it follows that a significant fraction of the total photogeneration must occur in the depletion region. In fact, the most efficient solar cells fabricated to date have been so-called "heteroface" devices incorporating a wide-bandgap $pGa_{1-x}Al_xAs$ "window" layer grown by epitaxy over an extremely shallow pGaAs-nGaAs homojunction [43], and for these cells the majority of photogeneration undoubtably occurs within the depletion region.

2.2.2 An Analytic Derivation of the Superposition Principle

In this subsection, a simple analytic argument establishing the validity of (2.2) for typical homojunction solar cells is developed. Following Lindholm et al. [31] and Cummerow [30], the argument is based on a straightforward extension of Shockley's seminal analysis of current flow in the pn diode [44]. Just as in these earlier treatments, it is assumed that the series resistance associated with the quasi-neutral regions is negligible, and that the minority carrier concentrations in these regions do not exceed low injection levels. However, whereas Lindholm et al. and Cummerow simply assumed without justification that the quasi-fermi energy levels are constant across the depletion region of an illuminated cell, this assumption is examined critically in subsection 2.2.3, and found to be grossly inaccurate in many situations. In the course of the analysis it is shown that the superposition principle can provide an excellent approximate description of cell characteristics even when the third necessary condition specified by Lindholm et al. does not apply -- that is, when the bulk of both photogeneration and recombination occur in the depletion region [32]. In subsection 2.2.4, support for the analytic argument is provided by direct numerical solution of the differential equations governing the current flows, carrier distributions and potentials within a solar cell. This numerical analysis is applied to both silicon and GaAs devices. In subsection 2.2.5, numerical analysis is used to show that the superposition principle may seriously overestimate the efficiency of cells fabricated on material with very poor minority carrier lifetimes and low mobilities, even if all three conditions set forth in [31] are satisfied [33]. This is not an unimportant point in view of the current interest in cells fabricated on

inexpensive, low-quality substrates.

The operation of any solar cell is governed by the five basic equations of semiconductor physics: the continuity equations, the current equations, and Poisson's equation [45]. Normally, only steady-state operation is of interest for solar cells. Further, only one-dimensional devices will be considered here. (Real three-dimensional cells are conventionally modelled by forming networks of idealized one-dimensional diode elements connected by lumped resistances representing, for example, the spreading resistance of a shallow diffused surface layer [46]). The basic equations are listed below in their steady-state, one-dimensional form.

Continuity Equations:

$$0 = (1/q)(dJ_n/dx) + G - U \tag{2.3}$$

$$0 = -(1/q)(dJ_p/dx) + G - U \tag{2.4}$$

Current Equations:

$$J_n = q\mu_n n\mathcal{E} + qD_n(dn/dx) \tag{2.5}$$

$$J_p = q\mu_p p\mathcal{E} - qD_p(dp/dx) \tag{2.6}$$

Poisson's Equation:

$$\mathcal{E} = -d\psi/dx; \qquad d^2\psi/dx^2 = -(q/\varepsilon)[N_D - n + p - N_A] \tag{2.7}$$

As Lindholm et al. [31] have pointed out, a cursory inspection of the basic equations reveals that the principle of dark current and photocurrent superposition can not be generally correct, at least in a strict

mathematical sense. When combined with appropriate boundary conditions at the surfaces of a cell, equations (2.3)-(2.7) can be thought of as a system specifying the terminal current J as a response to two excitations: the applied terminal voltage V and illumination. Since the basic equations are non-linear, the response to two excitations applied simultaneously will not in general be equal to the sum of the responses to the same excitations applied separately. Fortunately, the superposition principle provides an excellent approximate description of cell behaviour in many circumstances, even though it is not rigorously true.

Although the argument developed in this section is applicable to any planar homojunction solar cell, it is most easily presented in reference to a specific device structure. The structure considered here is a conventional N^+P diffused junction cell with the geometry of Fig. 2.3.

Before any progress can be made in solving the basic equations, boundary conditions must be imposed on n, p and ψ at the front and back faces of the cell. It is conventionally assumed that at the front surface the electron concentration is fixed at its thermal equilibrium value and the electron quasi-fermi level coincides with the fermi level in the metal contact to the emitter. Analogous boundary conditions are applied to the hole concentration and quasi-fermi level at the back surface. These two conditions automatically determine the electrostatic potential drop across the cell for any applied bias V. Further boundary conditions are imposed by specifying surface recombination velocities for minority carriers. At the front surface,

$$-J_p(x_F) = qS_F p_n'(x_F) \qquad (2.8)$$

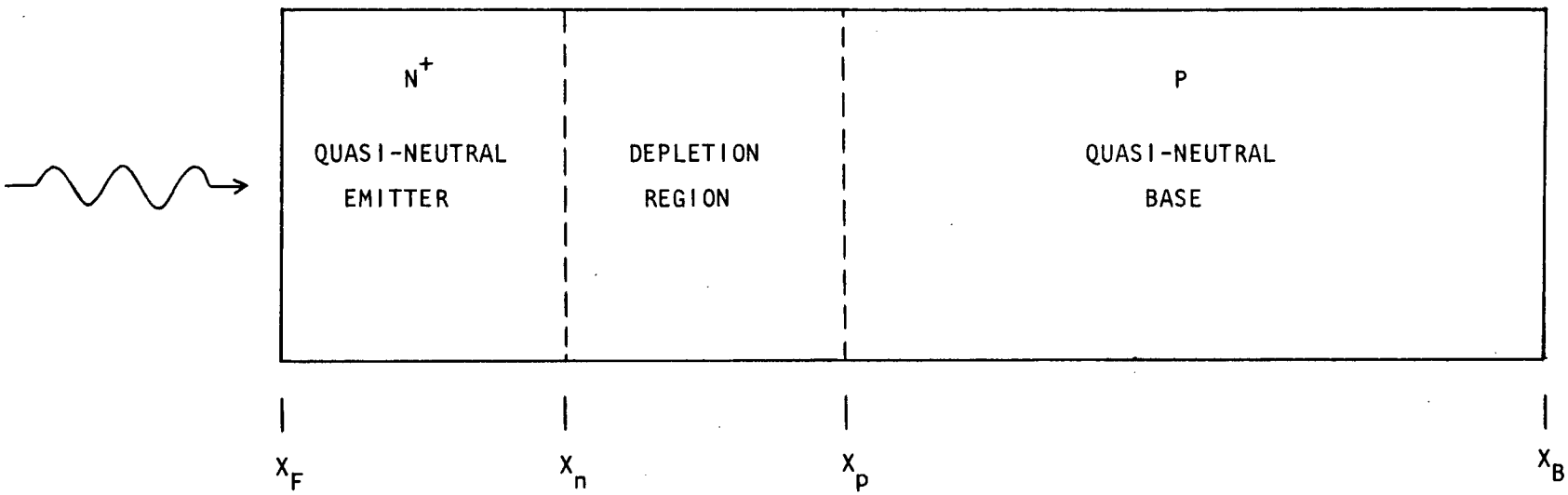

Figure 2.3 Geometry of N^+P solar cell.

while at the back surface

$$-J_n(x_B) = qS_B n_p'(x_B). \tag{2.9}$$

Frequently an ohmic contact is present at the back of the cell, in which case $S_B \to \infty$. (2.8) and (2.9) state that the minority carrier recombination rate at each surface is proportional to the excess minority carrier concentration there. This proportionality is essential if the superposition principle is to hold.

Following Shockley's method of analysis [44], the device of Fig. 2.3 has been divided into two quasi-neutral regions separated by a depletion or space-charge region. In the depletion region the concentration of ionized dopants is far greater than the concentration of free charge carriers, while in the quasi-neutral regions the charge of the ionized dopants is balanced almost exactly by that of the majority carriers. The boundaries between these regions are assumed to be abrupt. At equilibrium, there is essentially no electric field in the quasi-neutral base, but a large field exists in the quasi-neutral emitter as a result of the non-uniform doping profile there. In the low-level injection regime the application of a forward bias V to the cell is assumed to result in the reduction of the electrostatic potential drop across the depletion region by an amount V, while leaving the majority carrier and electric field distributions in the quasi-neutral regions unchanged.

Perhaps the most elegant way to describe the operation of a solar cell is in terms of the continuity principle, following the approach of Lindholm et al. [31]. In the steady state, the continuity principle holds that the current flowing through the terminals of a solar cell must equal

the difference between the total rate of photogeneration and the total rate of recombination in the device. That is,

$$J_L(V) = q \int_{cell} G(x)\, dx - q \int_{cell} U(x)\, dx \qquad (2.10)$$

where G(x) is the volume rate of photogeneration and U(x) the volume rate of recombination, including recombination at the front and back boundaries of the cell. (U(x) is defined here to account for the thermal generation of carriers, as well as recombination). Equation (2.10) simply specifies that in the steady state each photogenerated electron-hole pair must either recombine within the cell or contribute to current flow in the external circuit. From (2.10) it can be seen that the superposition principle will accurately describe the characteristics of a given cell if and only if the integral involving U can be split into a term which depends on the illumination level and not on V, and a term which depends on V but is independent of illumination.

U is, in general, a complicated function of the carrier concentrations n and p. However, within a quasi-neutral region under low-level injection conditions the recombination rate is controlled by the supply of minority carriers, and U therefore becomes proportional to the excess minority carrier concentration [47]. By definition, the proportionality constant is the reciprocal of the minority carrier lifetime τ. Moreover, in a quasi-neutral region the minority carrier current depends linearly on the excess minority carrier concentration for low-level injection, even if a built-in electric field is present due to non-uniform doping [31]. This allows the minority carrier current and continuity equations to be combined, yielding a single linear differential equation governing

the excess minority carrier distribution.

To take a specific example, in the uniformly doped quasi-neutral base region, the drift component in the electron current equation (2.5) can be ignored for low-level injection, so this equation becomes

$$J_n = qD_n(dn_p'/dx). \tag{2.11}$$

Combining (2.11) with the electron continuity equation (2.3), the following differential equation describing the excess electron distribution $n_p'(x)$ in the base is obtained:

$$d^2n_p'/dx^2 = n_p'/(D_n\tau_n) - G(x)/D_n . \tag{2.12}$$

In order to solve (2.12), it is necessary to specify boundary conditions on n_p' at the borders of the base. From (2.9) and (2.5), at the back contact

$$-D_n(dn_p'/dx) = S_Bn_p'(x_B). \tag{2.13}$$

Obtaining a boundary condition on n_p' at the border between the base and the depletion region presents a more difficult problem. In Shockley's analysis of current flow in the pn diode [44], the excess minority carrier concentrations at the boundaries between the depletion region and the quasi-neutral regions are found by assuming that the quasi-fermi energy levels for both carriers are constant across the depletion region. Although Shockley's analysis dealt only with devices operated in the dark, both Cummerow [30] and Lindholm et al. [31] applied this assumption

without qualification to the case of an illuminated solar cell, and added the further tacit assumption that the electrostatic potential barrier across the depletion region depends only on the bias V and not on the illumination level. Taken together, these two assumptions imply that at the boundary x_p between the depletion region and the quasi-neutral base

$$n_p'(x_p) = n_{p0}[\exp(qV/kT) - 1] \tag{2.14}$$

irrespective of the illumination level. Although it is possible to determine the excess electron distribution in the base by directly solving (2.12) with boundary conditions (2.13) and (2.14), $n_p'(x)$ can be found more easily by superposing the solutions to the following two systems:

System 1:

$$d^2n_p'/dx^2 = n_p'/(D_n\tau_n) \qquad \text{with B.C.'s (2.13) and (2.14)}$$

System 2:

$$d^2n_p'/dx^2 = n_p'/(D_n\tau_n) - G(x)/D_n \qquad \text{with B.C.'s (2.13) and } n_p'(x_p) = 0.$$

Clearly, the solution to the first system gives the excess electron distribution when a bias V is applied in the dark, while the solution to the second system is bias-independent. Recalling that U is proportional to n_p', it follows that the integral of U over the base can be split into two terms, with one term corresponding to the application of a bias V in the dark and the second term depending only on the illumination level.

A similar argument can be used to show that the integral of U over the quasi-neutral emitter can be split into strictly bias-dependent and strictly illumination-dependent terms. Since the non-uniform doping profile in this region gives rise to a large electric field, the drift term in the expression for the hole current can not be ignored. Writing the total hole concentration in the emitter as a sum of the equilibrium concentration and the excess concentration, the hole current equation (2.6) becomes

$$J_p = [-qD_p(dp_n'/dx) + q\mu_p \mathcal{E} p_n'] + [-qD_p(dp_{n0}/dx) + q\mu_p \mathcal{E} p_{n0}]. \quad (2.15)$$

The right hand term in square brackets in (2.15) is simply the value of the hole current at thermal equilibrium. The principle of detailed balance states that there can be no net hole current anywhere in the cell at equilibrium, so this term must equal zero. Substituting the left hand term in (2.15) into the hole continuity equation (2.4) gives the following differential equation governing the excess hole concentration in the emitter:

$$-p_n'[d(\mu_p \mathcal{E})/dx] - \mu_p \mathcal{E}(dp_n'/dx) + (dp_n'/dx)(dD_p/dx) \quad (2.16)$$
$$+ D_p(d^2p_n'/dx^2) + G(x) - p_n'/\tau_p = 0$$

Although the quantities μ_p, D_p, τ_p and $\mathcal{E}$ may all depend on position within the emitter, they should all be independent of p_n' in the low-level injection regime. (2.16) is therefore linear in the excess hole concentration. The boundary conditions on the hole concentration in the quasi-

neutral emitter are analogous to those on the electron concentration in the quasi-neutral base. At the front surface,

$$-\mu_p \mathcal{E} p_n' + D_p (dp_n'/dx) = S_F p_n'(x_F) \tag{2.17}$$

while at the boundary between the emitter and the depletion region

$$p_n'(x_n) = p_{n0}(x_n)[\exp(qV/kT) - 1] \, . \tag{2.18}$$

By analogy with the solution for the electron distribution in the base, the excess hole distribution in the emitter of a forward-biased, illuminated cell can be found by superposing the solutions to two special cases of (2.16). The first of these solutions is for G(x)=0 with boundary conditions (2.17) and (2.18), while the second solution is for non-zero G(x) with boundary condition (2.17) and the additional condition $p_n'(x_n)=0$. It should be noted that while an explicit solution for $n_p'(x)$ in the uniformly doped base can be obtained trivially, the solution of (2.16) for non-zero $\mathcal{E}$ represents a far more difficult mathematical problem [48].

To complete the evaluation of the integral of U over the cell, it is now necessary to examine the integral of U over the depletion region. In Cummerow's analysis [30], recombination in the depletion region was simply ignored. Lindholm *et al.* [31] noted that in the depletion region U is not linear in the excess carrier concentrations, and consequently concluded that within this region it would not in general be possible to split U into a term which depends only on the illumination level and a term which depends only on the applied bias. On these grounds it was further concluded that the superposition principle should apply

only to those devices in which the depletion region does not contribute significantly to both the photogeneration and recombination of carriers. However, this reasoning is not consistent with the use of Shockley's method [44] to obtain boundary conditions on the excess minority carrier concentrations at the edges of the depletion region. If it is assumed that the quasi-fermi energy levels and the electrostatic potential in the depletion region depend only on the bias V and not on the illumination level, then the carrier concentrations in this region must depend only on V. This in turn implies that for a given bias V the integral of U over the depletion region is independent of the illumination level.

Combining the conclusions drawn above regarding recombination in the quasi-neutral regions and the depletion region, it follows that the integral of U over the entire cell can be divided into strictly bias-dependent and strictly illumination-dependent terms. The current flowing in an illuminated cell is therefore given by

$$J_L(V) = J_{upc} - J_D(V) \tag{2.19}$$

where J_{upc} is a bias-independent photocurrent. In accordance with the terminology introduced by Lindholm et al. [31], the subscript "upc" stands for "uncompensated photocurrent". At this point the introduction of the symbol J_{upc} may seem redundant, since if (2.19) holds for all V, J_{upc} must be identical to J_{sc}. However, the distinction between J_{upc} and J_{sc} will prove useful in the remainder of this discussion. While J_{sc} is the current flowing in a real cell with the terminals shorted, J_{upc} is best thought of as a mathematical quantity defined by

$$J_{upc} = q \int_{x_F}^{x_B} G(x)\, dx \;-\; q \int_{x_F}^{x_n} U(x)\, dx \;-\; q \int_{x_p}^{x_B} U(x)\, dx \,. \quad (2.20)$$

In (2.20) the recombination rate U(x) is to be evaluated for boundary conditions $n_p'(x_p)=0$ and $p_n'(x_n)=0$ with photogeneration distribution G(x) appropriate to the illumination conditions under consideration.

Throughout the derivation of (2.19) it was assumed that the boundaries between the quasi-neutral regions and the depletion region do not move as the bias applied to the cell changes. This is, of course, not the case in a real cell, since the depletion region contracts as the bias V is increased. It might thus be expected that the photocurrent J_{upc} defined in (2.20) would have some slight bias dependence, since x_n and x_p are functions of V. For example, in the N^+P cell used as a model here, an increase in forward bias results in an increase in the width of the quasi-neutral base at the expense of the depletion region, while the width of the heavily-doped quasi-neutral emitter remains virtually unchanged. Thus in Fig. 2.3 x_p moves to the left while x_n is stationary. Now consider a fixed point A in the diode chosen so that x_p lies to the right of A for small forward bias and to the left of A for larger forward bias. In the former case A lies in the depletion region, and so virtually all carriers photogenerated at A are collected and contribute to J_{upc}. In the latter case A lies in the quasi-neutral base, but even so most of the carriers photogenerated at A will diffuse to the junction and be collected so long as A lies within an electron diffusion length of x_p. Thus J_{upc} should be essentially independent of bias as long as the change in the width of the depletion region with bias is small compared to a minority carrier diffusion length in the quasi-neutral base.

2.2.3 Quasi-Fermi Levels in the Depletion Region

The argument used to establish (2.19) was based on the twin assumptions that the electrostatic potential and the quasi-fermi energy levels in the depletion region of a solar cell are dependent only on the applied bias and not on the illumination level. The accuracy of the assumption on the electrostatic potential can be confirmed fairly easily. Provided that the series resistance associated with the quasi-neutral regions is negligible and that the minority carrier concentrations in these regions remain at low injection levels, the application of a forward bias V should result in the reduction of the junction electrostatic potential barrier by an amount V as well, regardless of the illumination level. Provided also that the free carrier concentrations in the depletion region are always negligible compared to the concentration of ionized dopants in that region, it follows that the depletion approximation should accurately describe the variation of the electrostatic potential across the junction for all illumination conditions.

The constancy of the quasi-fermi levels across the depletion region can best be checked by exploiting the relationship between the electron and hole currents and the gradients of these energy levels [49]; specifically,

$$\vec{J}_n = \mu_n n \vec{\nabla} E_{Fn} \tag{2.21}$$

and

$$\vec{J}_p = \mu_p p \vec{\nabla} E_{Fp} . \tag{2.22}$$

Qualitatively, (2.21) reveals that the gradient of E_{Fn} must be large

wherever J_n is large and n is small. Thus there will be a large drop in E_{Fn} across a region through which a large electron current flows and in which the electron concentration is small. Similar remarks apply to E_{Fp}.

Quantitatively, (2.21) and (2.22) can be used to compute the change in the quasi-fermi levels across any part of a device if accurate estimates for the currents and carrier concentrations in that region are available. In the case of a solar cell, it is possible to obtain a first estimate for the currents and carrier concentrations in the depletion region under given operating conditions by assuming that the two quasi-fermi levels are constant across this region and applying the analysis outlined above. The drops in the quasi-fermi levels across the depletion region, ΔE_{Fn} and ΔE_{Fp}, can then be estimated from (2.21) and (2.22). If the estimates for ΔE_{Fn} and ΔE_{Fp} calculated following this procedure are much smaller than kT, the assumption of constant quasi-fermi levels is self-consistent, and probably provides an accurate approximation to the actual solution to the basic equations. However, if the calculations suggest that large changes in E_{Fn} and E_{Fp} across the depletion region would be required to support the estimated electron and hole currents, the assumption of constant quasi-fermi levels in the depletion region is clearly untenable.

Equations (2.21) and (2.22) will now be used to investigate the behaviour of the quasi-fermi levels in the depletion region of an N^+P solar cell. The behaviour of the quasi-fermi levels when a forward bias is applied in the dark will be examined first, and then the effect of illumination will be considered.

A. Forward Bias in the Dark

Dark current in a forward-biased N^+P cell normally results from

recombination in either the depletion region or the quasi-neutral base. The magnitude of the injection-diffusion current resulting from recombination in the base is given by

$$J_d = q\sqrt{D_n}\, n_p'(x_p)/\sqrt{\tau_n} \ . \qquad (2.23)$$

To support an injection-diffusion current, electrons must flow all the way across the depletion region and enter the quasi-neutral base. On moving from the emitter across the depletion region towards the base the free electron concentration decreases by many orders of magnitude. Therefore, for this type of dark current, the electron concentration near the edge of the base is of greatest importance in determining ΔE_{Fn}. However, (2.23) states that J_d is proportional to $n_p'(x_p)$. Thus even though J_d increases exponentially with V, the electron concentration in the depletion region increases in step so that ΔE_{Fn} is roughly independent of bias. A similar result holds for the depletion region recombination current J_{rg}. A crude estimate for the magnitude of J_{rg} can be obtained by noting that the rate of carrier recombination is highest at the middle of the depletion region, near the point where the electron and hole concentrations are equal. If the maximum recombination rate is multiplied by the width W of the depletion region one arrives at the approximate formula [50]

$$J_{rg} \simeq q\, n_{n=p}\, W\, /(2\sqrt{\tau_n \tau_p}) \ . \qquad (2.24)$$

Here $n_{n=p}$ is the electron (or hole) concentration at the point where n=p. To support a depletion region recombination current it is only

necessary for electrons to travel from the emitter to the center of the depletion region, where most recombination takes place. Similarly, holes need only flow from the base to the zone near the center of the depletion region where the recombination rate is greatest. Thus the hole and electron currents are large only in those parts of the depletion region where the corresponding carrier concentrations are large as well. The drops in the quasi-fermi levels across the depletion region are therefore fixed primarily by the carrier concentrations at the place of maximum recombination, that is by $n_{n=p}$. Just as in the case of an injection-diffusion current, although J_{rg} increases exponentially with bias, $n_{n=p}$ increases proportionately, so that ΔE_{Fn} and ΔE_{Fp} are roughly bias independent.

B. Under Illumination

When an N^+P solar cell is forward-biased in the dark, electrons supplied from the emitter recombine with holes in the depletion region and in the base. Thus throughout the depletion region the electron flow is directed towards the base. To support this flow the electron quasi-fermi level must be slightly lower at the edge of the base than at the edge of the emitter. Therefore, at each point in the depletion region the electron concentration is actually slightly less than would be the case if E_{Fn} were precisely constant across this region. When the cell is exposed to light, at least some photogenerated electrons must flow from the base into the depletion region. This photogenerated electron current opposes the current due to electrons injected from the emitter, with the result that the net electron flow from the emitter to the base is smaller under illumination than in the dark. If the electron quasi-fermi level in the emitter is chosen as a reference point, it follows that everywhere in the depletion region of an illuminated, forward-biased cell E_{Fn} must

be higher than it was at the same forward bias in the dark. Therefore, throughout the depletion region the electron concentration must be greater in the light than it was at the same forward bias in the dark, assuming that the electrostatic potential depends only on the applied bias. A completely analogous argument can be developed to show that, for a given forward bias, the hole concentration everywhere in the depletion region must also be greater under illumination than in the dark. This increase in the concentration of free carriers in the depletion region must lead to an increased rate of recombination in that region. Also, the excess minority carrier concentrations at the boundaries of the quasi-neutral regions will be greater in the light than at the same forward bias in the dark. As a result, there will be more recombination in these regions than would be the case if the quasi-fermi levels were, in fact, constant across the depletion region. Thus for a given forward bias less current can be drawn from the cell terminals than predicted by (2.19), and so (2.19) must overestimate the energy conversion efficiency.

Although (2.19) is never strictly correct, it still provides an excellent approximate description of the characteristics of most real homojunction solar cells. (2.19) will be inaccurate only if at some bias point the carrier concentrations in the depletion region are significantly greater under illumination than in the dark and the total rate of recombination is comparable to the total rate of photogeneration. Whether or not this condition is realized in a given cell depends on the extent to which the carrier concentrations in the depletion region increase under illumination, and on the relationship between the carrier concentrations and the recombination rate.

It has been shown above that for a cell forward biased in the dark

the carrier flows and carrier concentrations in the depletion region both increase exponentially with bias, with the result that ΔE_{Fn} and ΔE_{Fp} are roughly bias independent. In contrast, in an illuminated solar cell large photocurrents flow across the depletion region even at short-circuit or low forward bias. Applying (2.21) and (2.22) in the quantitative manner suggested above, it can readily be shown that at low forward bias these photocurrents can not be supported unless E_{Fn} and E_{Fp} are shifted substantially from their positions in the dark. This result applies to essentially any device, regardless of the choice of substrate material or doping profile. Thus the assumption that E_{Fn} and E_{Fp} are constant across the depletion region is grossly in error at low forward bias. However, as the forward bias is increased the carrier concentrations in the depletion region rise, and so the drops in E_{Fn} and E_{Fp} across this region required to support the photocurrent decrease. If the bias is increased still further, eventually an operating point will be reached for which ΔE_{Fn} and ΔE_{Fp} are both small fractions of kT, and from this point on (2.19) will accurately describe the cell characteristics. For most homojunction cells, the bias point at which the quasi-fermi energy levels become effectively constant across the depletion region is reached when the total rate of recombination is still many orders of magnitude smaller than the total rate of photogeneration. If this is the case, then the fact that the quasi-fermi levels are not constant across the depletion region for operation at short-circuit or low forward bias will have no measureable effect on the accuracy of (2.19). Further, J_{upc} will be indistinguishable from J_{sc}, so (2.2) and (2.19) will be interchangeable.

If the drops in E_{Fn} and E_{Fp} across the depletion region of an illuminated solar cell are both much smaller than kT for operation near the

maximum power point, then (2.2) should provide a very accurate description of the device characteristics. The numerical analysis described in the next subsection reveals that this condition on ΔE_{Fn} and ΔE_{Fp} at the maximum power point is easily satisfied for typical silicon or GaAs homojunction devices. More generally, (2.2) is most likely to be applicable to those devices fabricated on substrates with high carrier mobilities and long minority carrier lifetimes. From (2.21) and (2.22) it is apparent that the drops in E_{Fn} and E_{Fp} across the depletion region required to support a given photocurrent at some specified bias point will be small when μ_n and μ_p are large, if other device properties are constant. For a device with long carrier lifetimes, the carrier concentrations in the depletion region can be raised to relatively high levels before the total rate of recombination becomes comparable to the total rate of photogeneration. Thus the effect of high mobilities is to minimize the increase in carrier concentrations in the depletion region under illumination, while the effect of long lifetimes is to minimize the increase in total recombination brought about by this rise in carrier concentration.

2.2.4 Numerical Analysis of Silicon and GaAs Homojunction Cells

In subsection 2.2.2 it was shown that if the quasi-fermi energy levels were always constant across the depletion region of an illuminated solar cell, then (2.2) would accurately describe the cell characteristics in the low-level injection regime. This assumption of constant quasi-fermi levels in the depletion region had been used in all previous attempts to justify (2.2) [30,31]. In subsection 2.2.3, essentially qualitative arguments based on (2.21) and (2.22) were used to show that for operation at short-circuit or under low forward bias the quasi-fermi levels in

fact vary sharply over the depletion region of any illuminated cell. However, it was subsequently proposed that in cells with reasonable lifetimes and carrier mobilities the drops in E_{Fn} and E_{Fp} across the depletion region would be very small for operation near the maximum power point, and that consequently (2.2) would provide an excellent description of the cell characteristics at all operating points.

The purpose of this subsection is to use direct numerical solutions of the basic semiconductor equations to provide quantitative support for the conclusions drawn in subsections 2.2.2 and 2.2.3. The algorithm chosen for the numerical solution of (2.3)-(2.7) was that developed by Seidman and Choo [51]; a detailed description of the algorithm and a complete listing of the FORTRAN programs written to implement it are given in Appendix A. It should be stressed that this algorithm makes no arbitrary assumptions concerning the behaviour of the electrostatic potential and the quasi-fermi levels within a device. Two devices were modelled, one a silicon cell resembling those available commercially, and the other a GaAs cell. The doping profiles and material properties for these two cells are summarized in Table 2.1.

In commercial silicon cells, the emitter is usually formed by carrying out a phosphorus diffusion under constant surface concentration conditions at a temperature close to 900°C. As a result, the emitter doping profile is of the complementary error function form, with a phosphorus concentration of approximately 10^{20} atoms/cm^3 at the surface [52]. However, recent studies have shown that because of the bandgap narrowing associated with such high impurity concentrations, the effective doping near the surface of the emitter is considerably lower than the actual phosphorus concentration [53]. To compensate for this effect, in the

TABLE 2.1 Cell properties used in numerical analysis

a) N^+P Silicon Cell

doping profile	Gaussian
base doping	$5*10^{15}$ cm^{-3}
donor concentration at emitter surface	$1*10^{19}$ cm^{-3}
metallurgical junction depth	0.5 μm
device width	250 μm
carrier lifetimes	see Appendix A
carrier mobilities	see Appendix A
S_F	10^3 cm s^{-1}
S_B	infinite

b) P^+N GaAs Cell

doping profile	Gaussian
base doping	$1*10^{17}$ cm^{-3}
acceptor concentration at emitter surface	$1*10^{19}$ cm^{-3}
metallurgical junction depth	0.2 μm
device width	10.0 μm
carrier lifetimes	$\tau_n = 10^{-9}$ s; $\tau_p = 10^{-8}$ s
carrier mobilities	see Appendix A
S_F	0
S_B	infinite

numerical model a Gaussian doping profile with a surface concentration of only 10^{19} atoms/cm^3 was used in the emitter. The Gaussian profile is somewhat flatter near the surface than the complementary error function distribution.

Since GaAs cells are still in a developmental stage, it is difficult to select a representative design for such a device. In recent years, both P^+N [43,54] and N^+P [55] GaAs cells prepared by several different techniques have shown promisingly high efficiencies. The structure and material properties of the P^+N GaAs cell considered here were chosen more to ensure that the bulk of both photogeneration and recombination would occur in the depletion region than to accurately model a particular experimental device. To this end the photogeneration distribution G(x) was set to correspond to the uniform absorption in the depletion region of all photons in the solar spectrum with energies greater than the GaAs bandgap; G(x) was made equal to zero in the other regions of the cell.

Some preliminary tests on the accuracy of the solutions to the basic equations obtained using Seidman and Choo's algorithm are described in Appendix A. These initial tests were concerned primarily with establishing an appropriate grid geometry for the applications considered here. To provide a further test of the capabilities of the numerical model, the dark current-voltage characteristics for both the silicon and the GaAs cell were computed. The results are plotted in Fig. 2.4.

The characteristic for the silicon cell strongly resembles those recorded for experimental silicon diodes, in that two regimes over which the current depends exponentially on bias can be discerned. When the forward bias is less than approximately 250 mV, the current obeys the relation

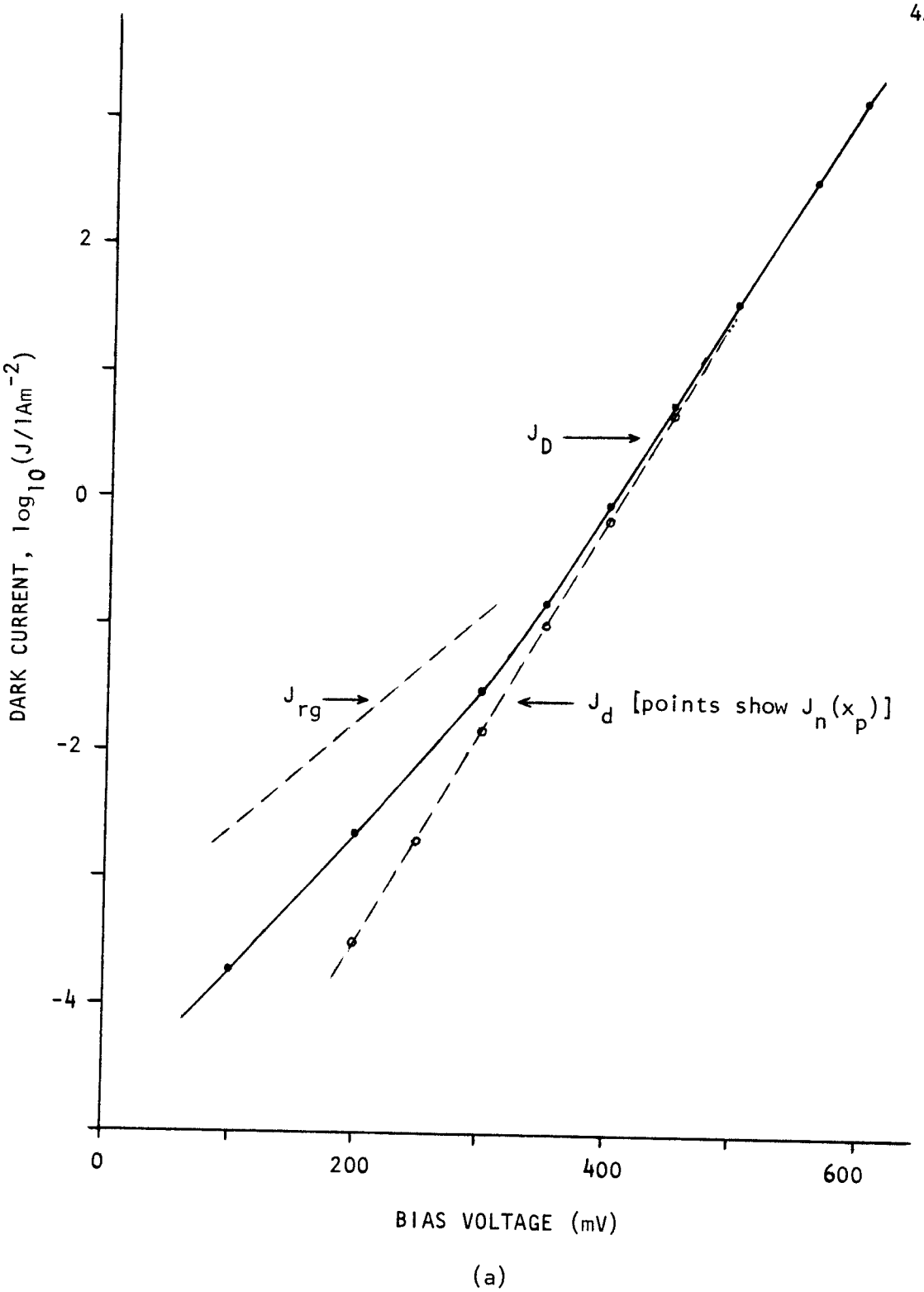

(a)

Figure 2.4 Dark current-voltage characteristics. True $J_D(V)$ curve is drawn solid; J_{rg} and J_d curves computed from (2.26) and (2.27) or (2.28) are drawn dashed.
(a) Silicon cell. (b) GaAs cell.

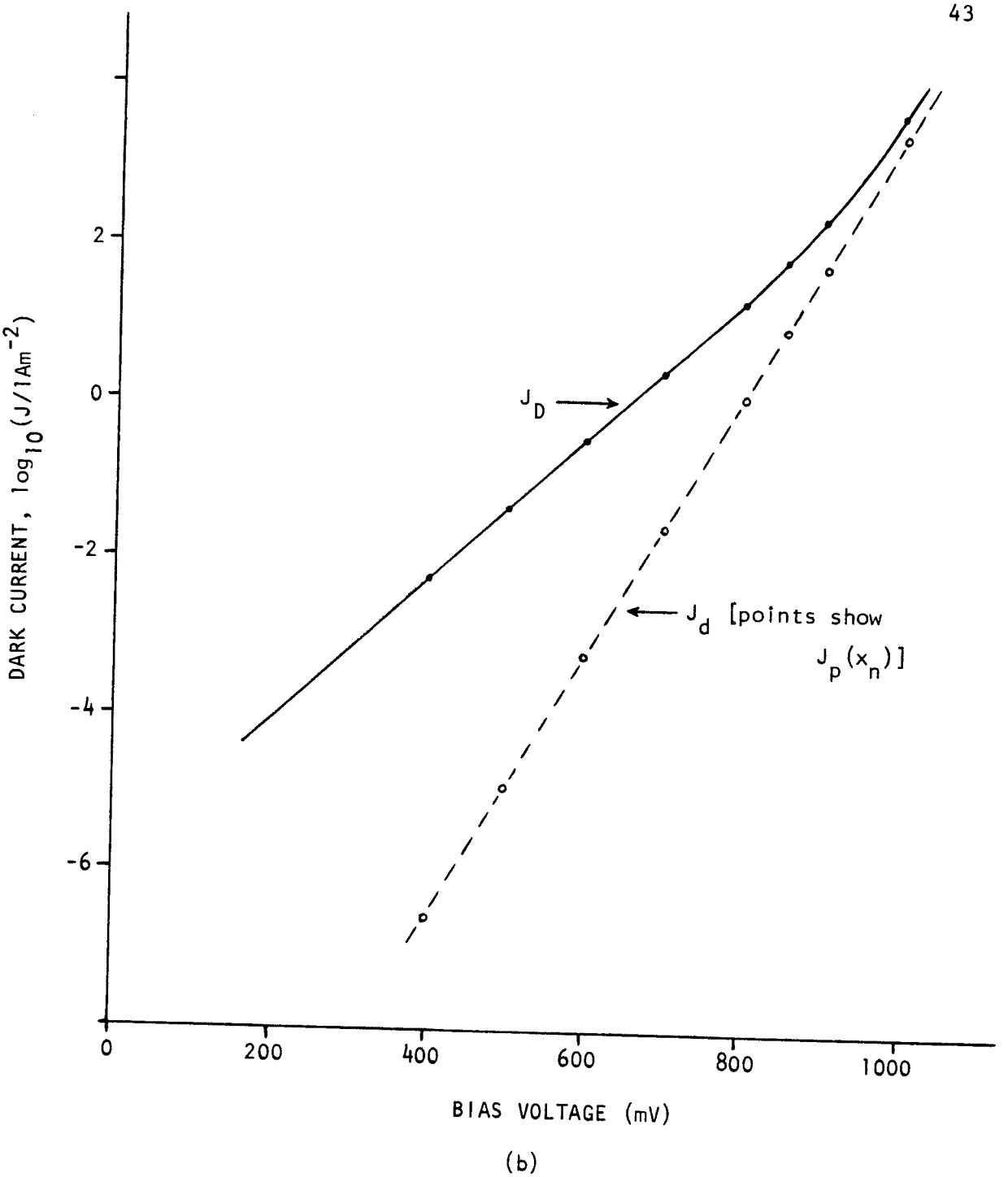
DARK CURRENT, $\log_{10}(J/1Am^{-2})$
2
0
-2
-4
-6
0
200
400
600
800
1000
BIAS VOLTAGE (mV)
J_D
J_d [points show $J_p(x_n)$]

(b)

Figure 2.4(b)

$$J_D(V) = J_0 \exp(qV/AkT) \tag{2.25}$$

where A≃1.6. In this regime the diode current is dominated by recombination in the depletion region. For forward biases greater than approximately 400 mV, recombination in the quasi-neutral base becomes dominant and the current again depends exponentially on V, but with an A-factor very close to unity. Over the bias range from 250 to 400 mV, a transition between the two regimes takes place, and J_D does not have a simple single-exponential dependence on V. A crude analytic approximation to the depletion region recombination current J_{rg} is given by (2.24), which can be written in the form [50]

$$J_{rg}(V) \simeq [qn_i W/(2\sqrt{\tau_n \tau_p})] \exp(qV/2kT) \ . \tag{2.26}$$

Under low-level injection conditions an analytic expression for the electron injection-diffusion current flowing into the base is [61]

$$J_d(V) = J_{0d} [\exp(qV/kT) - 1] \tag{2.27a}$$

where

$$J_{0d} = \frac{qD_n n_i^2}{L_n N_A} \left[\frac{\mathrm{Sinh}(L_B/L_n) + (S_B L_n/D_n)\ \mathrm{Cosh}(L_B/L_n)}{\mathrm{Cosh}(L_B/L_n) + (S_B L_n/D_n)\ \mathrm{Sinh}(L_B/L_n)} \right] \tag{2.27b}$$

$$\xrightarrow{S_B \to \infty} \frac{qD_n n_i^2}{L_n N_A} \ \mathrm{Coth}(L_B/L_n). \tag{2.27c}$$

Here L_B is the base width. Plots of $J_{rg}(V)$ and $J_d(V)$ obtained by substituting the parameters listed in Table 2.1(a) into (2.26) and (2.27) have been superposed on Fig. 2.4(a). It can be seen that there is excellent agreement between the upper branch of the $J_D(V)$ characteristic computed using Seidman and Choo's algorithm and the analytic expression for $J_d(V)$. However, the expression for J_{rg} specified in (2.26) clearly overestimates the dark current flowing at small forward bias. This is not unexpected, for in the derivation of (2.26) the maximum rate of recombination in the depletion region is first determined, and it is then assumed that this recombination rate applies throughout the region [50].

The $J_D(V)$ characteristic for the GaAs cell reveals the importance of depletion region recombination currents in this material. For forward biases less than approximately 800 mV, (2.25) is obeyed with A≈1.8. By analogy with (2.27), the analytic expression for the hole injection-diffusion current flowing into the uniformly doped n-type base of the GaAs cell is

$$J_d(V) = J_{0d}\,[\exp(qV/kT) - 1] \tag{2.28a}$$

where

$$J_{0d} = \frac{qD_p n_i^2}{L_p N_D}\left[\frac{\mathrm{Sinh}(L_B/L_p) + (S_B L_p/D_p)\,\mathrm{Cosh}(L_B/L_p)}{\mathrm{Cosh}(L_B/L_p) + (S_B L_p/D_p)\,\mathrm{Sinh}(L_B/L_p)}\right] \tag{2.28b}$$

$$\xrightarrow{S_B \to \infty} \frac{qD_p n_i^2}{L_p N_D}\,\mathrm{Coth}(L_B/L_p). \tag{2.28c}$$

This analytic form for $J_d(V)$ has been overplotted on Fig. 2.4(b). It can be seen that even at a forward bias of 900 mV, which gives a dark current density comparable in magnitude to the one-sun photocurrent, less than 25% of the total current flowing results from recombination in the quasi-neutral base.

More precise checks on the accuracy of the numerical analysis can be made by examining the individual electron and hole current components within a device. For example, the electron current flowing across the plane x_p into the quasi-neutral base of an N^+P cell should conform closely to (2.27), while the hole current crossing the plane x_n in a P^+N cell should agree with (2.28). In a real device there is some ambiguity in locating the planes x_n and x_p, since the boundaries between the depletion region and the quasi-neutral regions are not abrupt. Here x_n and x_p were defined arbitrarily to be the planes at which the free-carrier concentration equals 90% of the donor or acceptor concentration. Using this definition, $J_n(x_p)$ for the silicon cell and $J_p(x_n)$ for the GaAs cell were determined and plotted in Fig. 2.4. For both devices there is excellent agreement between the analytic expression for the minority carrier injection-diffusion current flowing into the base and the value computed for this current component using the numerical model.

The band diagrams generated by the numerical model for the silicon cell under a variety of bias and illumination conditions are presented in Fig. 2.5. The corresponding band diagrams for the GaAs cell have the same qualitative form, and so are not shown. Under moderate forward bias in the dark, the electron and hole quasi-fermi levels are both found to be very nearly constant across the depletion region. However, under one-sun illumination at short-circuit or small forward bias, E_{Fn} and E_{Fp}

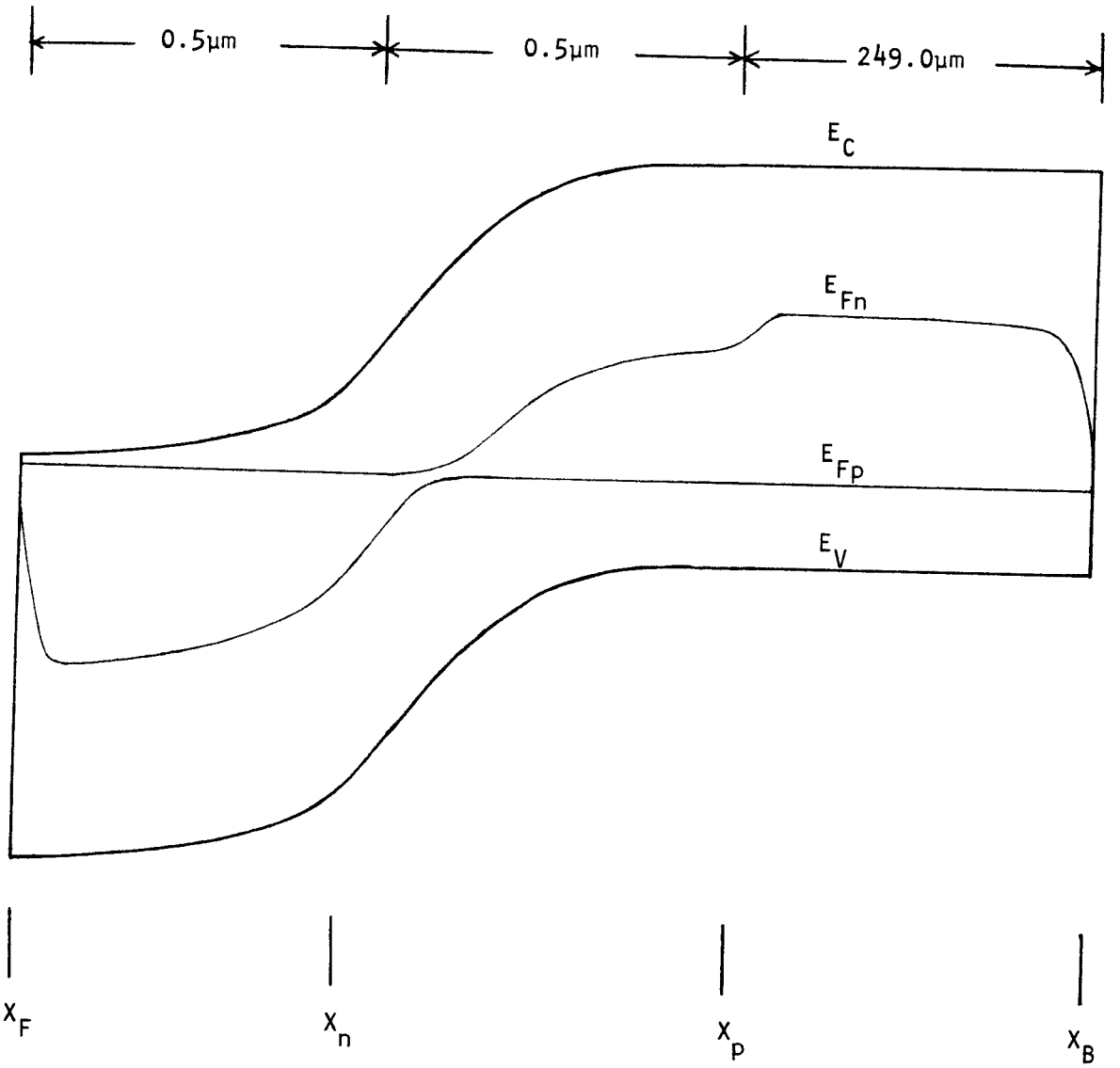

Figure 2.5 Band diagrams for silicon cell.

(a) Short-circuit, one-sun illumination.

(b) Maximum power point, one-sun illumination.

(c) $V=V_{mp}$ in dark.

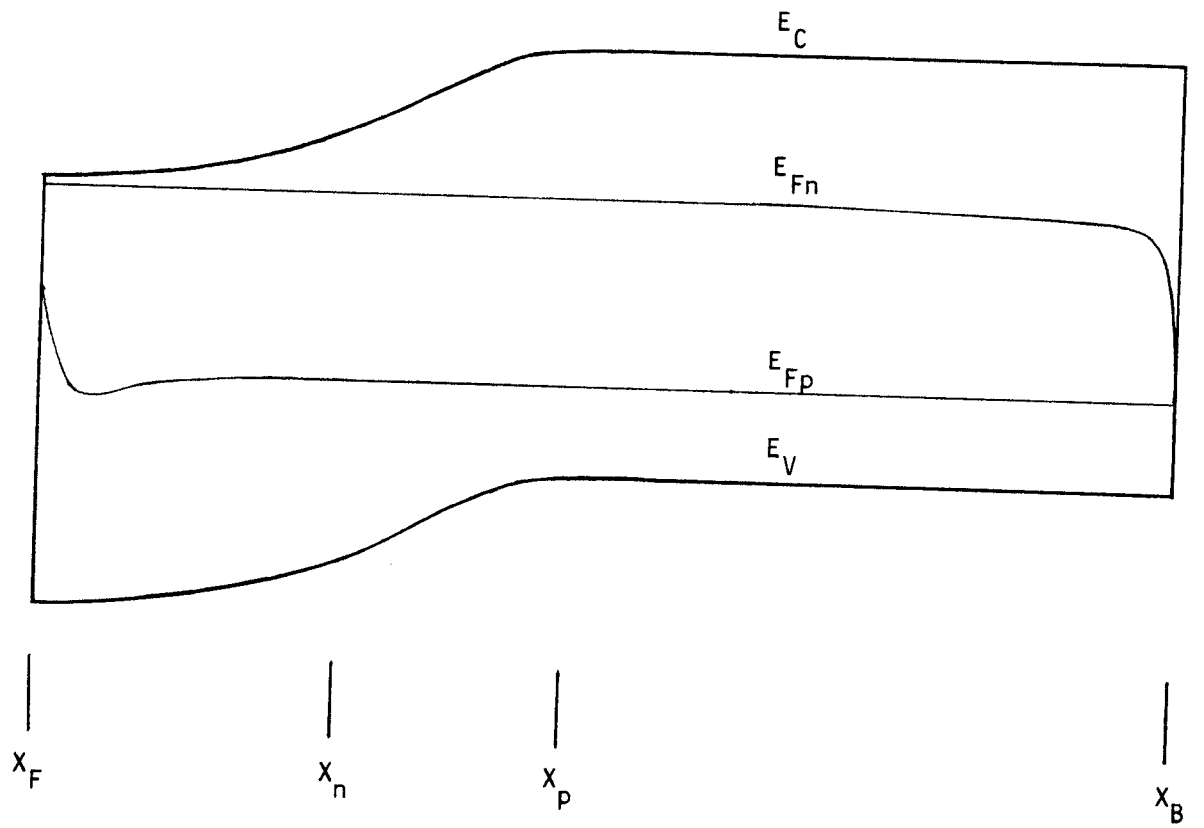

(b)

Figure 2.5(b)

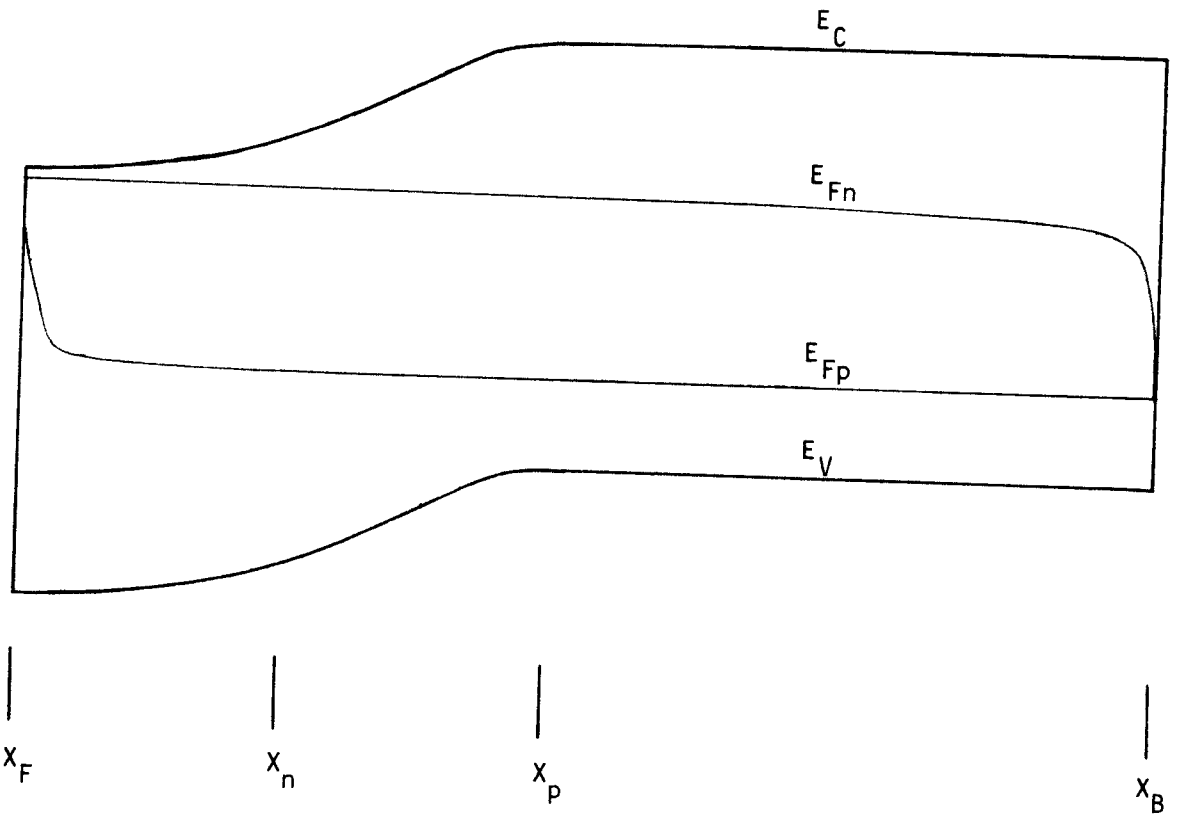

(c)

Figure 2.5(c)

shift so as to greatly increase the carrier concentrations in this region. As the forward bias is increased under illumination, the drops in E_{Fn} and E_{Fp} across the depletion region become smaller; by the time the maximum power point is reached both quasi-fermi levels are effectively constant across the depletion region. All these results are in agreement with the conclusions drawn from the qualitative arguments of subsection 2.2.3. Actual values for ΔE_{Fn} and ΔE_{Fp} are tabulated in Table 2.2.

Fig. 2.6 presents the "true" $J_L(V)$ characteristic (that is, the $J_L(V)$ curve obtained using the numerical model) and a plot of the curve $J_{sc} - J_D(V)$ under one-sun illumination for both the silicon and the GaAs cell. To the scale of the figure, the difference between the two curves is not visible for either device. A more precise measure of the accuracy of the superposition principle in describing the illuminated current-voltage characteristics for these two cells is provided by Table 2.3, which lists the true values of open-circuit voltage, fill factor, maximum output power and maximum power point voltage together with the values for these quantities predicted by (2.2). As expected, the true maximum output power is slightly less than that predicted by the superposition principle, although the difference is only 0.4% for the silicon cell and less than 0.1% for the GaAs cell. For the silicon cell, the true open-circuit voltage is found to be 1.5 mV less than that calculated using (2.2), while for the GaAs cell the difference is less than 0.1 mV. In short, Fig. 2.6 and Table 2.3 indicate that the superposition principle provides just as accurate a description of the characteristics of a GaAs cell in which the bulk of both recombination and photogeneration occur in the depletion region as it does for a typical commercial silicon cell.

TABLE 2.2 Changes in quasi-fermi levels across depletion region under various operating conditions

a) Silicon Cell

Condition:	ΔE_{Fn}(eV):	ΔE_{Fp}(eV):
short-circuit, one-sun	0.36	0.28
max. power point, one-sun	$3*10^{-4}$	$9*10^{-5}$
open-circuit, one-sun	$4*10^{-6}$	$5*10^{-6}$
$V = V_{mp}$, dark	$2*10^{-5}$	$2*10^{-6}$

b) GaAs Cell

Condition:	ΔE_{Fn}(eV):	ΔE_{Fp}(eV):
short-circuit, one-sun	0.19	0.47
max. power point, one-sun	$1*10^{-6}$	$2*10^{-3}$
open-circuit, one-sun	$2*10^{-6}$	$3*10^{-4}$
$V = V_{mp}$, dark	$1*10^{-6}$	$2*10^{-4}$

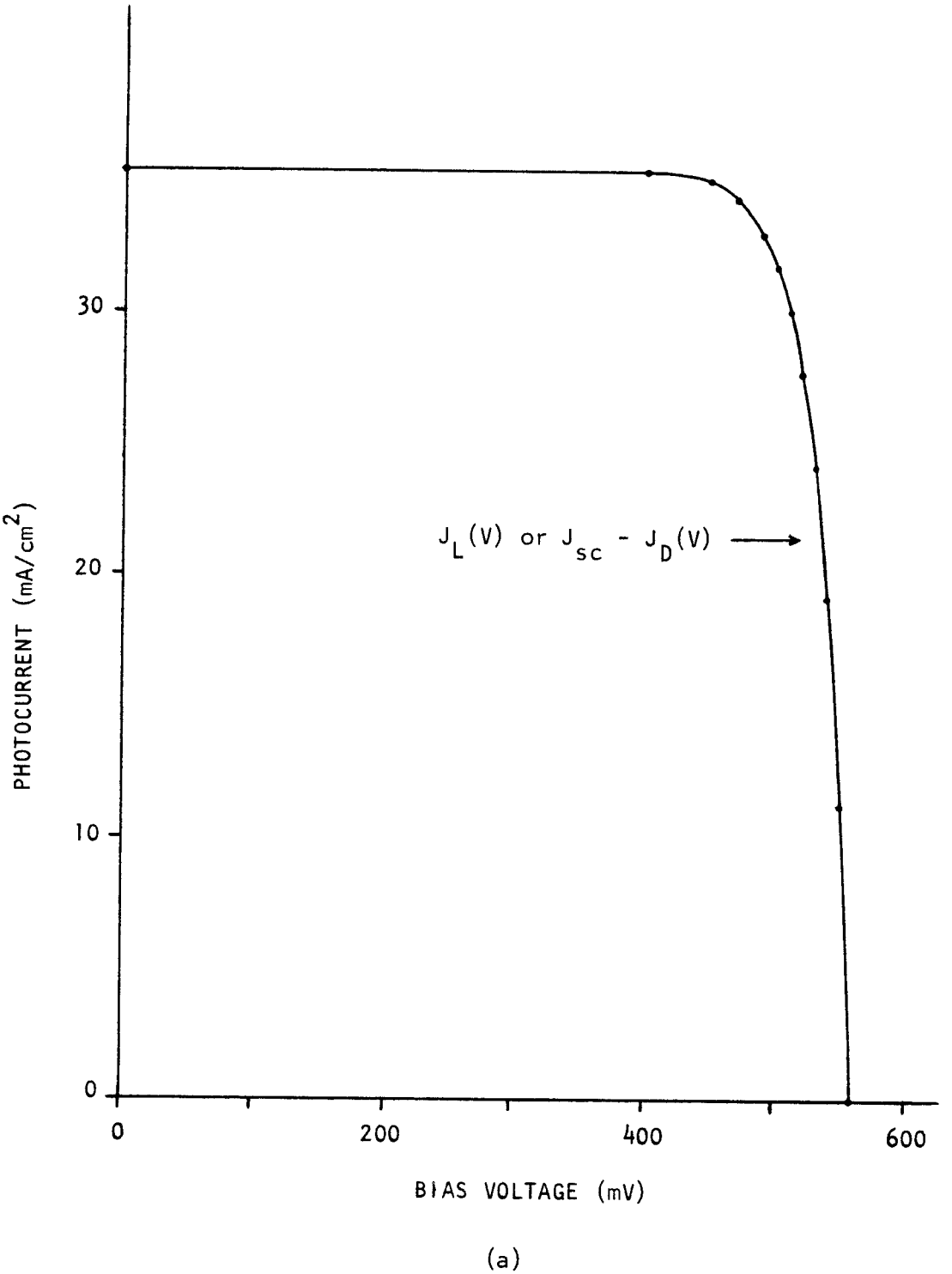

(a)

Figure 2.6 Plot of the true current-voltage characteristic $J_L(V)$, and of the curve $J_{sc} - J_D(V)$, under one-sun illumination. To the scale of the figure, the two curves coincide. (a) Silicon cell. (b) GaAs cell.

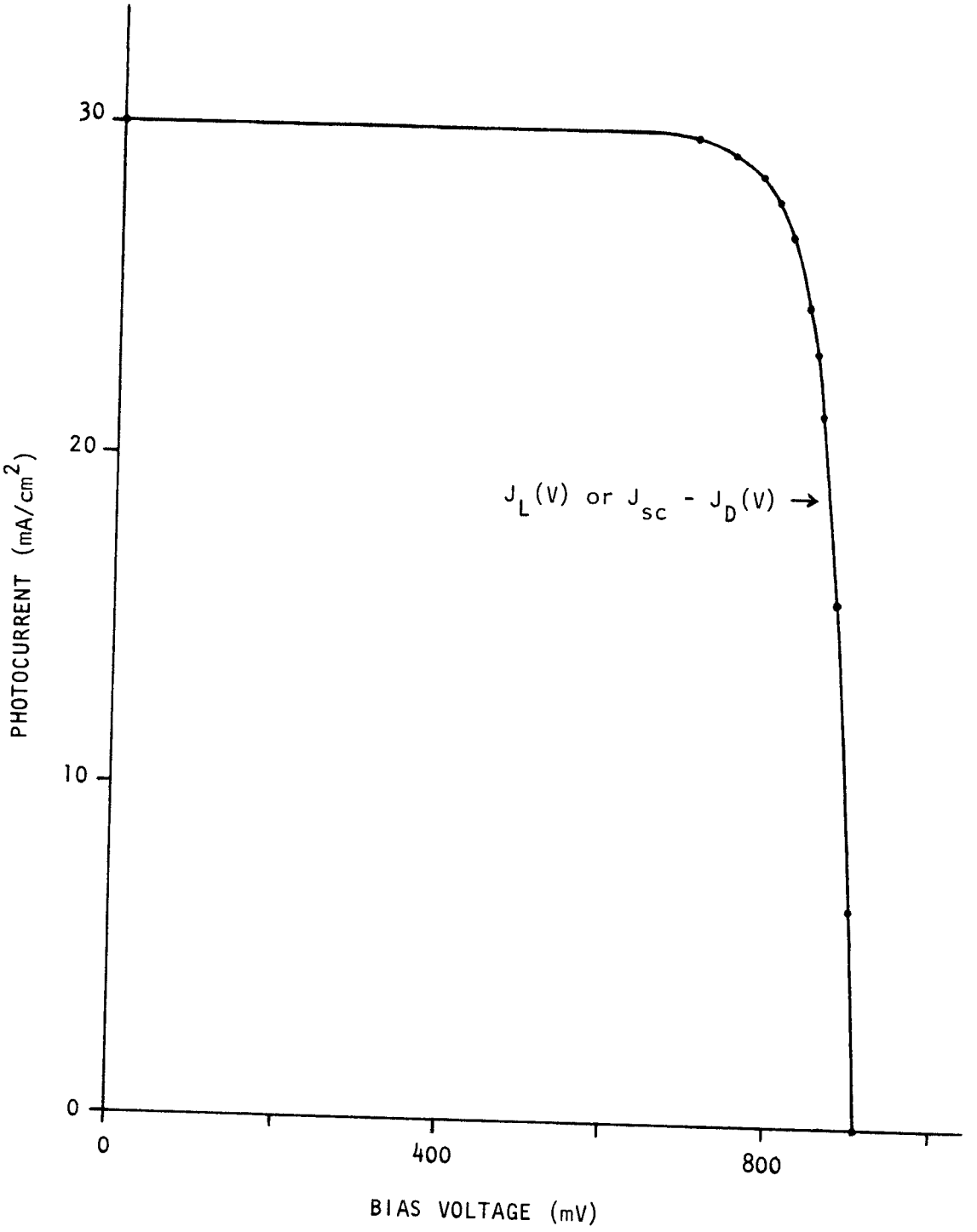
30
20
10
0
PHOTOCURRENT (mA/cm^2)
$J_L(V)$ or $J_{sc} - J_D(V)$ →
0
400
800
BIAS VOLTAGE (mV)
(b)

Figure 2.6(b)

TABLE 2.3 True performance parameters, and those predicted by the superposition principle

a) Silicon Cell

Quantity:	True value:	Predicted by superposition:
J_{sc} [A m^{-2}]	355.0	-
V_{oc} [mV]	558.5	560.0
V_{mp} [mV]	481±2	482±2
P_{max} [mW]	161.4	162.1
FF	0.814	0.815

b) GaAs Cell

Quantity:	True value:	Predicted by superposition:
J_{sc} [A m^{-2}]	301.2	-
V_{oc} [mV]	909.1	909.1
V_{mp} [mV]	789±2	790±2
P_{max} [mW]	224.7	224.8
FF	0.821	0.821

2.2.5 A Case of Superposition Breakdown

For certain device configurations the drop in one or both quasi-fermi levels across the depletion region at the maximum power point may be large even if E_{Fn} and E_{Fp} are essentially constant across this region at forward bias in the dark. This condition can arise if, for example, a large photogenerated hole current flows through a part of the depletion region in which the hole concentration is small and through which relatively little hole current would flow for operation in the dark. Such a situation might be encountered in a device in which the dark current is dominated by recombination in the depletion region while most photogeneration occurs in the emitter. It was noted in subsection 2.2.3 that to support a depletion region recombination current in an N^+P device, the electron flow need only be large in that part of the depletion region nearest the emitter, while the hole flow need be large only near the base (Fig. 2.7(a)). However, if most photogeneration takes place in the emitter then when the device is illuminated a large hole photocurrent must flow all the way across the depletion region from the emitter to the base. In order to support this photocurrent, the hole quasi-fermi level in the depletion region must be displaced from its dark position so as to greatly increase the hole concentration near the emitter (Fig. 2.7(b)). This has the result of extending the zone of maximum recombination from the center of the depletion region towards the emitter. If the carrier lifetimes and mobilities are sufficiently small, the rate of total recombination may be raised to such an extent that the true illuminated current-voltage characteristics differ measurably from those predicted by (2.19) or (2.2). This effect is illustrated in Fig. 2.8, which displays the true $J_L(V)$ curve and the curve $J_{sc} - J_D(V)$ for an N^+P GaAs cell with the properties

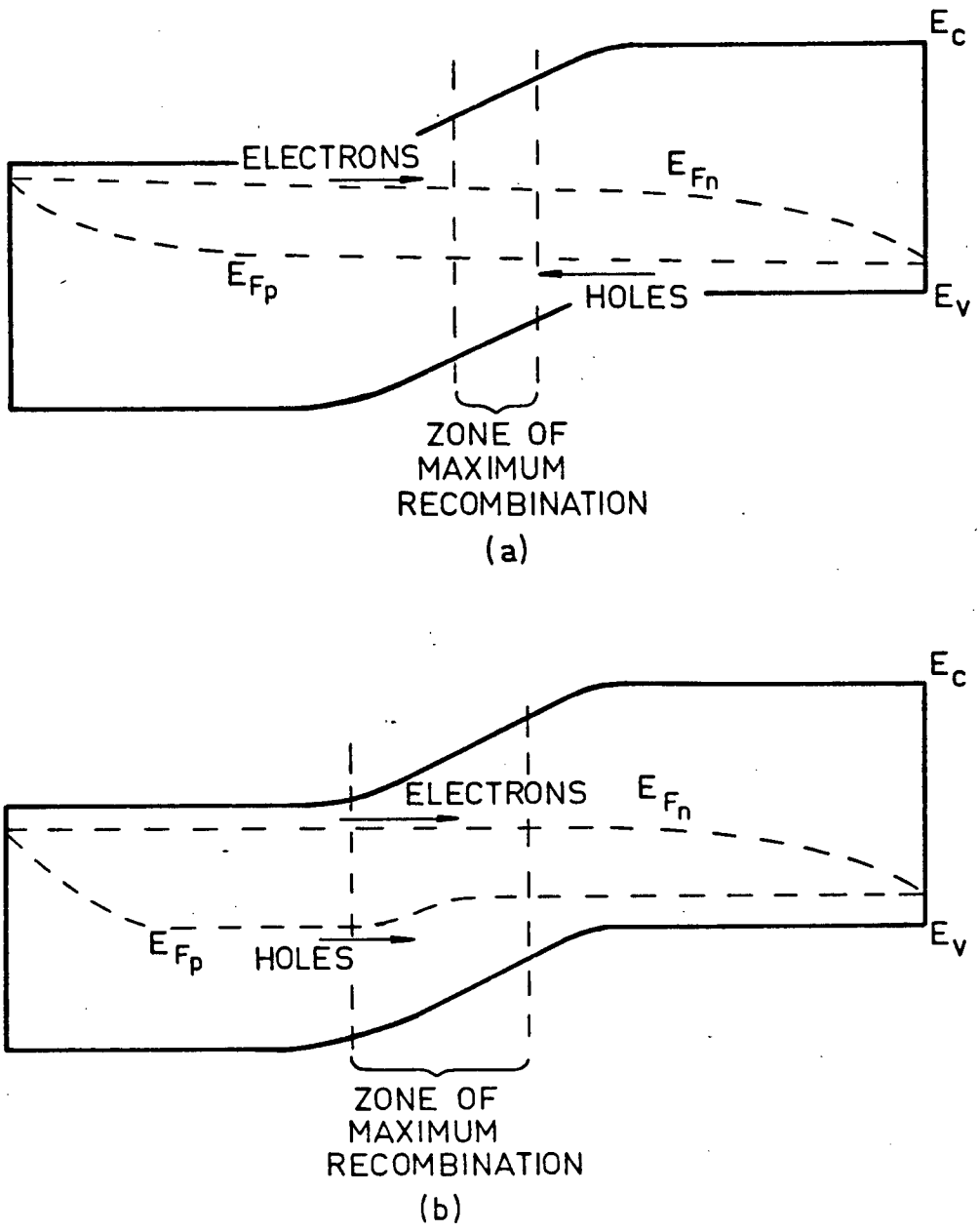

Figure 2.7 Band diagram for cell in which most photogeneration occurs in emitter while most recombination occurs in depletion region. (a) At forward bias in the dark. (b) Under illumination at same forward bias.

TABLE 2.4 Properties of N^+P GaAs cell whose characteristics are shown in Fig. 2.8

doping profile	abrupt
base doping	$1*10^{16}$ cm^{-3}
emitter doping	$1*10^{19}$ cm^{-3}
metallurgical junction depth	0.4 μm
device width	20.0 μm
carrier lifetimes	$\tau_n = \tau_p = 2*10^{-11}$ s
carrier mobilities	$\mu_n = 0.1$ m^2 V^{-1} s^{-1}; $\mu_p = 0.005$ m^2 V^{-1} s^{-1}
S_F, S_B	infinite

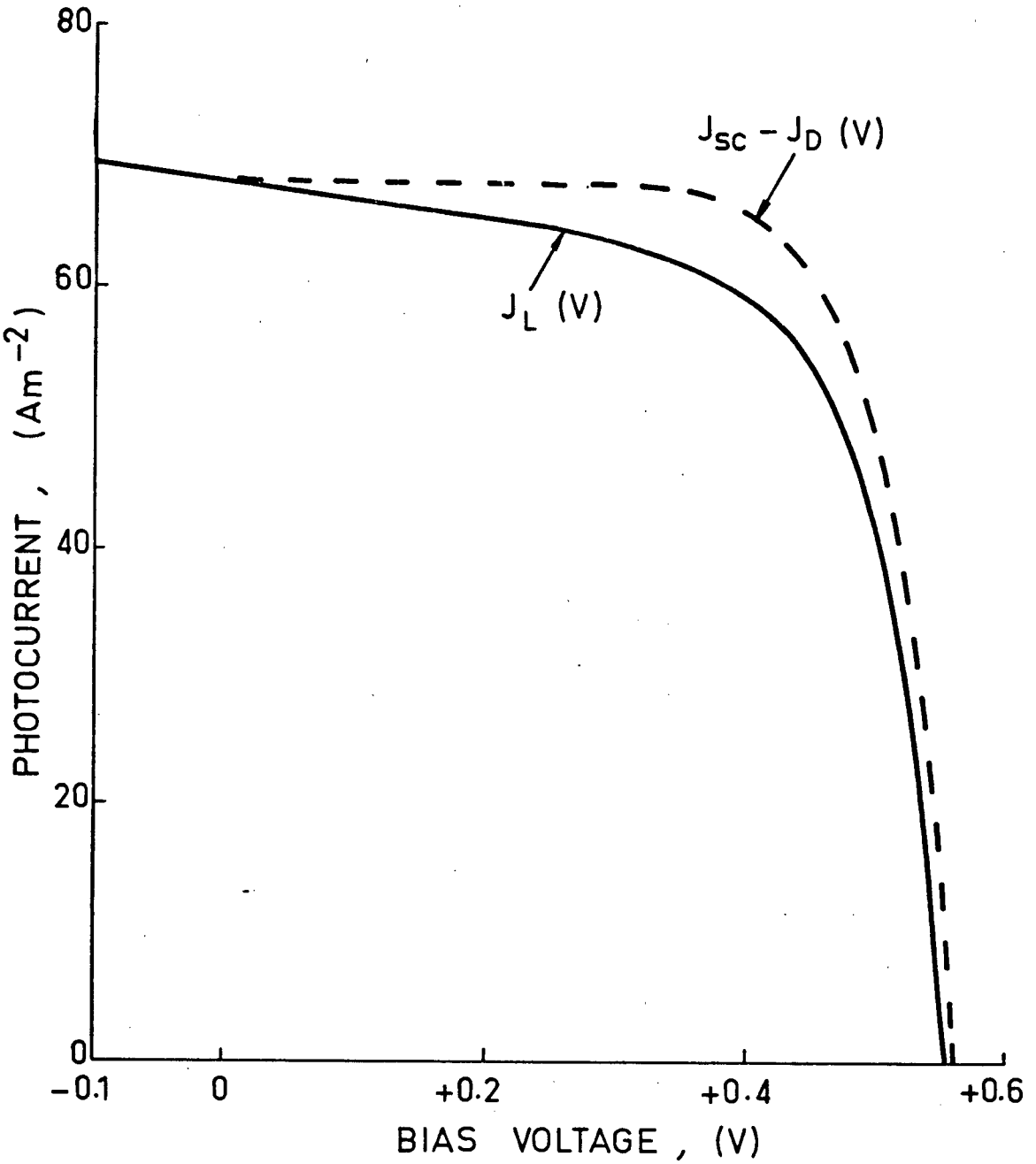

Figure 2.8 $J_{sc} - J_D(V)$ and true $J_L(V)$ characteristics for an N^+P GaAs cell with low mobilities and very short lifetimes. (One-sun illumination).

listed in Table 2.4. (Fig. 2.8 was generated using the numerical analysis described in the previous subsection and in Appendix A). The cell has very short lifetimes and low mobilities, properties which might be found in poor-quality polycrystalline substrates. For this device, essentially all recombination occurs in the depletion region, while G(x) was set to correspond to the uniform absorption in the emitter of all photons in the AM1 spectrum with energies greater than the GaAs bandgap. Fig. 2.8 reveals that for this cell the true fill factor and open-circuit voltage are both significantly less than those predicted by (2.2). Also, the application of a small reverse bias increases the photocurrent which can be drawn from the cell, so J_{upc} and J_{sc} are not equal. It must be emphasized that the breakdown of the superposition principle evident in Fig. 2.8 is not due to the variation in the width of the depletion region with bias. Since this is an N^+P device, the boundary between the quasi-neutral emitter and the depletion region does not move appreciably as the bias changes.

2.3 Back Surface Field Regions

In a typical N^+P silicon cell the open-circuit voltage under one-sun illumination is limited by recombination in the quasi-neutral base. In order to attain higher open-circuit voltages in cells of this kind, it is therefore necessary to reduce the magnitude of the electron injection-diffusion dark current flowing into the base. From (2.27) it is apparent that J_d can be reduced by increasing the base doping N_A, if the other material properties remain constant. Experimentally, it is found that V_{oc} increases as the substrate resistivity decreases from 10 Ωcm to 0.1 Ωcm. However, for material prepared by the Czochralski technique the electron

lifetime and diffusion length begin to drop sharply for resistivities lower than about 0.1 Ωcm [57]. As a result, increases in substrate doping beyond this point lead to a slow fall-off in both short-circuit current and V_{oc} [56,57].

An alternative method for suppressing electron recombination in the base is to use a lightly doped substrate, but form a high-low junction at the rear of the cell [58,59]. The band diagram for such a structure under moderate forward bias is shown in Fig. 2.9. High-low junctions of this kind are known as "back surface fields", since the built-in electric field at the junction repels minority carriers from the region of very high surface recombination velocity at the ohmic back contact. In order for a back surface field structure to be of use in reducing the electron injection-diffusion dark current, the electron diffusion length in the base must be substantially greater than the base width. This condition is satisfied in most present-day commercial cells fabricated on lightly doped substrates of high quality [57].

From the band diagram of Fig. 2.9, it can be seen that at a given forward bias the electron concentration is far lower in the heavily doped region of the high-low junction than at the rear edge of the lightly doped region. The high-low junction thus greatly reduces the electron concentration in the vicinity of the back surface, thereby screening the minority carrier electrons from this region of high recombination velocity. Provided the electron concentration remains at low injection levels throughout the base, the high-low junction can be described by an effective recombination velocity S_{eff} which is far lower than S_B. More precisely, the magnitude of the electron injection-diffusion current entering the base of the back surface field cell would not be altered if the

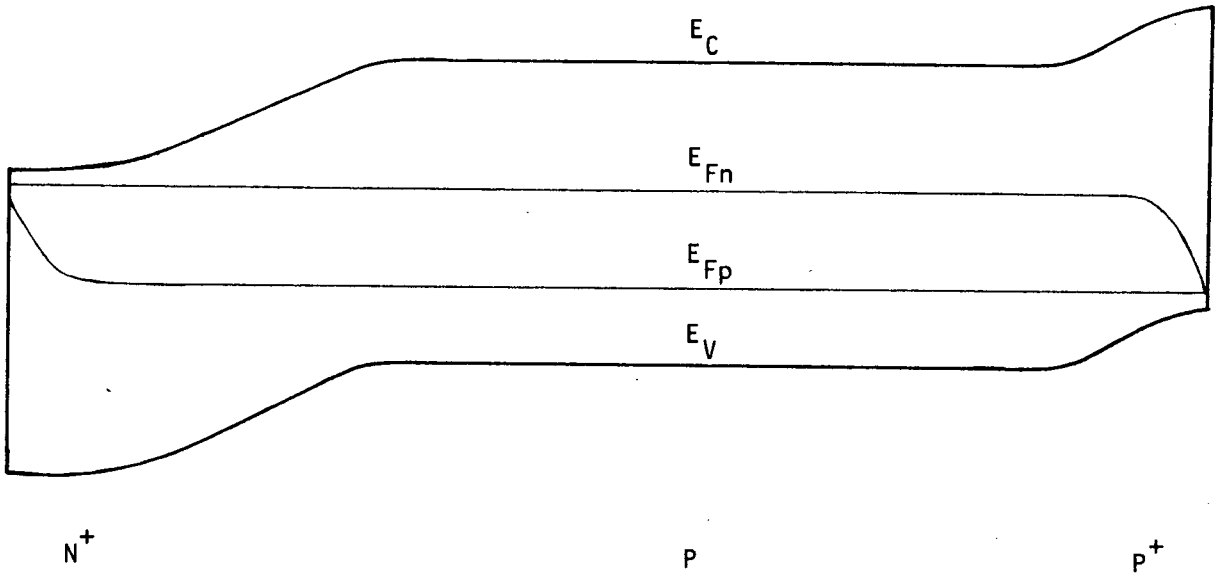

Figure 2.9 Band diagram for N^+PP^+ back surface field cell under moderate forward bias.

high-low junction were replaced by a surface with recombination velocity S_{eff} for electrons. Hauser and Dunbar [60] and Godlewski et al. [61] have derived expressions for S_{eff} for the case in which the back surface field region is uniformly doped, while Fossum [62] has presented an approximate analysis of the more realistic case in which the back surface field doping profile is non-uniform.

Aside from an enhancement in open-circuit voltage, the back surface field structure provides a modest increase in short-circuit current and fill factor [62]. The increase in short-circuit current results from an improved collection efficiency for minority carriers generated deep in the base by long-wavelength photons. An electron photogenerated near the middle of the base has a roughly equal probability of diffusing to the front junction or to the back contact region. In a cell with an ohmic back contact, an electron reaching the back surface will recombine and thus make no contribution to the photocurrent. However, in a cell with a properly designed back surface field an electron approaching the back surface will be reflected, and may eventually reach the junction and contribute to the photocurrent. The increase in fill factor results from conductivity modulation due to the increased minority carrier concentration in the base of the back surface field cell; this effect is important only in or near the high-level injection regime.

In industry, a rather unusual technique is currently used to fabricate N^+PP^+ back surface field cells. Following formation of the front junction, an organic paste containing metallic aluminum is applied to the back of the cell and then fired at a temperature of approximately 850°C for roughly one minute [134]. This procedure forms a layer of aluminum-silicon alloy a few microns deep which behaves in some ways like

a heavily doped p-type region. Crude as this process may appear, the open-circuit voltages of N^+PP^+ cells formed in this way on 10 Ωcm substrates are typically 30-50 mV higher than those of otherwise identical N^+P devices lacking a back surface field region [134]. Although N^+P cells formed on high quality substrates of 1 to 0.1 Ωcm resistivity may give slightly higher open-circuit voltages, N^+PP^+ devices incorporating 10 Ωcm substrates have among the highest energy conversion efficiencies of all silicon cells. Recently Fossum and Burgess have reported the fabrication of P^+NN^+ back surface field cells giving the highest energy conversion efficiencies and among the highest open-circuit voltages ever reported for silicon homojunction devices [135]. In these high efficiency P^+NN^+ cells the back surface field region is formed by a conventional phosphorus diffusion using a phosphine source. The gettering action of this phosphorus diffusion is believed to play a major part in establishing long minority carrier lifetimes and diffusion lengths in the base region.

CHAPTER 3

POSITIVE BARRIER SCHOTTKY AND MIS JUNCTIONS: THEORY

In this chapter a unified analytic model of conduction in Schottky barrier and MIS junctions is developed. The foundation for this model is established in Sections 3.1 and 3.2. In Section 3.3 the model is applied to compute the current flow in a non-ideal Schottky diode. Section 3.4 then examines the effect of increasing the thickness of the interfacial layer in the non-ideal Schottky diode to form an MIS junction. Assuming only that the interfacial insulating layer in the MIS junction presents roughly the same barrier to electrons attempting to tunnel into the metal from either the valence or conduction band of the semiconductor, it is shown that the presence of this layer can virtually eliminate the flow of electrons between the majority carrier band and the metal while leaving the net electron flow between the minority carrier band and the metal essentially unaltered. Section 3.4 thus reconciles the prediction made by Green et al. that minority carrier flows can dominate the dark current in suitably prepared MIS diodes with the thermionic emission theory of conduction in Schottky diodes. This is a rather important point in view of suggestions made recently that current transport proceeds by fundamentally different mechanisms in Schottky and MIS diodes [63]. Section 3.5 extends the model of MIS diode operation developed in Section 3.4 to the case of the MIS solar cell. It should be acknowledged that much of the material presented in this chapter has been introduced previously, albeit in somewhat different form, in publications by Green et al. [16,17, 22-25] and by Card and Rhoderick [26-28].

This chapter considers only positive barrier Schottky and MIS junctions -- that is, junctions in which the semiconductor surface is depleted

or inverted at equilibrium. Junctions of this class are formed by depositing low work function metals on p-type silicon substrates, or high work function metals on n-type substrates. The properties of negative barrier MIS contacts are examined in Chapter 5.

3.1 Junction Barrier Heights

The band diagrams conventionally drawn to represent the available electron energy states in a typical MIS or non-ideal Schottky diode are shown in Fig. 3.1 [64]. In constructing Fig. 3.1(a), it has been assumed that the junction was formed by depositing a high work function metal on an n-type silicon substrate. Conversely, if the junction had been formed by depositing a low work function metal on a p-type substrate, the band diagram of Fig. 3.1(b) would be appropriate. For an n-type substrate, the junction barrier height $q\phi_{Bn}$ is defined to be the difference in energy between the conduction band edge at the semicondcutor surface and the fermi level in the metal, as shown in Fig. 3.1(a). For a p-type substrate, the barrier height $q\phi_{Bp}$ is the energy difference between the valence band edge at the surface and the metal fermi level, as shown in Fig. 3.1(b). Both these energy differences are to be measured at equilibrium.

Schottky originally proposed that the electrostatic potential barrier induced in the semiconductor at a Schottky or MIS junction results from the difference between the work function ϕ_M of the metal and the electron affinity χ_S of the semiconductor [65]. This model undoubtably has some relevance for junctions in which an interfacial layer is present, although the use of concepts such as work function and electron affinity seems fundamentally suspect when the metal and semiconductor are separated by an oxide film only a few atomic diameters thick. Bardeen later postulated

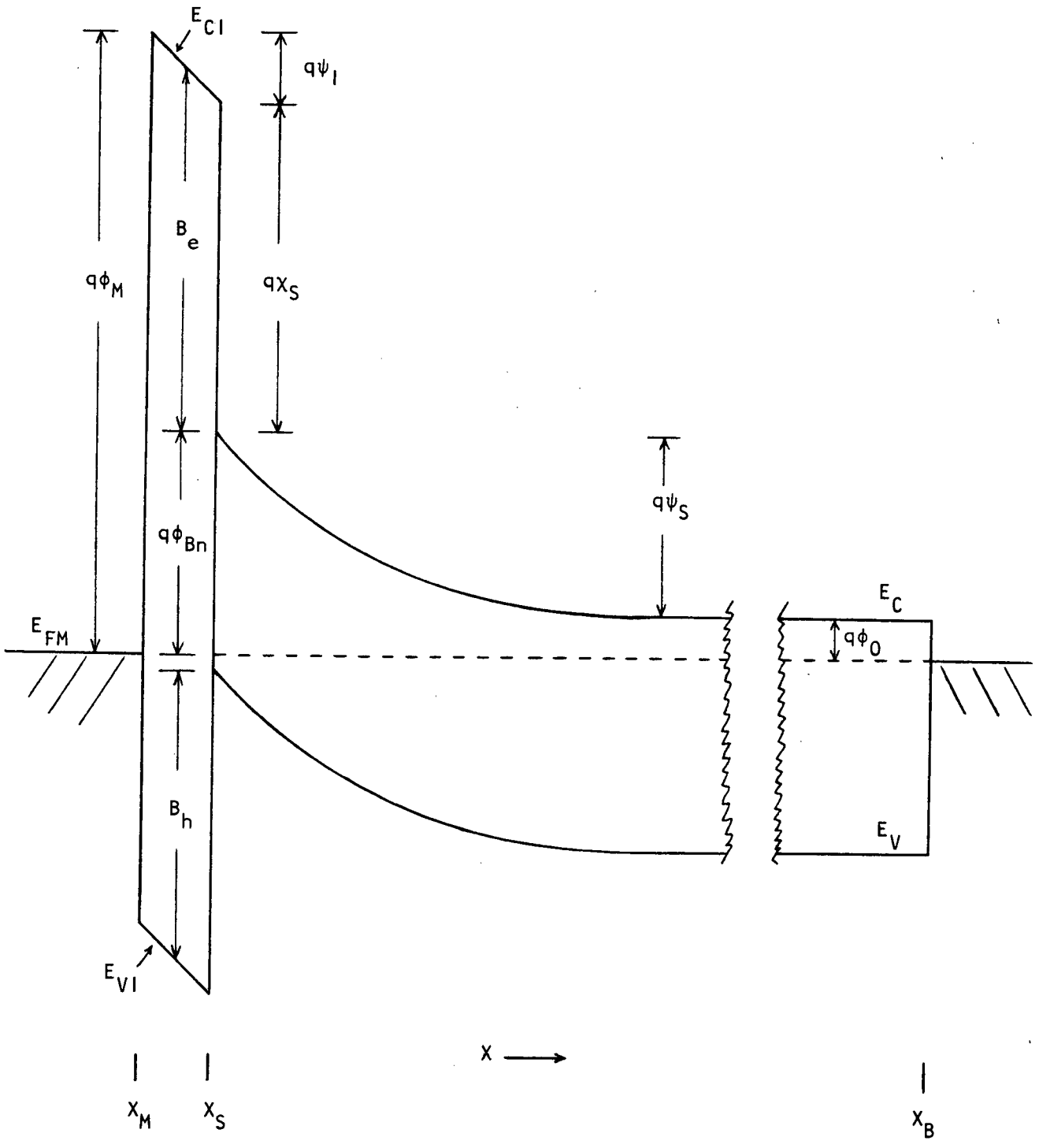

(a)

Figure 3.1 Equilibrium band diagram for MIS or non-ideal Schottky diodes. (a) n-type substrate. (b) p-type substrate.

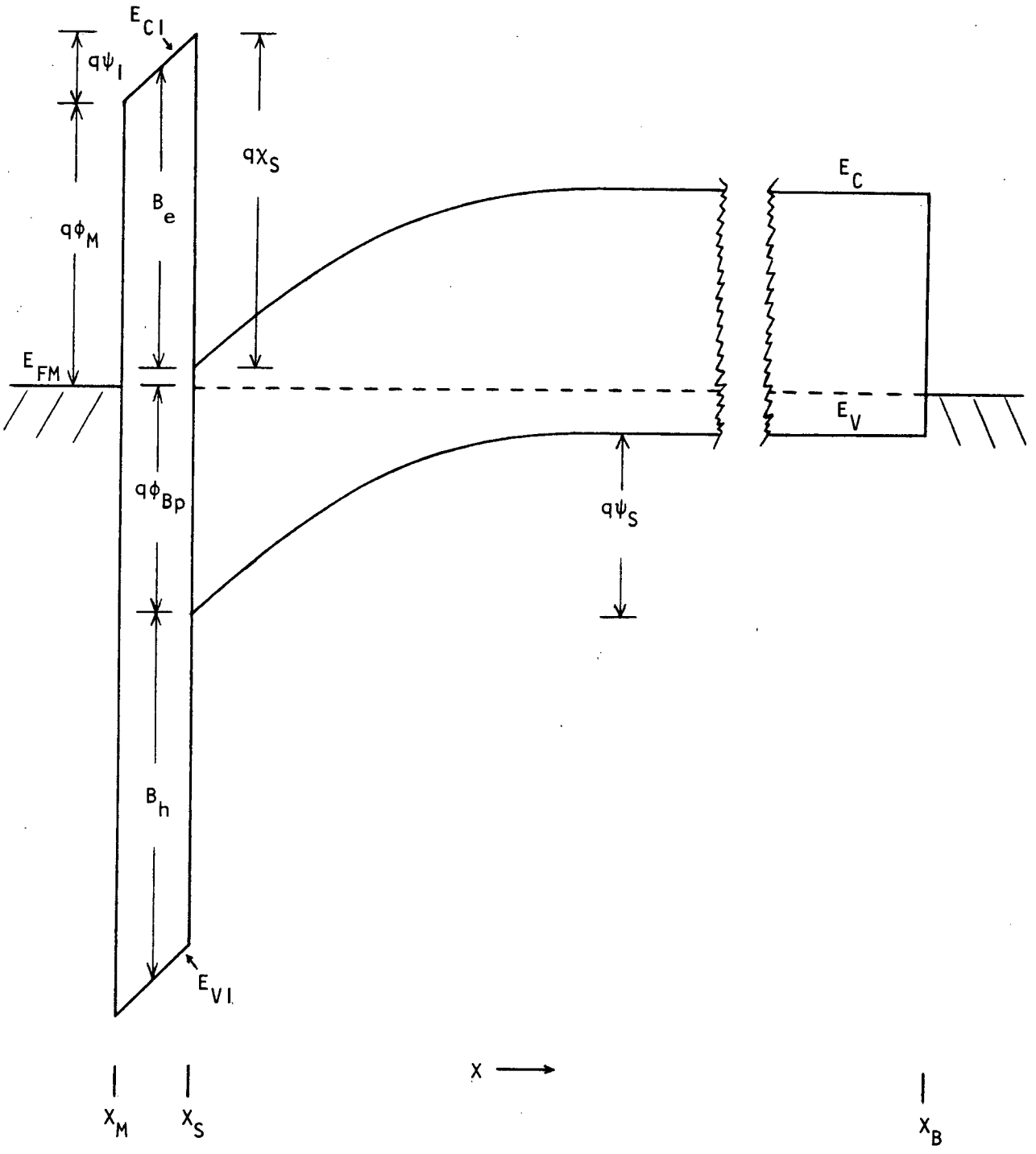

(b)

Figure 3.1(b)

that charge stored in electron states localized at the interface could play a major part in forming the barrier [66]. It is today generally accepted that the effects of both barrier metal work function and surface state charge can be of importance in determining the junction barrier height [67].

For Schottky diodes fabricated on freshly-etched silicon substrates the barrier metal work function and surface state charge are found to be of roughly equal importance in determining the barrier height. The interface state distribution for silicon surfaces prepared in this way is such that ϕ_{Bn} tends to be substantially larger than ϕ_{Bp}. ϕ_{Bn} is found to range from about 0.5 V for low work function metals to 0.9 V for high work function metals, while ϕ_{Bp} is usually less than 0.6 V [64]. It is thus not possible to obtain strong inversion at the surface of a p-type substrate, nor accumulation at the surface of an n-type substrate, in a conventional Schottky barrier diode.

For those MIS diodes formed on silicon substrates which have been oxidized at temperatures greater than about 400°C prior to metallization, the available experimental data indicate that the junction barrier height is determined almost exclusively by the barrier metal work function [68]. With an appropriate choice of barrier metal it is possible to obtain conditions ranging from accumulation to strong inversion at the semiconductor surface in an MIS diode prepared in this way, irrespective of the substrate doping type. It appears that the growth of the thin oxide layer which forms the interfacial insulator somehow passivates the silicon surface, greatly reducing the density of interface states.

Throughout this chapter, reference will be made to the electrostatic potential drop ψ_S appearing across the semiconductor and the drop ψ_I

across the insulator in an MIS or Schottky diode. For a diode formed on n-type material, ψ_S and ψ_I will be defined to be positive when these potential drops are in the direction shown in Fig. 3.1(a). Similarly, for a diode formed on a p-type substrate ψ_S and ψ_I will be defined as positive in Fig. 3.1(b). The equilibrium values of ψ_S and ψ_I will be denoted as ψ_{S0} and ψ_{I0}.

The application of a bias V to a Schottky or MIS diode displaces the fermi level at the base contact relative to the metal fermi level by an amount qV. (By convention, V is taken to be positive for forward bias). This in turn results in a change in the electrostatic potential distribution across the junction. Here the change $\Delta\psi_S$ in the potential drop across the semiconductor is defined by

$$\Delta\psi_S(V) = \psi_S(V) - \psi_{S0} \tag{3.1}$$

The change $\Delta\psi_I$ in the potential drop across the insulator is defined analogously. The relationship between $\Delta\psi_S$ and V is frequently written in the form

$$|\Delta\psi_S| \simeq V/n \tag{3.2}$$

where n is termed the "diode factor" or "ideality factor". (3.2) is useful because n is often found to be essentially constant over the normal operating bias range. For an ideal Schottky diode with a vanishingly thin interfacial layer, ψ_I must go to zero, so that n is unity. For the more general case in which the potential drop across the insulator can not be ignored, Card and Rhoderick have derived a simple expression

for n applicable when the semiconductor surface is depleted [26]. Unfortunately, no closed solutions for ψ_S and ψ_I are available for the case in which the semiconductor surface is strongly inverted. A possible technique for determining $\Delta\psi_I$ and $\Delta\psi_S$ in this case will be examined in Section 3.4 [17].

3.2 Tunnelling in Metal-Insulator-Semiconductor Structures

3.2.1 The Semiclassical Model of Conduction

A direct quantum-mechanical treatment of conduction in either Schottky barrier or MIS diodes is mathematically intractable. For this reason the analysis of current flow in these devices is invariably based on an extension of the semiclassical model of electron dynamics used, for example, in the development of the Boltzmann transport equation [69]. The main features of this model will now be very briefly reviewed.

The semiclassical model of electron dynamics is based on a knowledge of the band structure $E(\vec{k})$ in the independent electron approximation. Electrons moving under the combined influence of the periodic lattice potential $V(\vec{r})$ and an externally applied electromagnetic field are then represented as wavepackets constructed from the eigenstates of the independent electron Hamiltonian for the unperturbed crystal. Thus the wave function $\psi(\vec{r},t)$ of an electron is written in the form

$$\psi(\vec{r},t) = \int d^3k \; F(\vec{k},t) \; \psi_{\vec{k}}(\vec{r}) \qquad (3.3a)$$

where the states $\psi_{\vec{k}}$ are Bloch waves. If the externally applied fields are weak and slowly varying in time, intraband transitions can be ignored, allowing the expansion to be restricted to the states of a single band.

Further, in this case Wannier's theorem states that the envelope function F obeys an effective Schrodinger equation [69,70]

$$[E(-i\vec{\nabla}) + H_{ext}]F(\vec{r},t) = i\hbar[\partial F(\vec{r},t)/\partial t] \qquad (3.3b)$$

where H_{ext} is the contribution to the Hamiltonian from the external fields and

$$F(\vec{k},t) = (1/\sqrt{\Omega}) \int d^3r \exp(i\vec{k}\cdot\vec{r})\ F(\vec{r},t)\ , \qquad (3.3c)$$

Ω being the volume of a primitive cell.

In applications of semiclassical dynamics, reference is frequently made to a distribution function $f(\vec{k},\vec{r})$ which gives the probability that the independent electron state $|\vec{k}\rangle$ is occupied by an electron at position $\vec{r}$ [69]. This practice of assigning an electron both a wavevector $\vec{k}$ and a position $\vec{r}$ stands in apparent violation of the uncertainty principle. The practice is acceptable so long as $\vec{k}$ and $\vec{r}$ are taken to represent only the mean crystal momentum and mean position of a localized electron wavepacket.

3.2.2 Models for the Tunnelling Process

In the past, two conceptually distinct methods have been developed to determine the rate at which electrons tunnel through a thin insulator separating two conductors. (The conductors in question could be metals, semimetals or semiconductors; to simplify terminology, it will be assumed here that the junction has been formed between a metal and a semiconductor). In the original method developed by Bardeen [71] and later extended by Harrison [72], time-dependent perturbation theory is applied to esti-

mate the rate at which transitions between electron states in the metal and those in the semiconductor occur. This approach was employed by Card and Rhoderick [26], and later used by Green et al. [16,17] as the basis for their numerical analysis of the MIS tunnel diode. Here a more intuitively appealing method developed by Duke [73,74] is employed. To the level of approximation generally used, the two methods give mathematically identical expressions for the tunnel currents.

In Duke's approach, the tunnelling of electrons across a metal-insulator-semiconductor junction is treated in the same manner as the tunnelling of free electrons through a one-dimensional square potential barrier [75]. An electron approaching the interface from the semiconductor in Fig. 3.1 is represented by a travelling Bloch wave with wavevector $\vec{k}$. A solution to the Schrodinger equation is then sought which consists of this incident Bloch wave, a reflected wave returning to the right in the semiconductor, and a transmitted wave propagating to the left in the metal. If the energy E of the incident electron lies within the energy gap of the insulator, then in this region the electron wavefunction must have an exponential dependence on x. The ratio of the current density carried by the transmitted wave to that carried by the incident wave gives the probability that the electron will tunnel across the interface.

The form and amplitude of the transmitted and reflected electron waves are determined by the requirement that ψ and $\vec{\nabla}\psi$ be everywhere continuous. In general, these will not be simple Bloch waves. This can be seen by considering the solution to the Schrodinger equation at an abrupt interface between two regions with different lattice potentials. In each region, the solutions to the Schrodinger equation will be Bloch waves of the form

$$\psi_{\vec{k}}(\vec{r}) = u_{\vec{k}}(\vec{r}) \exp(i\vec{k}\cdot\vec{r}) \qquad (3.4)$$

where $u_{\vec{k}}(\vec{r})$ has the periodicity of the lattice. Since the functions $u_{\vec{k}}(\vec{r})$ will have different forms in the two regions, it will not in general be possible to connect a Bloch wave in one region with a single Bloch wave in the adjoining region in such a way that ψ is continuous across the boundary. Instead, a Bloch wave incident on the interface will give rise to transmitted and reflected waves with a spectrum of $\vec{k}$ values. The transmitted and reflected waves must, however, have the same energy as the incident wave.

In order to keep the description of tunnelling in the metal-insulator-semiconductor junction at a mathematically manageable level, it is invariably assumed that the lattice-periodic component $u_{\vec{k}}(\vec{r})$ of the Bloch wavefunction can be approximated by a constant in each region of the junction [72,76]. Thus the true Bloch wavefunction is replaced by a plane wave with the same wavevector. From this assumption it follows that the component $\vec{k}_t$ of the electron wavevector lying in the plane of the interface must be conserved during tunnelling. In other words, the incident, reflected and transmitted waves must all have the same value of $\vec{k}_t$.

Depending on the band structure of the metal, insulator and semiconductor, there may be several states available in each region of the junction with the same values of E and $\vec{k}_t$. As Fig. 3.2 indicates, in each band structure for every state with energy E, transverse wavevector $\vec{k}_t$ and velocity $v_x>0$, there must be at least one other state with the same E and $\vec{k}_t$, but with $v_x<0$. For simplicity, it will be assumed at first that only one such pair of states at the same energy and transverse wavevector exists in each region of the junction. The corrections to the

expressions for the tunnel currents required when this condition does not hold will be considered later.

In the independent electron approximation, the probability of an electron making a tunnelling transition from a state $|\vec{k}_S\rangle$ in the semiconductor to a state $|\vec{k}_M\rangle$ in the metal must equal the probability of the opposite transition, from $|\vec{k}_M\rangle$ to $|\vec{k}_S\rangle$ [73]. This probability will be denoted as $\theta(E,\vec{k}_t)$.

3.2.3 Expressions for the Tunnel Currents

If an electron in the semiconductor is to tunnel into the metal, the Pauli exclusion principle requires that the state which the electron is to enter in the metal be unoccupied. Taking this restriction into account, and summing the contributions from all occupied states in the semiconductor conduction band, it is found that the electron current component $J_{C\to M}$ flowing from the conduction band into the metal is given by [73]

$$J_{C\to M} = q \int_{v_x<0} d^3k \, \frac{2}{(2\pi)^3} \, v_x(\vec{k}) \, f_C(\vec{k},x_S) \, [1 - f_M(E,\vec{k}_t)] \, \theta(E,\vec{k}_t) \qquad (3.5)$$

where $f_C(\vec{k},x_S)$ is the distribution function for conduction band electrons evaluated at the semiconductor surface, and f_M is the distribution function for electrons in the metal. For most purposes it can be assumed that that f_M has its equilibrium form, and is thus identical to the Fermi-Dirac distribution function. The integral is to be carried out over all states $|\vec{k}\rangle$ in the conduction band with velocities directed towards the metal, and for which states in the metal with the same values of E and $\vec{k}_t$ exist.

Noting that

$$v_x(\vec{k}) = \frac{1}{\hbar}\frac{\partial E}{\partial k_x} \quad , \tag{3.6}$$

the integral over $\vec{k}$ appearing in (3.5) can be transformed to an integral over $\vec{k}_t$ and E. Since specifying E and $\vec{k}_t$ does not uniquely determine $\vec{k}$, some care is necessary in making this transformation. As noted above, for every state in the conduction band with energy E, transverse wavevector $\vec{k}_t$ and velocity component $v_x<0$, there must be at least one other state with the same E and $\vec{k}_t$, but with $v_x>0$. However, only the state with $v_x<0$ is to be included in computing J_{CM}. Therefore

$$J_{C\to M} = \frac{q}{2\pi^2\hbar}\int_{\substack{\text{cond.}\\ \text{band}}} dE \int_{S_{CM}} d^2k_t \; f_C(E,\vec{k}_t,x_S)\,[1 - f_M(E,\vec{k}_t)]\,\theta(E,\vec{k}_t) \tag{3.7}$$

where the region S_{CM} of the k_t plane is that in which states of energy E exist in both the metal and the semiconductor conduction band. Harrison [72] describes this region as the overlap of the "shadows" of the constant energy surfaces for the metal and the conduction band, where the shadow of a constant energy surface is defined to be its projection on a plane parallel to the interface. It is usually assumed that S_{CM} is equivalent to the shadows of the semiconductor constant energy surfaces alone. By making this assumption, any influence the band structure of the metal might have on the current flow is ignored. If, as suggested in Fig. 3.2, there is more than one pair of states in the conduction band with the same values of E and $\vec{k}_t$, then the contributions to $J_{C\to M}$ from the shadow of each branch of the constant energy surface must be taken into account. The shadows in the <100> direction for the various branches of a constant

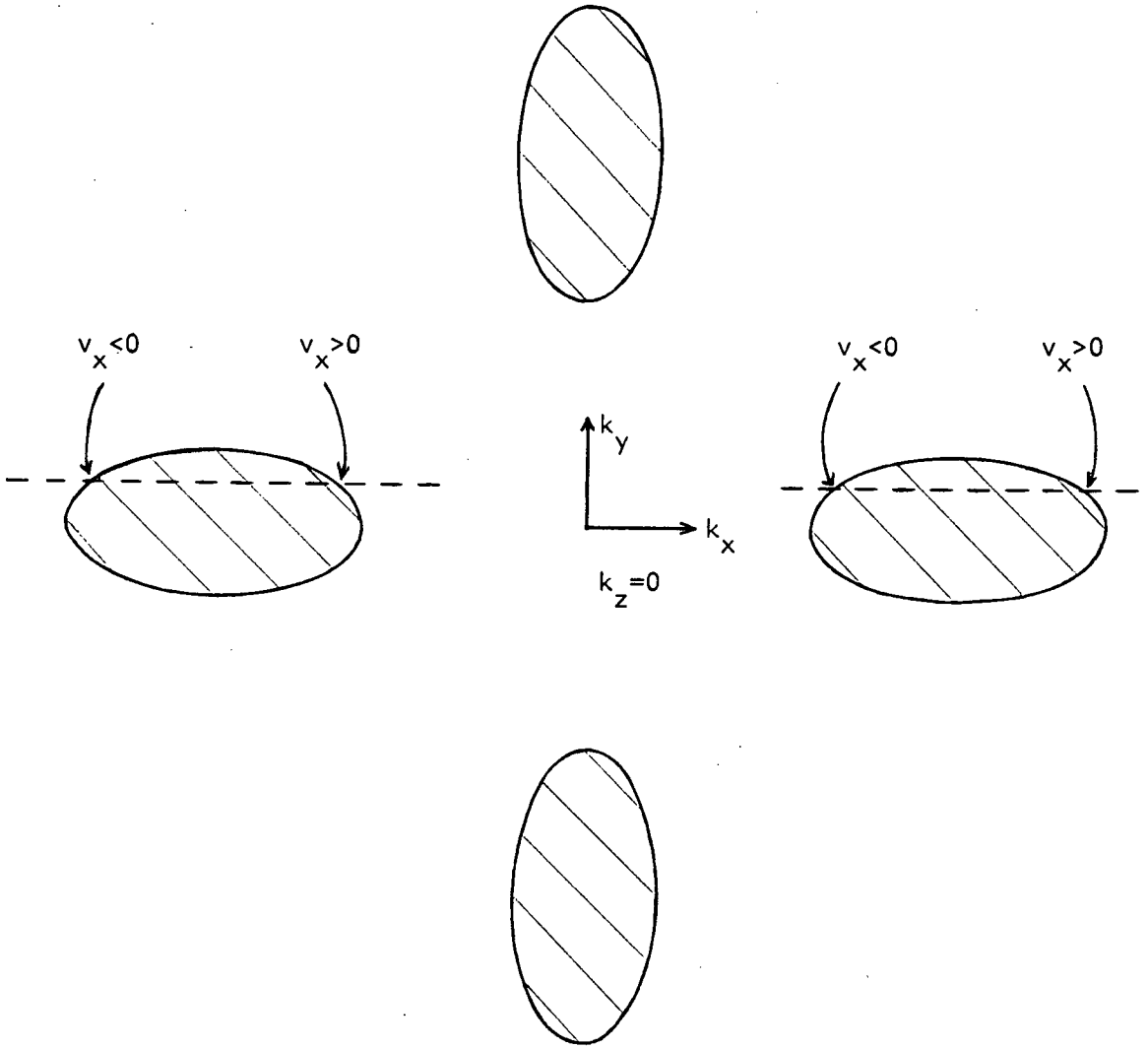

Figure 3.2 A slice through the constant energy surfaces for the silicon conduction band, showing that for each state with a given E, $\vec{k}_t$ and $v_x>0$, there exists at least one other state of the same E and $\vec{k}_t$, but with $v_x<0$.

energy surface close to the conduction band minimum for silicon are illustrated in Fig. 3.3.

By analogy with (3.7), the electron current component $J_{M\to C}$ flowing from the metal into the conduction band is given by

$$J_{M\to C} = \frac{-q}{2\pi^2 h} \int_{\substack{\text{cond.}\\ \text{band}}} dE \int_{S_{CM}} d^2k_t \; f_M(E,\vec{k}_t)\,[1 - f_C(E,\vec{k}_t,x_S)]\,\theta(E,\vec{k}_t) \; . \quad (3.8)$$

Adding (3.8) to (3.7), it is found that the net current J_{CM} flowing between the conduction band and the metal is given by

$$J_{CM} = J_{C\to M} + J_{M\to C} \quad (3.9)$$

$$= \frac{q}{2\pi^2 h} \int_{\substack{\text{cond.}\\ \text{band}}} dE \int_{S_{CM}} d^2k_t \,[f_C(E,\vec{k}_t,x_S) - f_M(E,\vec{k}_t)]\,\theta(E,\vec{k}_t) \; .$$

An analysis similar to that used to derive (3.7), (3.8) and (3.9) can be applied to obtain expressions for the current flows between the valence band and the metal. As is usually the case when dealing with a valence band, these current flows are most conveniently described in terms of the motion of holes [69]. From this viewpoint, the transfer of an electron from the metal to an unoccupied state in the valence band is equivalent to the emission of a hole from the semiconductor into the metal, while the transfer of a valence band electron to the metal is equivalent to the injection of a hole into the semiconductor. It is useful to define a hole distribution function f', which is related to the electron distribution function f by

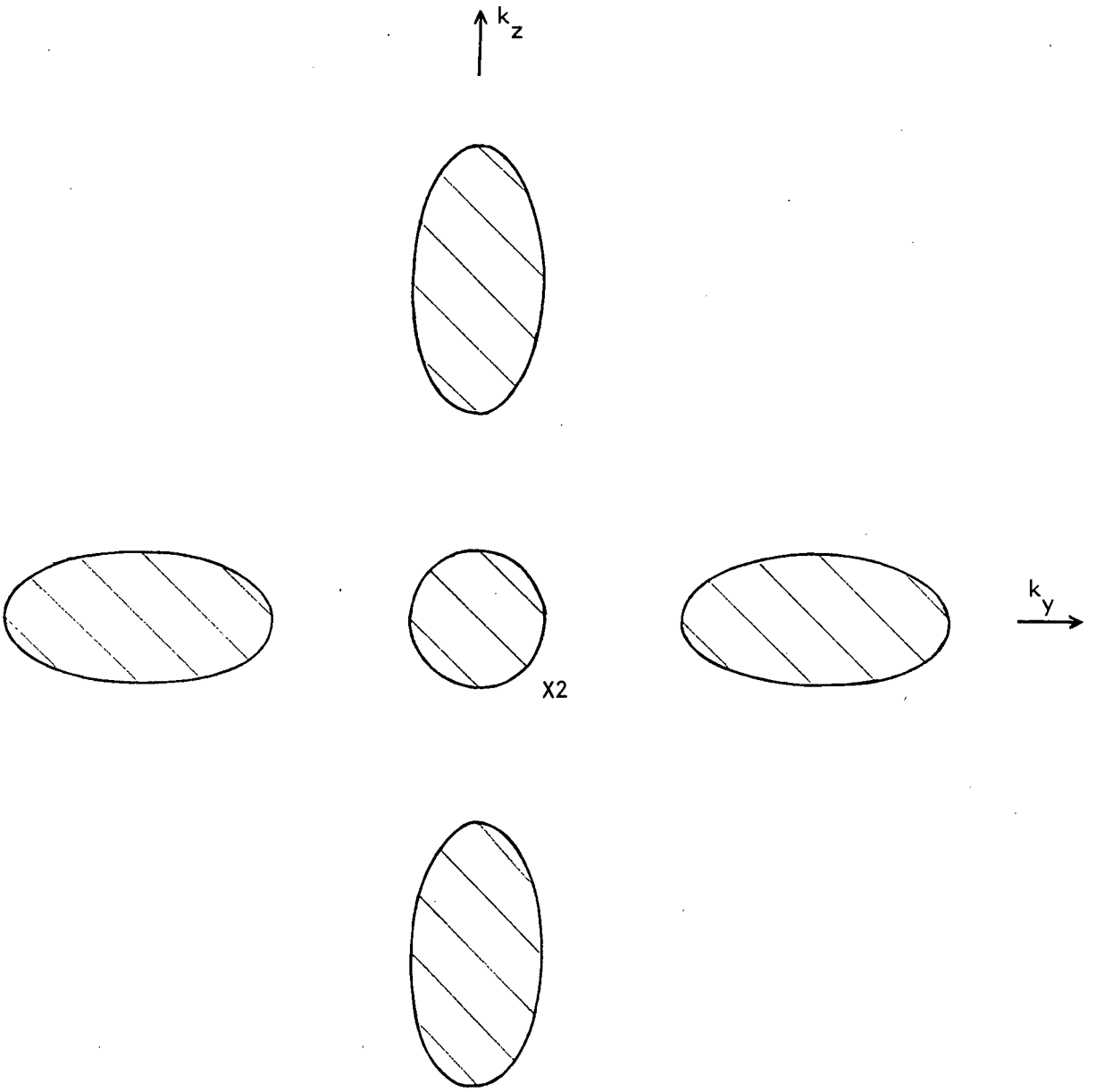

Figure 3.3 Shadow of the conduction band constant energy surfaces for a silicon sample of <100> orientation.

$$f' = 1 - f \ . \tag{3.10}$$

f' is thus the probability that a state in $\vec{k}$-space is "occupied" by a hole. In terms of f', the current flows between the valence band and the metal are given by

$$J_{V\to M} = \frac{-q}{2\pi^2 h} \int_{\substack{\text{val.}\\ \text{band}}} dE \int_{S_{VM}} d^2k_t \ f'_V(E,\vec{k}_t,x_S) \ [1 - f'_M(E,\vec{k}_t)] \ \theta(E,\vec{k}_t) \ , \tag{3.11}$$

$$J_{M\to V} = \frac{q}{2\pi^2 h} \int_{\substack{\text{val.}\\ \text{band}}} dE \int_{S_{VM}} d^2k_t \ f'_M(E,\vec{k}_t) \ [1 - f'_V(E,\vec{k}_t,x_S)] \ \theta(E,\vec{k}_t) \tag{3.12}$$

and

$$\begin{aligned} J_{VM} &= J_{V\to M} + J_{M\to V} \\ &= \frac{-q}{2\pi^2 h} \int_{\substack{\text{val.}\\ \text{band}}} dE \int_{S_{VM}} d^2k_t \ [f'_V(E,\vec{k}_t,x_S) - f'_M(E,\vec{k}_t)] \ \theta(E,\vec{k}_t) \ . \end{aligned} \tag{3.13}$$

3.2.4 An Estimate for the Tunnelling Probability Factor

The simplest possible estimate for $\theta(E,\vec{k}_t)$ is obtained through use of the WKB approximation [77,78]. In its conventional form, the WKB method is applied to determine approximate solutions to the full Schrodinger equation for the case in which the potential varies slowly over distances comparable to the electron wavelength. Within the insulator in the MIS junction, the potential experienced by an electron is a sum of the rapidly-varying lattice potential and a more slowly varying term associated with the electrostatic potential drop $\Delta\psi_I$ across the insulator,

so the WKB method can not be applied directly. However, it might be expected that the WKB approximation could still be applied to the effective Schrodinger equation (3.3) governing the envelope of the electron wavefunction. Proceeding in essentially this fashion, Harrison [72] has shown that the WKB expression for the probability of an electron tunnelling through the insulator is

$$\theta(E,\vec{k}_t) = \exp[-2 \int_{x_S}^{x_M} dx \ |k_{Ix}(E,\vec{k}_t,x)| \ ] \qquad (3.14)$$

where k_{Ix} is the imaginary x-component of the complex wavevector $\vec{k}_I$ within the insulator. (3.14) is identical to the expression the conventional WKB method gives for the probability of a free electron penetrating a potential barrier [78]. Just as in the free electron tunnelling problem, (3.14) is valid only if θ is small, so that only the exponentially decreasing solution to the Schrodinger equation need be considered within the insulator. Further, within the insulator the external potential must vary slowly over distances comparable to $|k_{Ix}|^{-1}$. In principle, for (3.14) to apply certain additional conditions on the behaviour of the potential near x_S and x_M must also be satisfied [78]. If these conditions are not met, the exponential appearing in (3.14) will be multiplied by a prefactor of order unity. However, since the tunnelling probability is dominated by the exponential, the exact value of this prefactor is of little importance.

In order to evaluate the tunnelling probability factor from (3.14), it is necessary to know the relationship between energy and complex wavevector $\vec{k}_I$ -- that is, the band structure -- for the evanescent states in the forbidden gap of the insulator. Previous theoretical analyses of

tunnelling in MIS structures [16,17,79] have generally assumed that E depends on $\vec{k}_I$ through a simple relationship first suggested by Franz [80]. The Franz dispersion relationship is

$$\frac{1}{k_I^2} = \frac{\hbar^2}{2m^*_{CI}[E - E_{CI}(x)]} + \frac{\hbar^2}{2m^*_{VI}[E_{VI}(x) - E]} \qquad (3.15)$$

where m^*_{CI} and m^*_{VI} are scalar effective masses associated with the conduction and valence bands in the insulator, and $E_{CI}(x)$ and $E_{VI}(x)$ are the energies of the conduction and valence band edges in the insulator. It should be noted that (3.15) predicts a negative value of k_I^2 for all states with energies within the forbidden gap. (3.15) reduces to a parabolic relationship between E and k_I near either band edge in the insulator. Once k_I^2 is known, k_{Ix} must be given by

$$k_{Ix} = \sqrt{k_I^2 - k_t^2} \quad . \qquad (3.16)$$

The probability of an electron tunnelling through a high potential barrier is not critically dependent on the shape of the barrier. Thus in evaluating the probability of an electron with energy near the middle of the insulator bandgap tunnelling between the metal and the semiconductor, it is reasonable to ignore the dependence of E_{CI} and E_{VI} on position. To this level of approximation, it is also reasonable to ignore any dependence θ might have on the bias applied to the junction.

In the semiconductor, only those states in the conduction band with wavevectors close to the bottom of the "valleys" will normally be occupied. It is thus reasonable to apply an approximate tunnelling probability

factor θ_{CM} to all transitions involving a given valley, where θ_{CM} is to be evaluated at the valley minimum. In general, if there are several valleys, the one with the smallest value of k_t will make the largest contribution to the tunnel current. For example, for silicon of <100> orientation, tunnel currents involving the conduction band will be dominated by transitions to and from states in the two valleys centered about $\vec{k}_t=0$. In this case a particularly simple estimate for θ_{CM} can be found. Assuming that the effective masses m^*_{CI} and m^*_{VI} appearing in (3.15) are equal to the free electron mass m, (3.14), (3.15) and (3.16) combine to give [79]

$$\theta_{CM} \simeq \exp[-2(2m/\hbar^2)^{1/2} B_e^{1/2} (1 - B_e/E_{gI})^{1/2} d] \qquad (3.17)$$

where B_e is the difference between the energy of the conduction band edge at the semiconductor surface and the mean energy of the insulator conduction band edge, d is the thickness of the insulator, and E_{gI} is the insulator bandgap energy.

By analogy to (3.17), an approximate tunnelling probability θ_{VM} applicable to all transitions involving states in the semiconductor valence band for which $\vec{k}_t\simeq 0$ can be defined. θ_{VM} is given by [79]

$$\theta_{VM} \simeq \exp[-2(2m/\hbar^2)^{1/2} B_h^{1/2} (1 - B_h/E_{gI})^{1/2} d] \qquad (3.18)$$

where B_h is the difference between the mean energy of the insulator valence band edge and $E_V(x_S)$.

Although the estimates for the tunnelling probability factor given above may appear very crude, there is little point in attempting to

generate more accurate expressions for $\theta(E,\vec{k}_t)$. In the vast majority of MIS and non-ideal Schottky junctions, the interfacial insulator is an amorphous film of silicon oxide grown by the low-temperature oxidation of the silicon substrate. At present, little reliable information is available concerning the structure or even the composition of layers grown in this way [81]. Such layers are thought to have the stoichiometry SiO_x, where $1 \lesssim x \leq 2$. In general, the band structure of an amorphous insulator is characterized by a mobility gap analogous in some respects to the forbidden energy gap in crystalline insulators. However, localized electron states can exist at energies within the mobility gap [82]. It is thus very likely that the bulk of the current flowing across the interface in an M-SiO_x-Si diode results from tunnelling transitions involving states within the mobility gap of the amorphous SiO_x layer. Assigning such SiO_x layers the band structure of crystalline SiO_2, as suggested in Fig. 3.1, is therefore hardly a realistic approximation. Further, there is no reason to believe that in a real diode the metal-insulator and semiconductor-insulator interfaces will be smooth over distances comparable to an electron wavelength. If the interfaces are rough on the atomic scale, the transverse wavevector $\vec{k}_t$ will not be conserved in tunnelling [72].

3.3 The Schottky Barrier Diode

Purely for notational convenience, it will be assumed that the junctions examined in this section and in the remainder of the chapter have been formed on n-type substrates, unless otherwise specified. The analysis developed applies equally well to p-type material if the roles of electrons and holes are interchanged.

3.3.1 The Majority Carrier Thermionic Emission Current

Under moderate forward bias, the current in a typical Schottky diode formed on n-type silicon is dominated by the emission of electrons from the conduction band into the metal. In most Schottky diodes this majority carrier flow is accurately described by the thermionic emission theory introduced by Bethe [10] in 1942. The thermionic emission theory is based on the assumption that the transmission coefficient θ appearing in equations (3.7-3.9) is equal to unity; thus the probability that an electron incident on the interface may suffer quantum-mechanical reflection is ignored. This assumption must always overestimate the electron flow, since even in an intimate metal-semiconductor contact part of the wave-packet representing the incident semiclassical electron will be reflected on collision with the interface [83]. However, if the interfacial layer is so thin that electrons can freely tunnel through it, the assumption of perfect transmission is not unreasonable.

In order to evaluate the net current flow J_{CM} between the conduction band and the metal from (3.9), it is necessary to know the distribution function for electrons at the semiconductor surface. As a first approximation, it is reasonable to assume that throughout the semiconductor the distribution function for conduction band electrons can be obtained by replacing the fermi energy E_F appearing in the Fermi-Dirac distribution function with a position-dependent quasi-fermi energy E_{Fn} [64]. The accuracy of this approximation is considered below. Measuring the electron energy E relative to the energy of the conduction band edge at the surface, (3.9) then becomes

$$J_{CM} = \frac{q}{2\pi^2 h} \int_0^{E_{max}} dE \, [f_C(E) - f_M(E)] \, \sigma_{CM}(E) \quad , \tag{3.19}$$

where

$$f_C(E) = \exp(-[E + E_C(x_S) - E_{Fn}(x_S)]/kT) \quad , \tag{3.20}$$

$$f_M(E) = \exp(-[E + E_C(x_S) - E_{FM}]/kT) \tag{3.21}$$

and the area σ_{CM} of the constant energy surface is given by

$$\sigma_{CM}(E) = \int_{S_{CM}(E)} d^2k_t \quad . \tag{3.22}$$

In writing (3.20) and (3.21), the Boltzmann limit to the Fermi-Dirac function has been taken. This is valid only if $E_C(x_S)$ lies above E_{FM} and $E_{Fn}(x_S)$ by at least kT. The upper limit on the energy integral can be raised to infinity without introducing appreciable error.

If there is a single valley in the conduction band, and if the effective mass tensor associated with this valley has one principal axis perpendicular to the interface, then for those states which have a significant probability of being occupied

$$E(\vec{k}) = \frac{\hbar^2}{2}\left[\frac{k_x^2}{m_x^*} + \frac{k_y^2}{m_y^*} + \frac{k_z^2}{m_z^*}\right] \quad . \tag{3.23}$$

Here m_x^*, m_y^* and m_z^* are the principal values of the effective mass [84]. In this case it can be seen immediately that the shadow of the constant energy surface is an ellipse, and that the shadow area is given by

$$\sigma_{CM}(E) = \frac{\pi\, 2\sqrt{m_y^* m_z^*}\, E}{\hbar^2} \quad . \tag{3.24}$$

It then follows that

$$J_{CM} = \frac{4\pi q\sqrt{m_y^* m_z^*}}{h^3} \int_0^\infty dE\ E\ [f_C(E) - f_M(E)] \tag{3.25}$$

$$= \frac{4\pi q m_e^* k^2}{h^3}\ T^2 \exp(-[E_C(x_S) - E_{Fn}(x_S)]/kT)$$

$$\cdot\ [1 - \exp(-[E_{Fn}(x_S) - E_{FM}]/kT)]$$

where

$$m_e^* = \sqrt{m_y^* m_z^*}\ . \tag{3.26}$$

For a conduction band valley in which the principal axes of the effective mass tensor have an arbitrary orientation relative to the interface, it is shown in Appendix B that (3.25) still holds, although the expression for m_e^* is more complicated than (3.26) [85]. If there is more than one valley, the contributions to J_{CM} from each valley must be summed.

Following Shockley's analysis of current flow in the pn diode [44], it is reasonable to base the computation of the electron thermionic emission current on the assumption that E_{Fn} is constant across the depletion region and the quasi-neutral base [86]. This situation is illustrated in Fig. 3.4, which gives the band diagram for the device of Fig. 3.1(a) when a forward bias V is applied. Once the electron current has been calculated, the methods outlined in Section 2.2 can be used to establish the self-consistency of this assumption on the constancy of E_{Fn}.

If E_{Fn} is constant across the semiconductor, then

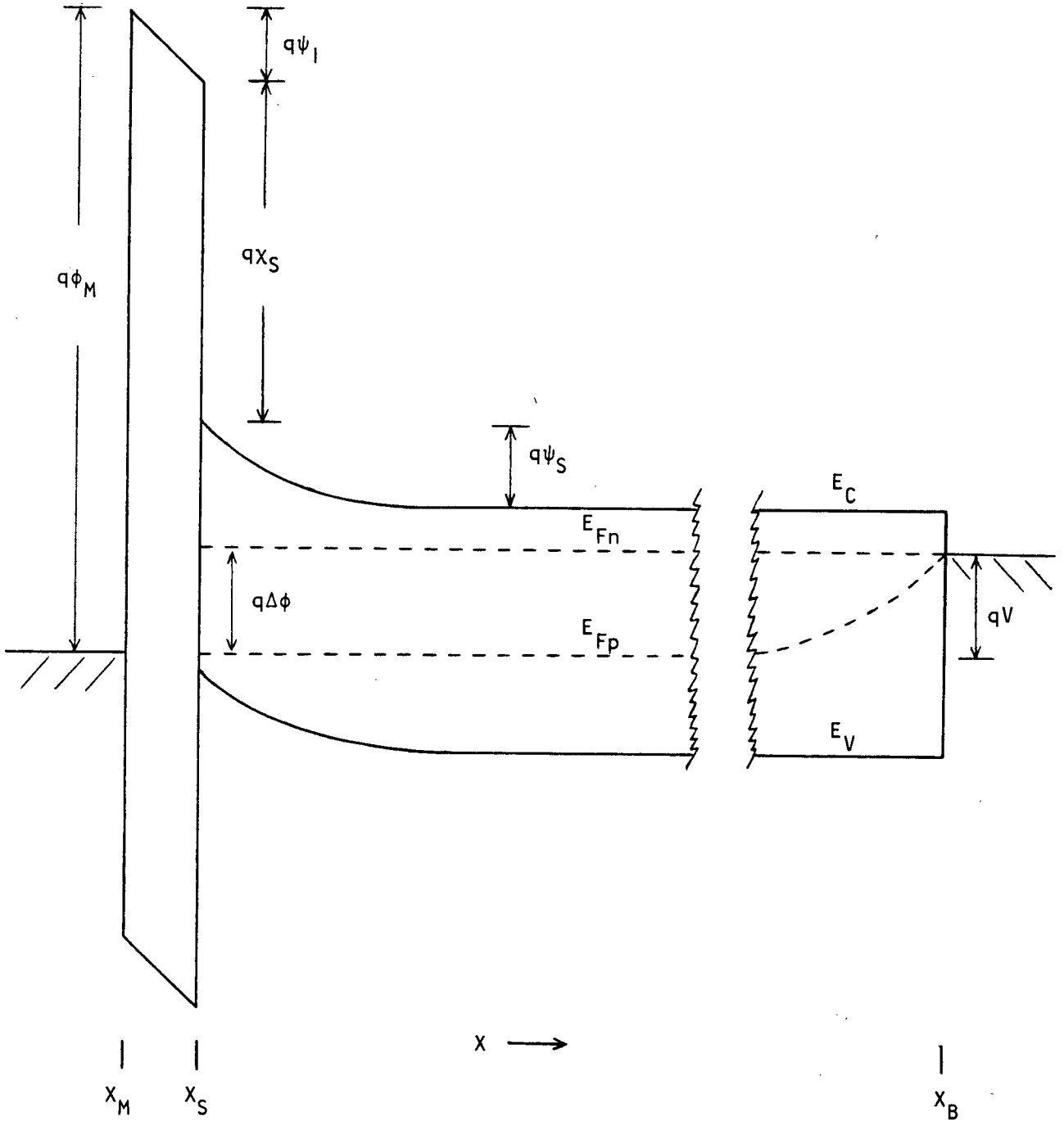

Figure 3.4 Band diagram for the device of Fig. 3.1(a) under moderate forward bias.

$$E_{Fn}(x_S) - E_{FM} = qV \tag{3.27}$$

and

$$E_C(x_S) - E_{Fn}(x_S) = q\psi_{S0} - q\Delta\psi_S + q\phi_0 = q\phi_{Bn} - \frac{qV}{n} \tag{3.28}$$

where $q\phi_0$ is the energy difference between the fermi level and the conduction band edge at the back contact. Defining the effective Richardson constant for electrons A_e^* by

$$A_e^* = \frac{4\pi q m_e^* k^2}{h^3} \quad , \tag{3.29}$$

(3.25) becomes

$$J_{Th}(V) = J_{CM} = A_e^* T^2 \exp(-q\phi_{Bn}/kT) \exp(qV/nkT) [1 - \exp(-qV/kT)]. \tag{3.30}$$

(3.30) is the conventional expression for the electron thermionic emission current, J_{Th} [87].

In deriving (3.30), it was assumed that the electron distribution in $\vec{k}$-space retains its equilibrium form throughout the semiconductor, even in the immediate vicinity of the interface. However, since a very large electron current flows across the interface into the metal when a forward bias V is applied to the diode, yet virtually no electrons enter the conduction band from the metal, it seems clear that the region near the surface must be depleted of electrons with $v_x>0$. Bethe [10] argued that this effect could be ignored provided the barrier potential drops by at least kT/q between the semiconductor surface and the plane $x=x_\lambda$, which by definition is separated from the surface by the mean free path

λ for electron-phonon collisions. The thermionic emission current is then envisaged as being composed of electrons scattered towards the interface from $x=x_\lambda$. Since relatively few electrons scattered from $x=x_\lambda$ will have sufficient energy to overcome the remaining portion of the barrier and reach the interface, the electron distribution at $x=x_\lambda$ should not be significantly influenced by the presence of the metal. For the case in which the effective mass tensor has one principal axis normal to the interface, at least, it can be shown that the expression for the thermionic emission current (3.30) is unaffected by this modification to the theory. As a general comment, the problem of selecting the correct form for $f_C(\vec{k},x_S)$ in the Schottky diode is still the subject of considerable controversy [88]. The quasi-equilibrium distribution function (3.20) is the most widely used approximation for f_C [86,89,90].

3.3.2 Minority Carrier Flow

By making approximations analogous to those used in the derivation of (3.25), an expression for the net current flow J_{VM} between the valence band and the metal for the Schottky diode can be obtained. This expression is

$$J_{VM} = -A_h^* T^2 \exp(-[E_{Fp}(x_S) - E_V(x_S)]/kT) \cdot [1 - \exp(-[E_{FM} - E_{Fp}(x_S)]/kT)] \tag{3.31}$$

where

$$A_h^* = \frac{4\pi q m_h^* k^2}{h^3} \quad . \tag{3.32}$$

It is often convenient to write (3.31) in the form

$$J_{VM} = -A_h^* T^2 \frac{p(x_S)}{N_V} \left[1 - \exp(-[E_{FM} - E_{Fp}(x_S)]/kT)\right] , \qquad (3.33)$$

which stresses the dependence of J_{VM} on the hole concentration $p(x_S)$ at the semiconductor surface.

For a typical Schottky diode formed on n-type silicon the semiconductor surface is inverted at equilibrium. There are therefore many unoccupied states at the semiconductor surface with energies near the valence band edge. Further, the band diagram of Fig. 3.1(a) indicates that there are also many occupied states in the metal at these energies. Thus from (3.11) and (3.12) the current components $J_{V\rightarrow M}$ and $J_{M\rightarrow V}$ flowing between the valence band and the metal must be extremely large, even though at equilibrium these two current components cancel exactly.

When a small forward bias is applied to a Schottky or MIS diode, the hole quasi-fermi level at the semiconductor surface must be displaced from the fermi level at the base contact by an amount $q\Delta\phi$, as shown in Fig. 3.4. ($\Delta\phi$ is defined to be positive when the minority carrier quasi-fermi level shifts so as to increase the minority carrier concentration at the surface). This displacement of $E_{Fp}(x_S)$ results in a net flow of holes from the metal into the semiconductor. The net hole current J_{VM} crossing the interface can be divided into a component J_{rg}, which accounts for recombination in the depletion region, and a component J_d, which accounts for recombination in the quasi-neutral base. J_{VM} must be equal to the hole current which would flow across the emitter/depletion region boundary of a P^+N homojunction diode formed on an identical substrate and subject to a forward bias $\Delta\phi$. (Minor differences in the width of the depletion region between the Schottky diode and the P^+N diode may

result in very small differences between the two hole currents; however, these differences can be ignored for all practical purposes). Thus

$$J_{VM} = J_{rg}(\Delta\phi) + J_{d}(\Delta\phi) \tag{3.34}$$

where analytic approximations for J_{rg} and J_{d} are given in (2.26) and (2.28). From Fig. 3.4, it is apparent that

$$E_{Fp}(x_S) - E_{FM} = q(V - \Delta\phi) \quad . \tag{3.35}$$

In terms of $\Delta\phi$ and V, (3.33) becomes

$$J_{VM} = -A_h^* T^2 \frac{p(x_S)}{N_V} \left(1 - \exp[q(V - \Delta\phi)/kT]\right) . \tag{3.36}$$

Fig. 3.4 suggests that the hole quasi-fermi level at the semiconductor surface should coincide with the fermi level in the metal [12,91], so that $\Delta\phi$ is equal to V. This "pinning" of $E_{Fp}(x_S)$ to E_{FM} can be explained by the following indirect argument. If $E_{Fp}(x_S)$ did not coincide with E_{FM}, but instead lay closer to the fermi level at the back contact, the balance between $J_{V\to M}$ and $J_{M\to V}$ would be destroyed. As a result, there would be an enormous net flow of holes from the metal into the semiconductor. If desired, the magnitude of this hole flow could be estimated from (3.36). The flow could be sustained only if the rate at which holes were injected into the semiconductor were matched by the rate at which these excess holes recombined with electrons in the depletion region and base. However, since $\Delta\phi$ is always less than or equal to V, an upper

bound on the hole recombination current is set by the sum of $J_{rg}(V)$ and $J_d(V)$. For a substrate with reasonable doping, mobilities, and carrier lifetimes, at moderate forward bias $J_{rg}(V)$ and $J_d(V)$ will both be extremely small compared to either $J_{M\to V}$ or $J_{V\to M}$. Thus the only possible steady-state solution is to have a condition of quasi-equilibrium between the metal and the holes at the semiconductor surface, which is equivalent to pinning $E_{Fp}(x_S)$ to E_{FM}. In fact, $E_{Fp}(x_S)$ will be displaced just enough from E_{FM} that the difference between $J_{V\to M}$ and $J_{M\to V}$ is equal to $J_{rg} + J_d$.

3.3.3 The Minority Carrier Injection Ratio

The minority carrier injection ratio γ of a Schottky barrier diode is defined to be the ratio of the minority carrier current crossing the boundary between the depletion region and the base to the total current flow. Thus

$$\gamma = \frac{J_d}{J_{Th} + J_{rg} + J_d} \xrightarrow[\text{large } V]{} \frac{J_d}{J_{Th} + J_d} \quad . \tag{3.37}$$

γ can readily be computed from the expressions for J_{Th}, J_d and J_{rg} given above. Calculations of precisely this type lead Scharfetter [12] to conclude that γ is extremely small for typical silicon Schottky diodes operated at moderate forward bias. In principle, however, if the junction barrier height were made large enough, J_{Th} could be made smaller than J_d. This condition would be achieved most easily with a lightly doped substrate, since J_d decreases as the doping level increases. For example, for a 10 Ωcm p-type substrate with a 10 μsec electron lifetime, a barrier height ϕ_{Bp} of approximately 0.99 V would be required to make J_{Th} equal

to J_d. Although such a high barrier height is not impossible in theory, it is far higher than the values of ϕ_B recorded for Schottky diodes fabricated using conventional techniques.

3.3.4 Current Flow Through Surface States

Up to this point, only the direct flow of carriers between the conduction and valence bands and the metal has been considered. If the surface state density is large, and if these states communicate readily with one or both bands and with the metal, there may be a third important current component resulting from electrons tunnelling between these states and the metal [16]. The magnitude of this current component is likely to be very sensitive to the density and distribution in energy of the surface states, which in turn depends critically on device fabrication procedures. For this reason, current flow through surface states will not be considered here.

3.4 Transition to the MIS Diode

If the interfacial insulating layer in the junction of Fig. 3.1(a) is made progressively thicker, a point will eventually be reached at which this layer can no longer be considered transparent to electrons. For theoretical purposes, it is useful to define this point as marking the transition from non-ideal Schottky diode to MIS diode. In an MIS diode, it is no longer reasonable to assume that the transmission coefficient $\theta(E,\vec{k}_t)$ is unity. In this section and in Section 3.5, for all tunnelling transitions involving the conduction band $\theta(E,\vec{k}_t)$ will be approximated by a constant, θ_{CM}. Similarly, all tunnelling transitions between the valence band and the metal will be described by a constant tunnelling probability factor θ_{VM}. Thus the expressions for the net

current flows between the semiconductor bands and the metal become

$$J_{CM} = \theta_{CM} A_e^* T^2 \exp(-q\phi_{Bn}/kT) \exp(qV/nkT) [1 - \exp(-qV/kT)] \qquad (3.38)$$

and

$$J_{VM} = -\theta_{VM} A_h^* T^2 \frac{p(x_S)}{N_V} (1 - \exp[q(V - \Delta\phi)/kT]) . \qquad (3.39)$$

Estimates for θ_{CM} and θ_{VM} in terms of the thickness and band structure of the insulator are given in equations (3.17) and (3.18). Crude as this model for the tunnelling process may appear, it is capable of explaining both the existence of minority carrier MIS diodes and, on a qualitative level, the main features appearing in the conduction characteristics of all MIS diodes.

In the previous section it was pointed out that in a Schottky diode the electron distribution function at the semiconductor surface is likely to deviate significantly from its equilibrium form. In an MIS diode, however, there is no doubt that $f(\vec{k},x_S)$ can be accurately approximated by the Fermi-Dirac function at moderate forward bias, since most electrons incident on the semiconductor surface are reflected.

3.4.1 The Minority Carrier MIS Diode

From (3.38) it follows that the electron thermionic emission current J_{Th} flowing in the MIS diode is reduced by a factor θ_{CM} relative to its value in a Schottky diode with the same barrier height. However, so long as $J_{V\to M}$ and $J_{M\to V}$ both remain large compared to the sum of the depletion region recombination current J_{rg} and the hole injection-diffusion current

J_d, then the condition of quasi-equilibrium between the metal and the holes at the semiconductor surface which held for the Schottky diode must still apply in the MIS junction. Thus at moderate forward bias $E_{Fp}(x_S)$ will be pinned to E_{FM} in the MIS diode [16]. Provided θ_{CM} is sufficiently small, in this bias regime the sum of J_{rg} and J_d will be much larger than J_{Th}. If this is the case, then a minority carrier MIS diode has been formed.

If the forward bias applied to the MIS diode is gradually increased, a bias point will eventually be reached at which the sum of J_{rg} and J_d becomes comparable to $J_{M\rightarrow V}$. Above this bias point, $E_{Fp}(x_S)$ will no longer be pinned to E_{FM}, but will instead lie closer to the fermi level at the base contact; thus in Fig. 3.4 $\Delta\phi$ becomes significantly smaller than V. Green et al. have termed this bias range the "tunnel limited" regime [16], since over this range the net hole current entering the semiconductor is limited by the rate at which holes are supplied by tunnelling across the insulator, rather than by recombination processes within the semiconductor. Correspondingly, the bias range in which $E_{Fp}(x_S)$ is pinned to E_{FM} is termed the "semiconductor limited" regime [16].

When operated in the semiconductor limited regime, the minority carrier MIS diode is electrically equivalent to a one-sided pn junction formed on an identical substrate. At the onset of the tunnel limited regime, the minMIS diode can be modelled approximately as a pn junction connected in series with a voltage-dependent resistance. Further into the tunnel limited regime, both minority and majority carrier flows may be important. The maximum forward bias which can be applied to the MIS diode before the tunnel limited regime is entered depends on θ_{VM}, and hence on the insulator thickness [16].

The dark current-voltage characteristics for a hypothetical set of MIS diodes fabricated on identical substrates but with different insulator thicknesses are sketched in Fig. 3.5 [16]. For all the diodes, at very small forward bias the characteristics are dominated by recombination in the depletion region. As the forward bias is increased, the characteristic of the device with the thinnest insulator rises above those of the other diodes. In this device, a substantial fraction of the dark current flowing at moderate forward bias results from majority carrier thermionic emission. For the other devices, the current flow at moderate forward bias is dominated by minority carrier injection-diffusion in the quasi-neutral base. These devices are thus minority carrier MIS diodes. If the forward bias applied to the minMIS diodes is increased still further, the minority carrier flows eventually become tunnel limited. The transition from the semiconductor limited regime to the tunnel limited regime occurs first for those devices with the thickest interfacial layers.

The "quality" of a minority carrier MIS diode depends on both the ratio of the minority carrier current component to the majority carrier component in the semiconductor limited regime, and on the maximum forward bias which can be applied before the tunnel limited regime is entered. Devices of the highest quality are formed when the tunnelling probability coefficient for the minority carrier band is greater than that for the majority carrier band, and when the semiconductor surface is strongly inverted. Both these conditions help to suppress the majority carrier thermionic emission current, while simultaneously strengthening the carrier flows which maintain the state of quasi-equilibrium between the metal and the minority carriers at the semiconductor surface. Although

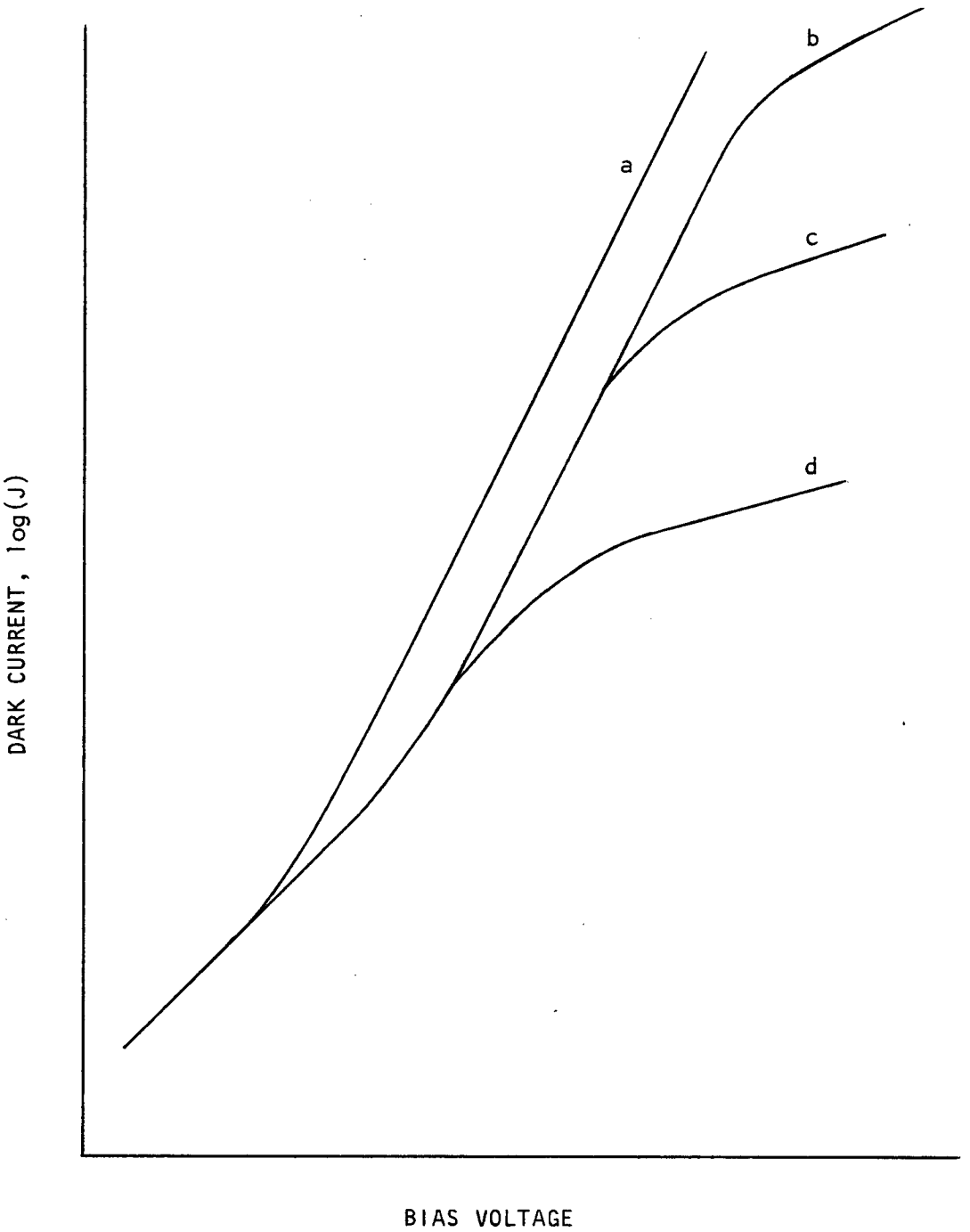

Figure 3.5 Dark current-voltage characteristics for MIS diodes with various insulator thicknesses; insulator thickness increases a→d.

little can be done to control the ratio of θ_{CM} to θ_{VM}, an appropriate choice of barrier metal work function can assist in achieving high junction barrier heights and hence strong surface inversion.

3.4.2 An Analytic Solution for the Potentials and Current Flows

Up to this point nothing has been said regarding the electrostatic potential distribution across the MIS junction. In the case of a thick-insulator MOS capacitor, it is possible to integrate Poisson's equation over the semiconductor to obtain an expression for the electric field $\mathcal{E}(x_S^+)$ just inside the semiconductor surface [92]. Green et al. [17] have shown that this technique can be extended to the case of the MIS tunnel diode. Here the results obtained by Green et al. will be derived using a somewhat less rigorous argument.

For a uniformly-doped n-type substrate, Poisson's equation becomes

$$d^2\psi/dx^2 = -(q/\varepsilon_S)\ [p - n + N_D]\ . \tag{3.40}$$

If ψ and the quasi-fermi potentials ϕ_n and ϕ_p are measured relative to an appropriate reference point, in the non-degenerate case the carrier concentrations are given by

$$n = n_i\ \exp[q(\psi - \phi_n)/kT] \tag{3.41}$$

and

$$p = n_i\ \exp[q(\phi_p - \psi)/kT]\ . \tag{3.42}$$

Provided the net current flow through the diode is small, the potential drop across the quasi-neutral base can be ignored. Further, in Chapter 2

it was argued that each quasi-fermi level should be essentially constant across that part of the depletion region in which the corresponding carrier concentration is large. However, in evaluating the right-hand side of (3.40) the charge contribution from each free carrier need be considered only where the concentration of that carrier is large. Thus for the purpose of evaluating (3.40), it is reasonable to assume that the quasi-fermi levels are constant across the depletion region. Applying the same technique used to solve (3.40) for the MOS capacitor [92], it is then found that

$$[\mathcal{E}(x_S^+)]^2 = (2kT/\varepsilon_S)\,[p(x_S) - p(x_n) + n(x_S) - n(x_n) + N_D(q\psi_S/kT)] \quad (3.43)$$

where the plane x_n marks the boundary between the depletion region and the quasi-neutral base. Under normal operating conditions, the terms $p(x_n)$ and $n(x_S)$ can be ignored. Further, $n(x_n)$ is very nearly equal to N_D. Thus

$$[\mathcal{E}(x_S^+)]^2 \simeq (2kT/\varepsilon_S)\,[p(x_S) + N_D(q\psi_S/kT - 1)] \; . \quad (3.44)$$

$p(x_S)$ is related to the equilibrium hole concentration p_{n0} in the quasi-neutral base by

$$p(x_S) = p_{n0} \exp(q\Delta\phi/kT) \exp(q\psi_S/kT) \; . \quad (3.45)$$

If the charge stored in surface states can be ignored, the electrostatic potential drop ψ_I across the insulator is related to $\mathcal{E}(x_S^+)$ by

$$\psi_I = \mathcal{E}(x_S^+)\; d\; \varepsilon_S/\varepsilon_I \; , \quad (3.46)$$

where d is the thickness of the interfacial layer. From Fig. (3.4),

$$\phi_M = V + \phi_0 + \psi_S + \chi_S + \psi_I \ . \tag{3.47}$$

Taken together, equations (3.34), (3.39), (3.44), (3.45), (3.46), and (3.47) are sufficient to uniquely determine the values of ψ_I, ψ_S, $p(x_S)$ and $\Delta\phi$ in the MIS diode at any operating point. Unfortunately, there is no closed solution for this system of coupled non-linear equations. However, a considerable simplification of the system is possible. (3.44), (3.45), (3.46) and (3.47) can be combined to eliminate $p(x_S)$ and ψ_I, giving

$$\phi_M = V + \phi_0 + \chi_S + \psi_S \tag{3.48}$$

$$+ d\left[\frac{2kT\varepsilon_S}{\varepsilon_I^2}\right]^{1/2} [p_{n0} \exp(q\psi_S/kT) \exp(q\Delta\phi/kT) + N_D(q\psi_S/kT - 1)]^{1/2} \ .$$

At equilibrium, $\Delta\phi$ and V must both be zero. In this case (3.48) reduces to a single transcendental equation for ψ_{S0}, which can be solved iteratively.

(3.34) and (3.39) can be combined to give

$$-J_{VM0} \frac{p(x_S)}{p_0(x_S)} (1 - \exp[q(V - \Delta\phi)/kT]) = J_{rg}(\Delta\phi) + J_d(\Delta\phi) \tag{3.49a}$$

where $p_0(x_S)$ is the surface hole concentration at equilibrium and the constant J_{VM0} is given by

$$J_{VM0} = \frac{\theta_{VM} A_h^* T^2 p_0(x_S)}{N_V} \quad . \tag{3.49b}$$

(3.49) is simply a statement of hole current continuity at the semiconductor surface. Provided the net hole current entering the semiconductor is not zero, (3.49) can be solved for $p(x_S)$ in terms of $\Delta\phi$, and then (3.45) can be used to solve for ψ_S in terms of $\Delta\phi$. Substituting the resulting expression for ψ_S in (3.48) yields a single transcendental equation for $\Delta\phi$, which can be solved by iteration. Once $\Delta\phi$ is known, ψ_S, $p(x_S)$, ψ_I and the current flows across the interface can be found immediately at any bias point V.

Following the above procedure, reasonably accurate approximate analytic solutions for the current flows and potential drops in the MIS diode can be obtained, even for operation in the tunnel limited regime. This analytic treatment of the MIS junction is similar to that developed by Card and Rhoderick [26-28]. However, the method proposed here takes into account the possibility of strong inversion at the semiconductor surface, a matter which was overlooked by Card and Rhoderick. In contrast to the approach taken here, and to that followed by Card and Rhoderick, Green et al. [16,17,22-25] chose to rely entirely on numerical analysis to solve for the carrier concentrations, potentials and current flows in the MIS diode. In this numerical approach, a technique similar to that outlined in Appendix A is used to solve the five basic equations governing the carrier concentrations and electrostatic potential in the semiconductor, subject to the boundary conditions imposed by (3.38), (3.39), and (3.47).

Even though no general analytic solution for the potential distribution in an MIS junction is available, some important conclusions

concerning the behaviour of the electrostatic potential and the carrier concentrations can be drawn for the case in which $E_{Fp}(x_S)$ is pinned to E_{FM}. In particular, it can be shown by the following indirect argument that under the application of a forward bias V the hole concentration at the semiconductor surface can not fall below its equilibrium value if $E_{Fp}(x_S)$ coincides with E_{FM} [16]. From (3.47), when a bias V is applied to the MIS diode, $\Delta\psi_I$ and $\Delta\psi_S$ must satisfy the relationship

$$V = -\Delta\psi_I - \Delta\psi_S \ . \tag{3.50}$$

The hole concentration at the surface could decrease only if $-\Delta\psi_S$ were greater than V, for if $E_{Fp}(x_S)$ is pinned to E_{FM}, it follows that $E_{Fp}(x_S)$ must be displaced from the fermi level at the back contact by an amount qV. But with this condition on $\Delta\psi_S$, (3.50) could be satisfied only by having $\Delta\psi_I$ positive. However, had the surface become less inverted, the potential drop across the insulator would be smaller than at equilibrium. In this case $\Delta\psi_I$ would be negative, which is a contradiction. Therefore if $E_{Fp}(x_S)$ is pinned to E_{FM}, (3.50) can be satisfied only by having the surface concentration of holes remain at its equilibrium value or increase. In fact, the numerical analysis carried out by Green et al. has shown that the hole concentration at the semiconductor surface remains very close to its equilibrium value until the tunnel limited regime is entered. It should be noted that this is exactly opposite to the behaviour expected for a thick-insulator MOS capacitor. It follows that $\Delta\psi_S$ is essentially equal to V throughout the semiconductor limited regime. Thus the diode factor n defined in (3.2) is effectively unity for a minority carrier MIS diode operated in this regime.

3.5 The MIS Solar Cell

3.5.1 Light Coupling into the Semiconductor

The first problem which must be overcome in order to form an efficient Schottky barrier or MIS solar cell is the coupling of light into the semiconductor. In the earliest MIS cells, a partial solution to this problem was achieved by making the evaporated barrier metal layer so thin as to be semi-transparent. The thin barrier layer was then overlaid with a thick contact grid, as illustrated in Fig. 3.6(a). However, this solution was far from ideal. From the viewpoint of electrical properties alone, the best MIS solar cells are those formed by depositing low work function metals such as aluminum, chromium or magnesium on p-type silicon [19]. Unfortunately, these low work function metals are very strong absorbers of visible light; for example, Hovel [93] has calculated that even when overlaid with an optimized anti-reflection coating, a 75 Å thick layer of aluminum can be expected to transmit only about 60% of incident light at visible wavelengths into a silicon substrate.

The transmittance of evaporated layers of low work function metals can be increased to some extent by partial oxidation during deposition [35]. This partial oxidation is easily accomplished by carrying out the evaporation slowly under a relatively high oxygen pressure. However, the incorporation of oxygen may produce deleterious changes in the work function of the layer. Alternatively, a composite barrier layer can be formed in which an ultra-thin layer of low work function metal is overlaid with a reasonably transparent layer of high work function metal. If the components are correctly chosen, the resulting stack may have high conductivity, high optical transmittance, and a work function in the desired range. Following this approach, Anderson *et al.* have fabricated MIS cells

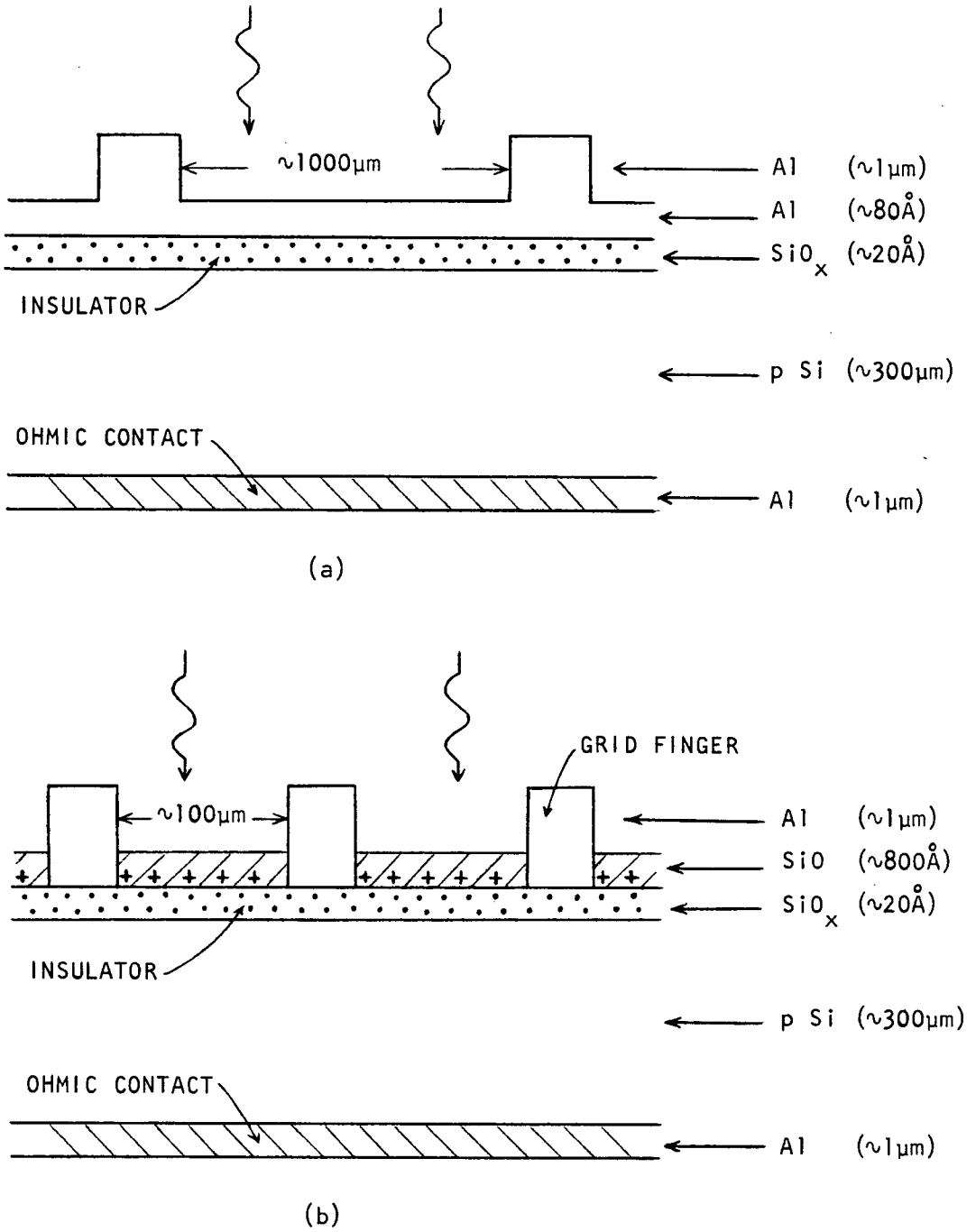

Figure 3.6 (a) Structure of MIS solar cell with thin, semi-transparent barrier layer.
(b) Structure of inversion layer cell.

with the structure 10Å Cr - 60Å Cu - 30Å Cr - SiO_x - pSi giving photocurrent densities as high as 26 mA/cm^2 [94]. In this structure, the chromium layer closest to the silicon induces the junction, while the copper provides reasonable sheet conductivity without a serious loss in transmittance. The photocurrent recorded by Anderson et al. is probably close to the upper limit which can be achieved with semi-transparent barrier metal layers.

Recently Godfrey and Green [95,96] and Thomas et al. [97] have produced inversion layer cells of exceptionally high efficiency incorporating MIS junctions. In the inversion layer cell the MIS junction covers only 10 to 20% of the surface, and functions as a contact grid (see Fig. 3.6(b)). A thin layer of dielectric is deposited over the rest of the surface in such a way that a high concentration of fixed positive charge is present near the interface (this can easily be accomplished by the thermal evaporation of SiO). The fixed charge in the dielectric induces an inversion layer at the silicon surface, in effect creating a very shallow induced junction. If the thickness and index of refraction of the dielectric are selected to minimize reflection, virtually all light incident on the cell can be transmitted into the substrate. As a result, photocurrent densities close to the theoretical maximum for silicon can be achieved. Although the inversion layer cell will not be given further consideration in this thesis, the structure offers a means of utilizing MIS junctions to form cells with efficiencies equal to or surpassing those of the best homojunction devices.

For the remainder of this section, it will be assumed that a means has been found to efficiently couple incident light into the semiconductor in MIS solar cells. Although the most efficient MIS cells reported

to date have been fabricated on p-type substrates [19], cells formed on n-type material will be considered here for consistency with Sections 3.3 and 3.4. It will be assumed from the outset that the barrier metal has been chosen to give strong inversion of the semiconductor surface at equilibrium. The relationship between cell performance and the thickness of the interfacial layer will then be considered.

3.5.2 Optimally Efficient MIS Cells

In order to attain the highest possible open-circuit voltage in an MIS solar cell, the interfacial layer must be thick enough to suppress the majority carrier thermionic/emission dark current component to negligible levels. However, in order to obtain high fill factors the insulator must simultaneously be thin enough that a net current equal in magnitude to the one-sun photocurrent can flow between the minority carrier band and the metal without significant displacement of the minority carrier quasi-fermi level at the surface from E_{FM}. This is equivalent to requiring that the minority carrier flow in the cell be semiconductor limited up to current densities comparable to 30 mA/cm^2. If these two conditions on insulator thickness can be met, then the characteristics of the MIS cell will be essentially the same as those of an ideal one-sided homojunction cell with a very shallow emitter region formed on an identical substrate [98]. In fact, the performance of the MIS cell is likely to be slightly better than that of the homojunction cell, since the carrier lifetimes and mobilities in the inversion layer of the MIS cell will not have been degraded by heavy doping effects. As a result, carriers photogenerated very near the silicon surface by short-wavelength photons will have a higher probability of crossing the depletion region and contributing to the photocurrent in the MIS cell [99]. Similarly,

the dark current component resulting from recombination near the surface should be smaller in the MIS cell than in the homojunction cell.

In Chapter 2 it was found that the superposition principle should provide an excellent approximate description of a silicon homojunction cell operated in the low-level injection regime. It follows that the superposition principle should also be applicable within the semiconductor in a minority carrier MIS solar cell. Therefore the net hole flow from the semiconductor surface into the depletion region and base must be given by

$$J_{VM} = J_{rg}(\Delta\phi) + J_{d}(\Delta\phi) - J_{upc} \ . \tag{3.51}$$

The requirement of hole current continuity at the surface then gives

$$-J_{VM0} \frac{p(x_S)}{p_0(x_S)} \left(1 - \exp[q(V - \Delta\phi)/kT]\right) = J_{rg}(\Delta\phi) + J_{d}(\Delta\phi) - J_{upc} \ , \tag{3.52}$$

which replaces (3.49) for an illuminated cell. Assuming that the majority carrier thermionic emission current is negligible, J_{VM} must be equal to the terminal current $J_L(V)$. If $E_{Fn}(x_S)$ is pinned to E_{FM} at all operating points, then $\Delta\phi$ is always equal to the bias V applied at the terminals. In this case, superposition will hold at the cell terminals.

3.5.3 The Characteristics of Thick-Insulator Cells

When the insulator in a minMIS solar cell becomes thick enough to seriously impede the flow of a current J_{VM} comparable in magnitude to the one-sun photocurrent, the cell conversion efficiency is reduced. The first performance parameter to be degraded is the fill factor, followed by the short-circuit current [25]. In principle, there should be no degradation

in open-circuit voltage, so long as the majority carrier thermionic emission current remains negligible. The band diagram for a thick-insulator MIS cell exposed to one-sun illumination at terminal short-circuit is shown in Fig. 3.7. In order to support the hole photocurrent flowing into the metal, $E_{Fp}(x_S)$ must be displaced from E_{FM}. This displacement of $E_{Fp}(x_S)$ has two consequences. First, in order to satisfy (3.48) and (3.45), the hole concentration at the semiconductor surface must increase dramatically over its equilibrium value. Secondly, from (3.51) it can be seen that the short-circuit current for the thick-insulator cell must be less than that for a cell in which $E_{Fp}(x_S)$ is always pinned to E_{FM}. However, unless the insulator is excessively thick, this suppression of J_{sc} should be insignificant. As long as $\Delta\phi$ at short-circuit is roughly 100 mV or more less than V_{oc}, J_{sc} will be very nearly equal to J_{upc}.

When a small forward bias V is applied to the illuminated thick-insulator cell, $E_{Fp}(x_S)$ is displaced even further from the fermi level at the back contact than at short circuit. If $\Delta\phi$ at short-circuit was small compared to V_{oc}, it is possible to apply a fairly large forward bias before $J_L(V)$ drops significantly below J_{sc}. However, a bias point is eventually reached at which $\Delta\phi$ is comparable to V_{oc}, and any further increase in forward bias past this point causes a sharp drop in current output. As J_{VM} decreases, $E_{Fp}(x_S)$ moves closer to E_{FM}, while the surface hole concentration drops rapidly towards its equilibrium value. At terminal open-circuit J_{VM} is zero, so $E_{Fp}(x_S)$ must align with E_{FM} regardless of insulator thickness. V_{oc} should therefore be independent of insulator thickness.

Fig. 3.8 shows the current-voltage characteristics under one-sun illumination for a set of MIS solar cells with various insulator thick-

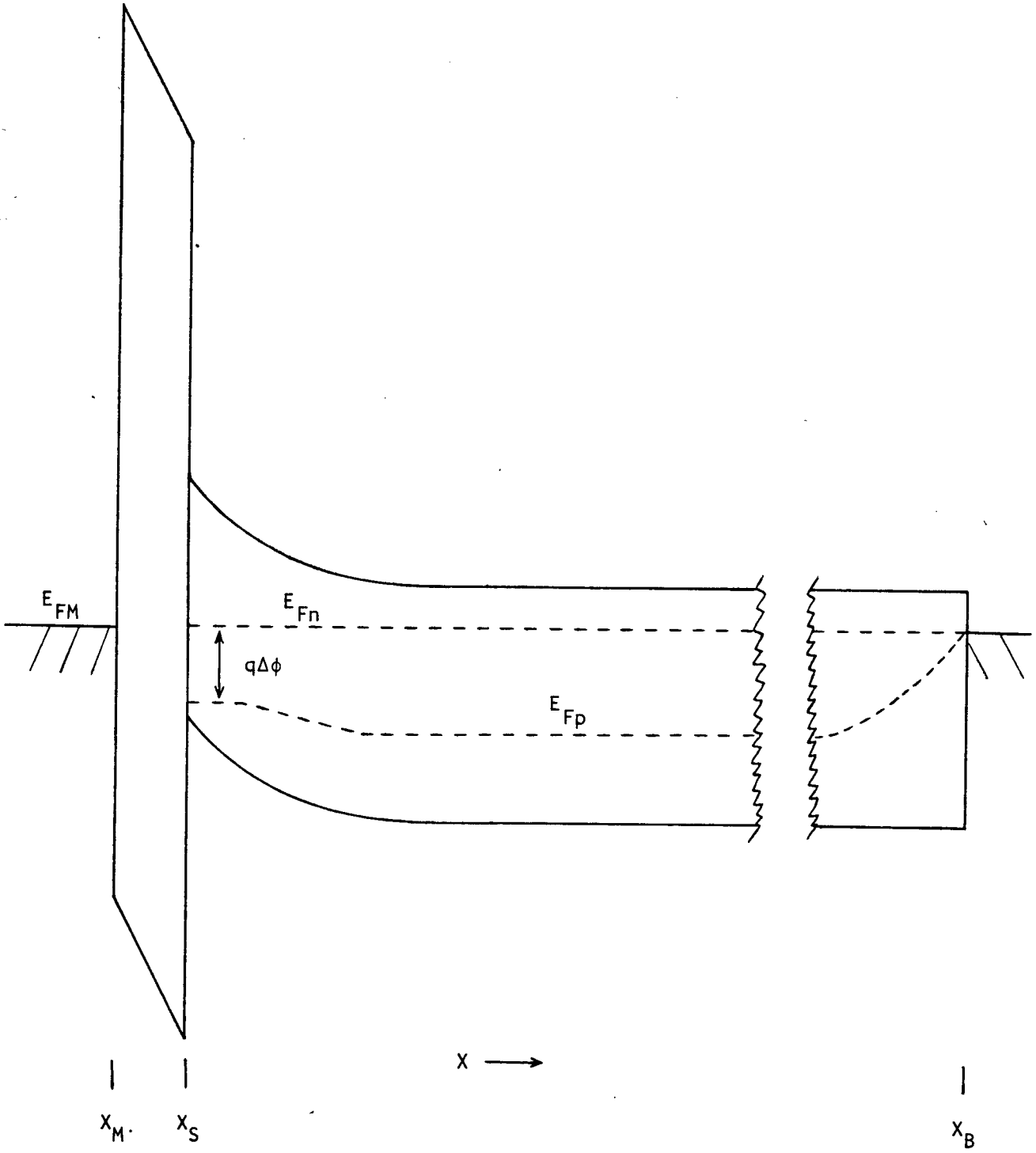

Figure 3.7 Band diagram for thick-insulator MIS cell at terminal short-circuit under one-sun illumination.

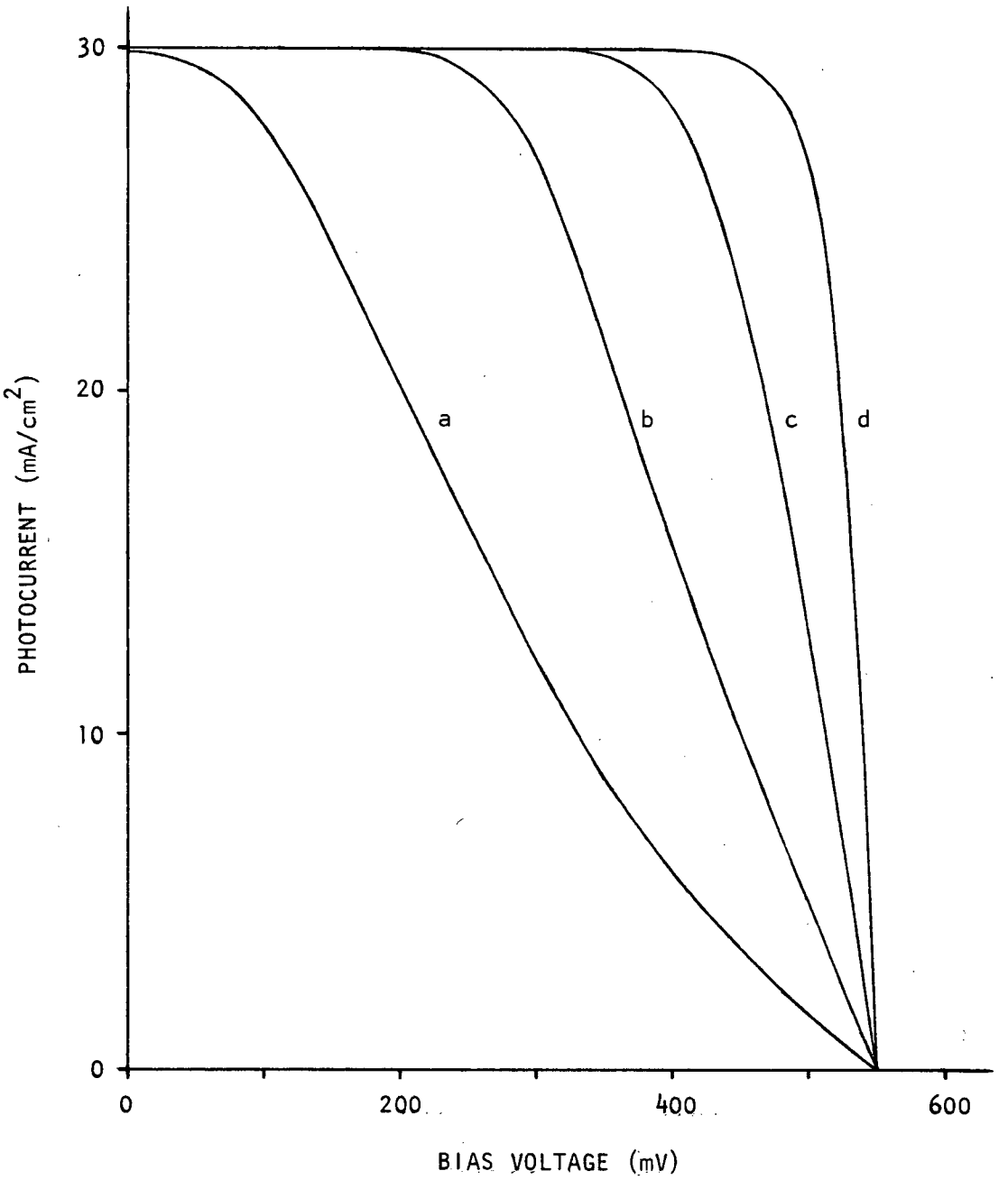

Figure 3.8 Illuminated current-voltage characteristics for MIS solar cells with various insulator thicknesses, as predicted by theory. For all cells $p_{0_2}(x_s)=10^{18}cm^{-3}$, d=20Å, V_{oc}=550mV, $\varepsilon_I=3\varepsilon_0$, and J_{upc}=30mA/cm^2.
(a) J_{VM0}=1mA/cm^2. (b) J_{VM0}=3mA/cm^2. (c) J_{VM0}=10mA/cm^2.
(d) $J_{VM0}\to\infty$.

nesses. These characteristics were generated using iterative techniques to simultaneously solve (3.45), (3.48) and (3.52), as outlined in Section 3.4. The cell material properties used in this calculation are listed in the figure caption. Rather than setting ϕ_M and χ_S directly, the equilibrium hole concentration at the semiconductor surface $p_0(x_S)$ was specified. Both the depletion region recombination current J_{rg} and the majority carrier thermionic emission current J_{Th} were assumed to be negligible. In this case, the cell open-circuit voltage depends only on the magnitude of the hole injection-diffusion dark current J_d. The expression used to compute $J_d(\Delta\phi)$ was that given in (2.28). J_{0d} was set to give a specified open-circuit voltage.

The most remarkable feature of Fig. 3.8 is the way in which the characteristics of those cells with relatively thick insulators become concave-upwards as V approaches V_{oc}. For a conventional diffused-junction cell with very large shunt conductance or series resistance, the $J_L(V)$ characteristic may become almost a straight line connecting the short-circuit and open-circuit points, but the characteristic will always be concave downwards [100]. As might be expected, the bias V at which the current first begins to fall sharply in Fig. 3.8 is approximately equal to the difference between V_{oc} and the value of $\Delta\phi$ at equilibrium.

Numerical analysis carried out by Shewchun, Singh and Green [25] has shown that the fill factor of a thick-insulator MIS solar cell may even drop below 0.25, which is the lower limit on this parameter in a conventional homojunction device. The lowest fill factor associated with the characteristics of Fig. 3.8 is indeed slightly less than 0.25.

It should be noted that for the device with the smallest value of J_{VM0} considered in Fig. 3.8, the hole concentration at the semiconductor

surface becomes comparable to N_V for operation near short-circuit. Since the analysis used to generate Fig. 3.8 is valid only when the carrier concentrations in the semiconductor remain at non-degenerate levels (see Section 3.4), the characteristic shown for this device may be in error. However, characteristics obtained using the analysis of Section 3.4 should be at least qualitatively correct provided the semiconductor surface is not strongly degenerate.

CHAPTER 4

POSITIVE BARRIER MIS JUNCTIONS: EXPERIMENT

In this chapter the first conclusive experimental evidence for the existence of minority carrier MIS diodes is presented. This evidence was gathered through two independent experiments which are described in Sections 4.2 and 4.3 respectively. The first of these experiments involved the measurement of the current-voltage characteristics of Al-SiO_x-pSi diodes at various temperatures spanning the range from 0 to 50°C [20]. Since the temperature dependence of an injection-diffusion current is stronger than that of any thermionic emission current, this experiment provided a definitive test for the charge-transport mechanisms dominating the dark current. In the second experiment, Al-SiO_x-pSi solar cells were formed on 10 Ωcm substrates with alloyed aluminum back surface fields [21]. The presence of the back surface field region was found to increase the open-circuit voltage by up to 50 mV relative to the value recorded with an ohmic back contact, a result which can be explained only if the dark current in these cells is dominated by minority carrier injection-diffusion. Section 4.1 provides a brief review of previous experimental research on the positive barrier MIS junction, placing particular emphasis on investigations of a fundamental nature. Finally, the relationship between insulator thickness and electrical characteristics in experimental MIS solar cells is examined in Section 4.4.

4.1 Previous Experimental Research on the MIS Junction

As of mid-1978, when the first of the experiments discussed in this chapter was undertaken, no unambiguous demonstration of the existence of minority carrier MIS diodes had been reported. However, over the

years a considerable body of indirect evidence supporting the MIS tunnel diode theory introduced by Green et al. [16] had appeared in the literature. An overview of this evidence is given below.

In a prophetic experiment conducted in 1963, Jaklevic et al. [101a] demonstrated that an MIS junction could be used to inject sufficient minority carriers into a CdS crystal to generate electroluminescence. In contrast, injection electroluminescence was never observed in Schottky barrier diodes formed on CdS. Since 1963, a number of other groups have observed electroluminescence associated with minority carrier injection from an MIS junction in the semiconductors ZnS, ZnSe, GaP, GaN and GaAs, as well as CdS [101b]. Although the observation of electroluminescence at an MIS contact conclusively reveals the presence of injected minority carriers, it provides virtually no information concerning the relative magnitudes of the majority and minority carrier currents flowing in the contact.

In the early 1970's, Card and Rhoderick [26,102] undertook the first systematic experimental study of the effect of the introduction of a thin interfacial insulating layer on the properties of metal-semiconductor junctions. The structure chosen for this study was the Au-SiO_x-nSi junction, in which the interfacial SiO_x layer was grown by low temperature oxidation of the silicon substrate prior to barrier metal deposition. After correction for variations in the barrier height ϕ_{Bn} with insulator thickness, it was found that the forward-biased dark current decreased by several orders of magnitude as the insulating layer thickness was increased over the range from 8 to 26 Å. Since the dark current in diodes of this type is dominated by thermionic emission, this experiment clearly demonstrated that the introduction of an interfacial insulating layer

could suppress the majority carrier thermionic emission current in a metal-semiconductor junction. However, no attempt was made to measure the magnitude of the injected minority carrier current in these devices.

Card and Rhoderick next turned their attention to the direct measurement of the minority carrier injection ratio γ in MIS junctions [27]. This measurement was accomplished using the metal-emitter transistor structure which Yu and Snow had employed earlier to investigate minority carrier injection in Schottky diodes [13]. The metal-emitter transistor is equivalent to a conventional planar bipolar transistor, except that a Schottky or MIS junction replaces the diffused emitter. Provided that the base width is short compared to the minority carrier diffusion length in the base, the ratio of the collector current to the emitter current in this device is equal to the minority carrier injection ratio of the emitter junction. Card and Rhoderick confirmed Yu and Snow's finding that γ is typically less than 10^{-4} for Au-nSi Schottky diodes formed on chemically etched substrates, and then went on to show that γ could be made as large as 0.2 in Au-SiO_x-nSi diodes with relatively thick ($\simeq$30 Å) interfacial layers. With such thick interfacial layers relatively large forward biases ($\gtrsim$ 1 V) had to be applied to obtain appreciable current flow, so these MIS diodes would not have been of use for photovoltaic energy conversion.

Following the development of their MIS tunnel diode theory, Green et al. themselves carried out a number of fundamental experiments on the MIS structure. In the first of these experiments, Al-SiO_x-pSi diodes with different insulator thicknesses were fabricated on a set of substrates of identical resistivity [68]. The dark current-voltage characteristics of these diodes were found to exhibit the qualitative depend-

ence on insulator thickness predicted theoretically (see Fig. 3.5). In a subsequent experiment, Al-SiO_x-pSi diodes having the same insulator thicknesses were fabricated on substrates with a wide range of resistivities. While a thermionic emission current should be independent of the substrate doping level, the current flowing under moderate forward bias in these MIS diodes was found to decrease as the substrate doping level increased. This is exactly the behaviour which would be expected for a depletion region recombination current or a minority carrier injection-diffusion current. When magnesium was substituted for aluminum as the barrier metal in these diodes, no significant change in the current-voltage characteristics at moderate forward bias was observed, for a given substrate doping. This result strongly suggested that the diode dark current was dominated by minority carrier flows, which depend only on substrate properties. In contrast, the magnitude of a thermionic emission current would have depended strongly on the barrier metal work function.

In other experiments, the small-signal capacitance C of Al-SiO_x-pSi and Mg-SiO_x-pSi diodes was recorded as a function of bias [24,68]. In reverse bias, $1/C^2$ was found to depend linearly on V, just as for a Schottky diode. By finding the voltage-axis intercept of a plot of $1/C^2$ versus V, the diode barrier height was estimated. It was found that in these diodes the silicon surface was strongly inverted at equilibrium, a condition which must be satisfied to produce a minority carrier MIS diode.

Although the experimental results obtained by Green et al. were in general agreement with the predictions of the MIS tunnel diode theory, they did not prove that the majority carrier thermionic emission current

could be made negligible at current densities comparable to the one-sun photocurrent. Most of the devices used in the experiments described above had such thick insulating layers that they entered the tunnel-limited regime long before the dark current density reached the 30 mA/cm^2 level. These devices would thus have been quite unsuitable for use as MIS solar cells. Indeed, in 1976 St. Pierre, Singh, Shewchun and Loferski [103] suggested that significant majority carrier dark current components would always be present in efficient MIS solar cells.

In 1977 Pulfrey reported dark current-voltage characteristics for Al-SiO_x-pSi solar cells showing two regions of exponential dependence of current on bias [104]. At low forward bias the current was found to obey (2.25) with $A \simeq 2$, while for forward biases between 300 and 500 mV (2.25) was obeyed with $A \simeq 1$. Characteristics of this type are frequently observed for silicon homojunction diodes, as discussed in Section 2.2. In interpreting the characteristics of these Al-SiO_x-pSi cells, Pulfrey suggested that at low forward bias the dark current was dominated by recombination in the depletion region, while at larger forward bias the minority carrier injection-diffusion current flowing into the base became dominant. It was thus inferred that these devices were minority carrier MIS diodes. Unfortunately, in an MIS diode current-voltage characteristics of this "double exponential" form can equally well be explained by assuming that the main current component in the higher bias range is a majority carrier thermionic emission current.

Prior to 1978, perhaps the most convincing evidence for the existence of minority carrier MIS diodes resided in the high efficiencies and open-circuit voltages reported by several groups for their MIS solar cells. In 1976, Green, Godfrey and Davies [35] and St. Pierre *et al.* [103]

reported open-circuit voltages over 600 mV for Al-SiO_x-pSi cells fabricated on substrates with resistivities ranging from 0.1 to 1 Ωcm. Anderson *et al.* concentrated on improving the performance of their Cr-SiO_x-pSi cells, and had achieved efficiencies of over 10% and open-circuit voltages of 600 mV by late 1977 [94], using 2 Ωcm substrates. Since a typical diffused junction cell formed on a 1 Ωcm p-type silicon substrate would be expected to have an open-circuit voltage of approximately 600 mV, there could be little doubt that the majority carrier thermionic emission dark current component in these MIS solar cells had been reduced to very low levels.

4.2 New Experimental Evidence for Minority Carrier MIS Diodes

In principle, a minority carrier MIS diode can be identified by the temperature dependence of its dark current-voltage characteristic. Ideally, both majority carrier thermionic emission currents and minority carrier injection-diffusion currents obey the law

$$J = J_0 \, [\exp(qV/kT) - 1] \tag{4.1}$$

where J_0 is a temperature-dependent constant. From (3.30) and (3.38), for a thermionic emission current on a p-type substrate

$$J_{0Th} = \theta_{VM} \, A_h^* \, T^2 \exp(-q\phi_{Bp}/kT) \, , \tag{4.2}$$

while from (2.27), for an injection-diffusion current in a long, uniformly doped p-type base region

$$J_{0d} = q\sqrt{D_n} \, n_i^2 \, / \, (\sqrt{\tau_n} \, N_A) \, . \tag{4.3}$$

The intrinsic carrier concentration n_i is given by [105]

$$n_i(T) = \frac{1}{4}\left[\frac{2kT}{\pi h^2}\right]^{3/2} (m_c^* m_v^*)^{3/4} \exp[-E_g(T)/2kT] \qquad (4.4)$$

where $E_g(T)$ is the bandgap energy of silicon. To a good approximation, $E_g(T)$ decreases linearly with temperature above about 250°K; thus [106]

$$E_g(T) = E_{g0} - \alpha T \qquad (4.5)$$

where E_{g0} and α are temperature-independent constants. There is some disagreement concerning the exact values of E_{g0} and α. In the late 1950's, Macfarlane et al. concluded that $E_{g0} = 1.206$ eV on the basis of optical absorption measurements [106]. More recent measurements of the temperature dependence of the collector current in diffused junction bipolar transistors carried out by Slotboom et al. [107] indicate that $E_{g0} = (1.20 \pm .01)$ eV. The important point is that E_{g0} is significantly larger than the bandgap energy of silicon at room temperature, which is known to lie between 1.11 and 1.12 eV. Substituting (4.5) into (4.4), it is found that

$$n_i^2 \propto T^3 \exp(-E_{g0}/kT) \; . \qquad (4.6)$$

Compared to n_i, D_n and τ_n are not strongly dependent on temperature. Near 300°K the electron mobility μ_n obeys the empirical relationship [108]

$$\mu_n \propto T^{-2.7} \; . \qquad (4.7)$$

Invoking the Einstein relationship between the mobility and the diffusion coefficient, from (4.7) it follows that

$$D_n \propto T^{-1.7} \quad . \tag{4.8}$$

To a first approximation, the minority carrier lifetime is inversely proportional to the mean minority carrier velocity, which is in turn proportional to $T^{1/2}$ [109]. Thus

$$\tau_n \propto T^{-0.5} \quad . \tag{4.9}$$

Combining (4.6), (4.8) and (4.9), it is found that

$$J_{0d} \propto T^{2.4} \exp(-E_{g0}/kT) \quad . \tag{4.10}$$

Comparing (4.2) and (4.10), it is seen that J_{0Th} and J_{0d} are both of the form

$$J_0 \propto T^{\rho} \exp(-E_{g0}/kT) \tag{4.11}$$

where ρ has the value 2 for a thermionic emission current and 2.4 for an injection-diffusion current. Since the temperature dependence of J_0 is dominated by the exponential factor, the exact value of ρ is unimportant.

From (4.11) it can be seen that an Arrhenius plot of $\log(J_0/T^{\rho})$ versus 1/T should yield a straight line, and that the slope of this line should be proportional to an activation energy E_A. For an injection-diffusion current $E_A = E_{g0}$, while for a thermionic emission current $E_A = q\phi_B$.

Because $q\phi_B \leq E_g < E_{g0}$ for any Schottky barrier, this technique can readily distinguish between minority and majority carrier diodes. It should be noted in passing that Yu and Snow have used an activation energy analysis of this type to determine the relative magnitudes of the thermionic emission current and the depletion region recombination current in conventional Schottky barrier diodes [11].

In real diffused junction, MIS and Schottky barrier diodes, it is often found that (4.1) applies, if at all, only over a very limited bias range. At low forward bias the diode characteristics are usually dominated by depletion region recombination currents, which obey (2.25) with A values between 1 and 2. At high forward bias voltage drops across internal series resistances associated with ohmic contacts, with thin barrier metal layers, and with the bulk substrate itself give rise to current-voltage characteristics which do not have an exponential form. Rhoderick has shown that a combination of depletion region recombination current and series resistance effects can produce Schottky diode characteristics in which an exponential current-voltage relationship holds over several decades of current, but in which the diode factor A is significantly greater than unity [89]. When dealing with injection-diffusion currents, deviations from (4.1) will be encountered when the high-level injection regime is reached [110]. In minority carrier MIS diodes, the tunnel resistance effects discussed in Section 4.3 can also lead to deviations from (4.1) [16].

Prior to 1978, both Shewchun and Green [23] and Vernon and Anderson [111] had published data on the temperature dependence of the current-voltage characteristics of MIS diodes. Vernon *et al.* reported current-voltage characteristics for Cr-SiO_x-pSi solar cells at various temper-

atures spanning the range from 20°C to 120°C, but no region in which (4.1) was even approximately obeyed could be discerned in these characteristics. Shewchun et al. recorded current-voltage characteristics for an Al-SiO_x-pSi diode over the temperature range 200-350°C but, again, no region in which (4.1) was obeyed could be found. The diode selected for this latter study had a very thick insulating layer, and showed tunnel limited behaviour at current densities of only 0.1 mA/cm^2. At this low dark current density, depletion region recombination currents would have been far larger than either the injection-diffusion or thermionic emission currents.

In the fall of 1978, the activation energy analysis technique described above was applied to obtain the first irrefutable evidence for the existence of minority carrier MIS diodes with electrical properties suitable for photovoltaic energy conversion [20]. Al-SiO_x-pSi solar cells fabricated on chem-mechanically polished substrates of 10 Ωcm resistivity and <100> orientation were used in this experiment. Complete details of the device fabrication procedure are given in Appendix C. In summary, the substrates were first cleaned following standard procedures used in the manufacture of integrated circuits, and then exposed to a dry oxygen flow at 500°C for 20 minutes to grow a thin oxide layer. An ohmic contact was formed at the back of the slices by the deposition of a thick aluminum layer, followed by sintering in dry nitrogen at 500°C for 10 minutes. The MIS junction itself was produced by depositing a semi-transparent aluminum dot approximately 80 Å thick onto the front surface of the substrates. Contact to this barrier metal layer was made with a single aluminum grid finger several thousand angstroms thick. The thin barrier metal layer and the contact finger were defined using metal shadow masks to give a total

junction area of about 0.1 cm^2. The ohmic contact, barrier metal and contact finger aluminum depositions were all carried out by thermal evaporation from a tungsten filament.

In order to ensure that the silicon surface in the completed Al-SiO_x-pSi cells was strongly inverted at equilibrium, the small-signal capacitance C of these devices was measured as a function of reverse bias. A plot of $1/C^2$ versus V for a typical cell is shown in Fig. 4.1; as expected, the data points lie almost exactly on a straight line. Using the method of least squares, the slope and voltage-axis intercept V_C of this line were computed. The slope is consistent with a doping density of $1.0*10^{15}$ cm^{-3}. Theory predicts that V_C should equal the barrier height ϕ_{Bp} for a junction in which the surface is only depleted at equilibrium. However, if the substrate surface is strongly inverted at equilibrium, V_C should be only slightly greater than the strong inversion potential [24]. The voltage-axis intercept in Fig. 4.2 is 590 mV, while the strong inversion potential for a substrate with a doping density of $1.0*10^{15}$ cm^{-3} is 580 mV. It can thus be concluded that strong inversion of the silicon surface had indeed been achieved.

The dark current-voltage characteristic for a representative Al-SiO_x-pSi cell is shown in Fig. 4.2. Two regions of approximately exponential dependence of current on voltage are visible in this characteristic, as would be expected for a minority carrier MIS diode. However, while in the low-level injection regime an injection-diffusion current must obey (2.25) with A=1, the slope of the upper region of the MIS diode characteristic corresponds to an A value between 1.1 and 1.2. Since no region can be identified in the characteristic over which the diode factor A is equal to unity, it is not possible to derive a reliable estimate

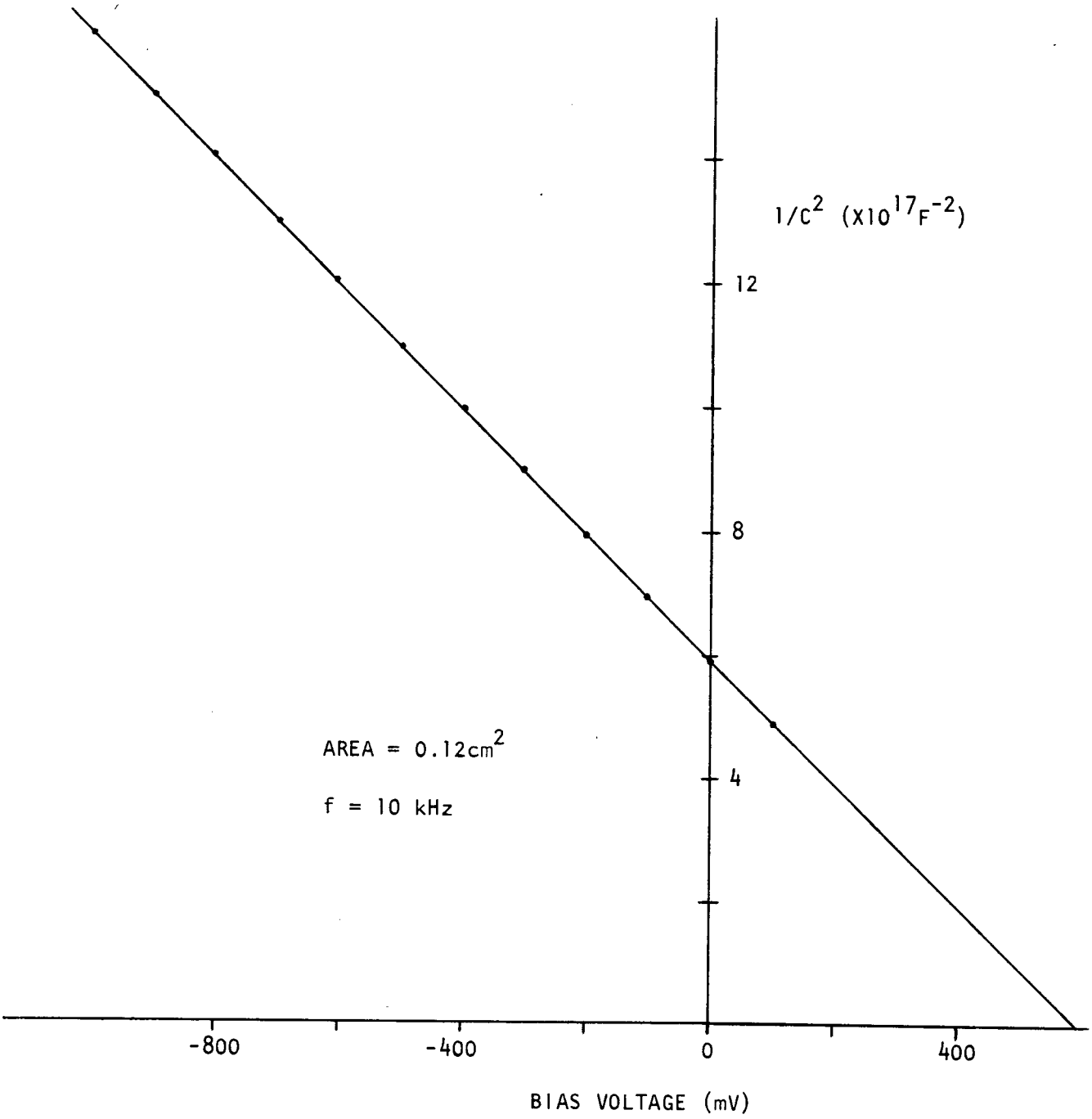

Figure 4.1 Capacitance-voltage characteristic for reverse-biased Al-SiO_x-pSi dot diode.

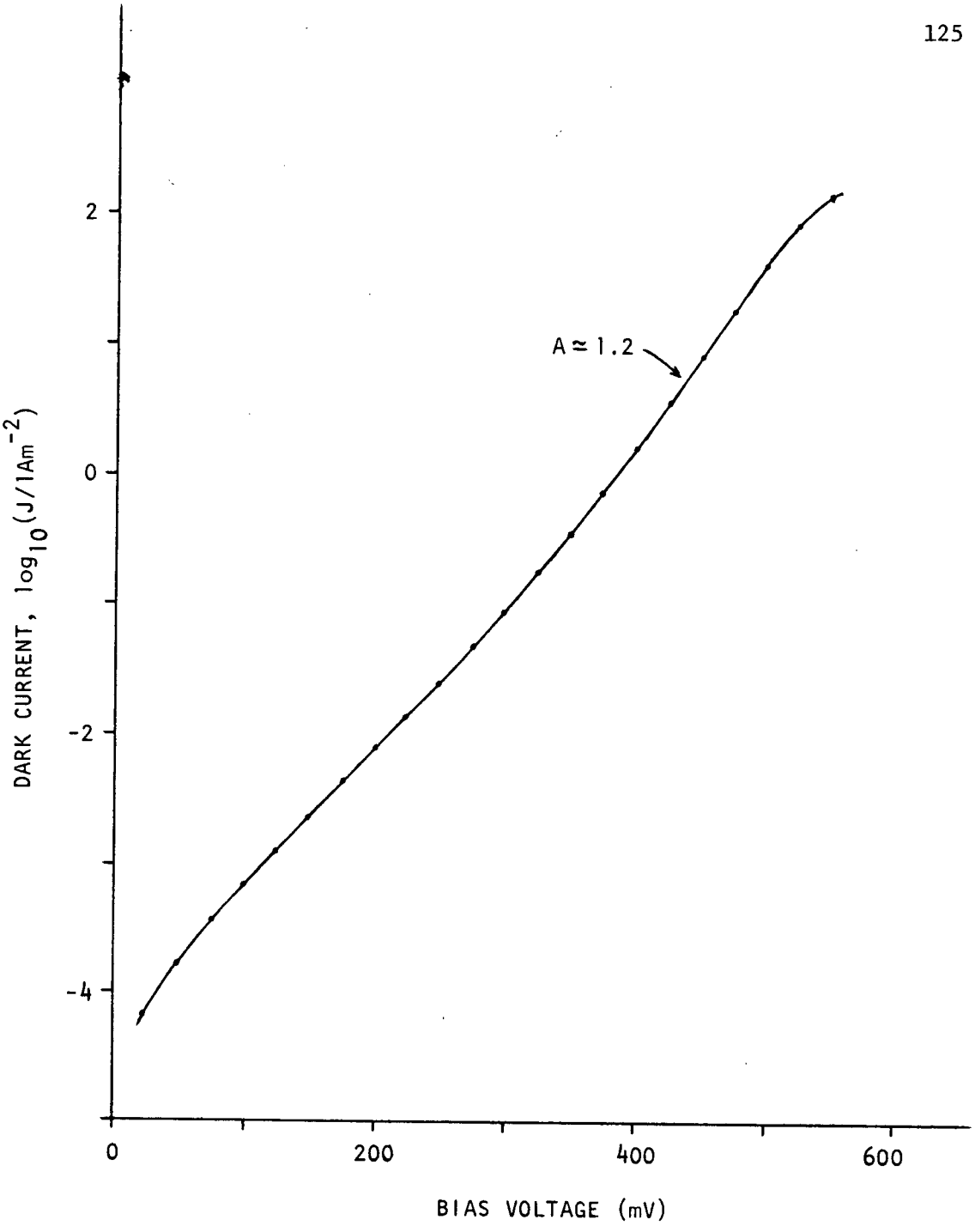

Figure 4.2 Dark current-voltage characteristic for small-area Al-SiO_x-pSi solar cell.

for the parameter J_0 appearing in equation (4.1) from this curve.

As noted above, even in an MIS diode in which the dark current is dominated by minority carrier injection-diffusion, A values greater than unity may be encountered if the bias regime in which the depletion region recombination current is significant is not well separated from the regime in which series resistance or tunnel resistance becomes important. For the device of Fig. 4.2, it appears that a substantial fraction of the dark current flowing at bias levels below about 400 mV resulted from depletion region recombination processes, while series resistance or tunnel resistance effects set in at biases greater than about 500 mV. It should be stressed, however, that the series and/or tunnel resistance was not so large as to seriously degrade the performance of this device when operated as a solar cell. The small-area Al-SiO_x-pSi cells considered here typically gave fill factors ranging from 0.6 to 0.7 under simulated one-sun illumination.

It is well known that ordinary series resistance effects can be eliminated from the current-voltage characteristics of a solar cell by measuring J_{sc} as a function of V_{oc} rather than by measuring J and V in the dark [137]. From the discussion of Section 3.5, it follows also that the effects of tunnel resistance for an MIS cell can be eliminated by recording the J_{sc}-V_{oc} characteristic rather than the dark current-voltage characteristic. For this reason it was decided that it would be worthwhile to obtain J_{sc}-V_{oc} characteristics as well as dark current-voltage characteristics for the MIS cells.

Fig. 4.3 shows the J_{sc}-V_{oc} characteristics for a typical Al-SiO_x-pSi cell recorded at six temperatures spanning the range 0-50°C. These characteristics were taken by mounting the entire test bed, contact probe and

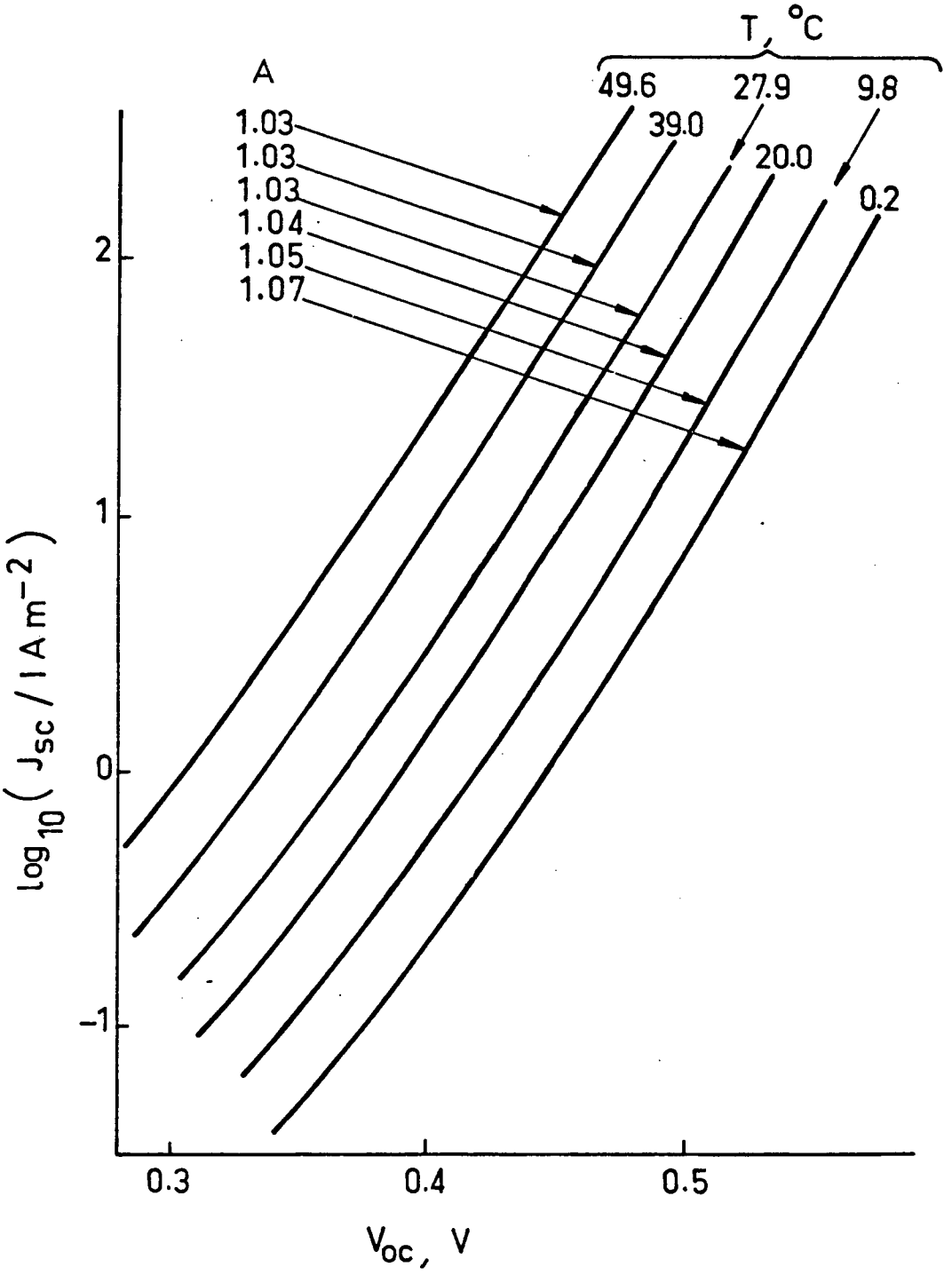

Figure 4.3 J_{sc}-V_{oc} characteristics for a small-area Al-SiO_x-pSi solar cell at various temperatures. The value quoted for A refers to the region $1 \leq J_{sc} \leq 10$ mA/cm^2.

light source assembly within a temperature-controlled Statham oven. The cell temperature was measured using a thermocouple mounted in the test bed. This temperature measurement was confirmed with a mercury thermometer inserted through the oven wall, and should be accurate to about ±0.2°C. In order to minimize any effect that heating by the light source might have had on the characteristics, the light source was switched on only long enough to record a single J_{sc}-V_{oc} pair, and then left off for one to two minutes. The illumination level was also varied randomly from measurement to measurement, rather than being steadily increased.

For short-circuit current densities ranging from roughly 1 to 10 mA/cm^2, the characteristics of Fig. 4.3 are well described by (2.25) with an A value close to unity. At current densities below about 1 mA/cm^2, A becomes significantly larger than unity, while for J_{sc} > 10 mA/cm^2, A actually drops below one, probably as a result of excessive heating of the cell by the light source.

For each characteristic shown in Fig. 4.3, the method of least squares was applied to compute the equation of the line best fitting the data points lying in the range 1 mA/cm^2 ≤ J_{sc} ≤ 10 mA/cm^2. From the slope of this line, the value of A appropriate to this current range was calculated, while an estimate for the parameter J_0 was obtained by finding the intercept of the line with the current axis. This estimate for J_0 will be termed J_{01}. A second estimate for J_0, which will be referred to as J_{02}, was obtained by computing the average of the quantity

$$J_{sc} \exp(-qV_{oc}/kT)$$

over all points in the range specified above. In effect, in the computa-

tion of J_{02} A was assumed to be exactly equal to one. The values of A, J_{01} and J_{02} for each characteristic shown in Fig. 4.3 are listed in Table 4.1. The data presented in Table 4.1 represent the averaging of some 20-25 individual J_{sc}-V_{oc} measurements at each temperature.

After correction for the T^{ρ} factor appearing in (4.11), J_{01} and J_{02} were graphed as a function of reciprocal temperature. These Arrhenius plots are shown in Fig. 4.4. Fig. 4.4(a) reveals that the plot of $\log[J_{02}(300/T)^{2.4}]$ versus reciprocal temperature is fitted almost perfectly by a straight line. Using the method of least squares, the slope of this line was computed, and from the slope the corresponding activation energy E_A was calculated. The value of E_A was found to be (1.19±.013)eV, which agrees almost exactly with the best available estimates for E_{g0}.

From Fig. 4.4(b) it can be seen that not all points in the graph of $\log[J_{01}(300/T)^{2.4}]$ versus reciprocal temperature are co-linear. However, the data points corresponding to the four highest temperatures at which J_{sc}-V_{oc} characteristics were recorded do lie very nearly on a line. Once again, the method of least squares was used to compute the slope of this line, and the appropriate activation energy. In this case E_A was found to be (1.14±.02)eV which, although somewhat less than E_{g0}, is still larger than the silicon bandgap energy at room temperature.

It should be noted that the experimental J_0 data agree very well with an electron lifetime of 10 μsec and a substrate doping of 10^{15} cm^{-3}, which are reasonable estimates for these quantities in 10 Ωcm material. Taking τ_n = 10 μsec, $N_A = 10^{15}$ cm^{-3}, $\mu_n = 0.13$ $m^2V^{-1}s^{-1}$ and $n_i = 1.45*10^{10}$ cm^{-3} at 300°K, (4.3) predicts $J_{0d} = 6*10^{-8}$ mA/cm^2. From Fig. 4.4(a), it can be seen that the experimental value of J_{02} at 300°K is about $5*10^{-8}$ mA/cm^2.

TABLE 4.1 Values of A, J_{01} and J_{02} corresponding to the characteristics of Fig. 4.3

T: (°C)	A:	$\log_{10}[J_{01}(300/T)^{2.4}]$:†	$\log_{10}[J_{02}(300/T)^{2.4}]$:†
-0.2	1.066±.005	-7.708±.047	-8.322±.019
9.8	1.048±.006	-7.145±.058	-7.562±.018
20.0	1.037±.006	-6.511±.048	-6.813±.013
27.9	1.033±.007	-6.033±.056	-6.281±.014
39.0	1.039±.004	-5.304±.028	-5.568±.014
49.6	1.034±.004	-4.726±.025	-4.938±.013

† Here T is measured in °K, J_0 in Am^{-2}

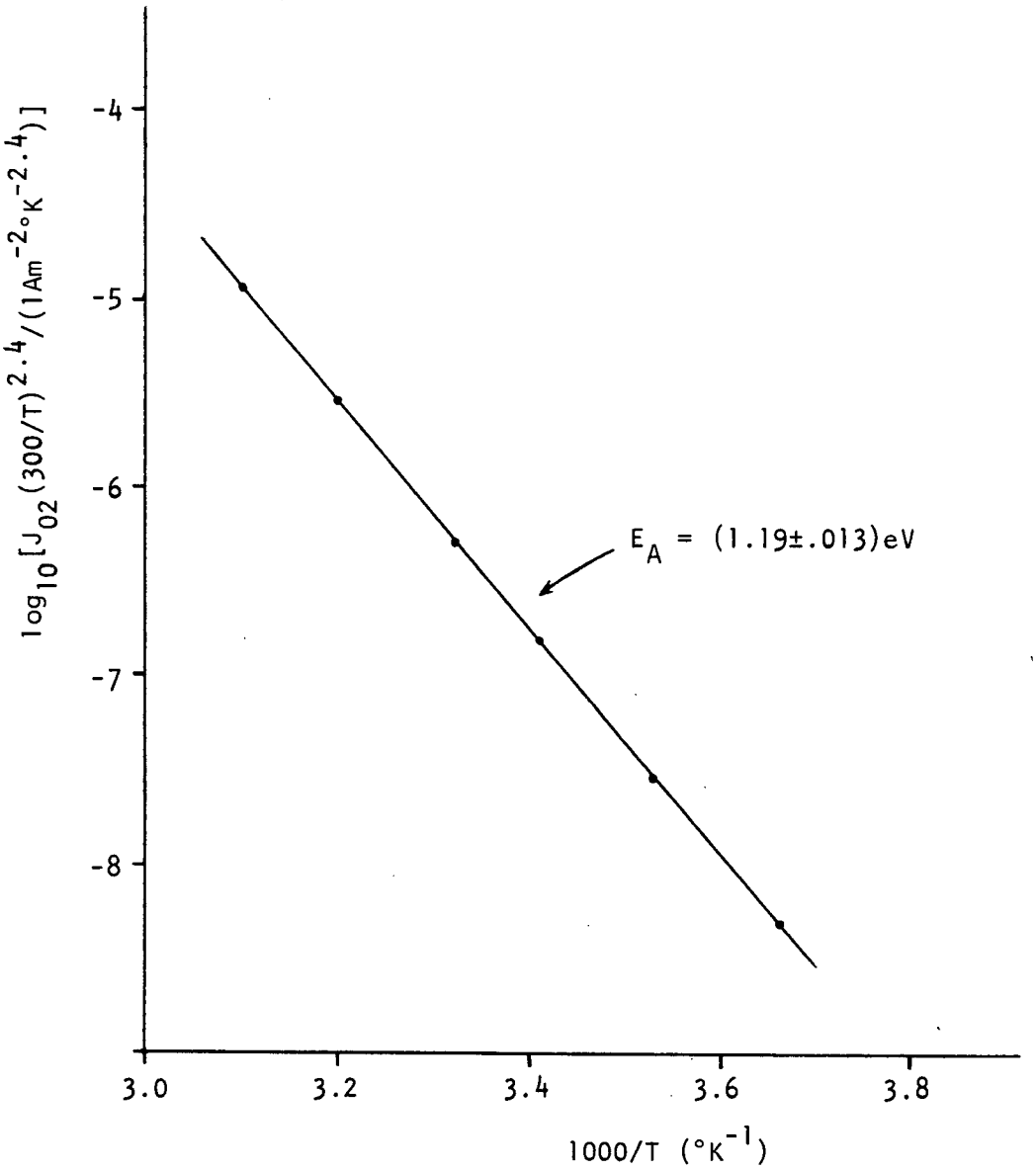

Figure 4.4(a) Temperature dependence of J_{02}.

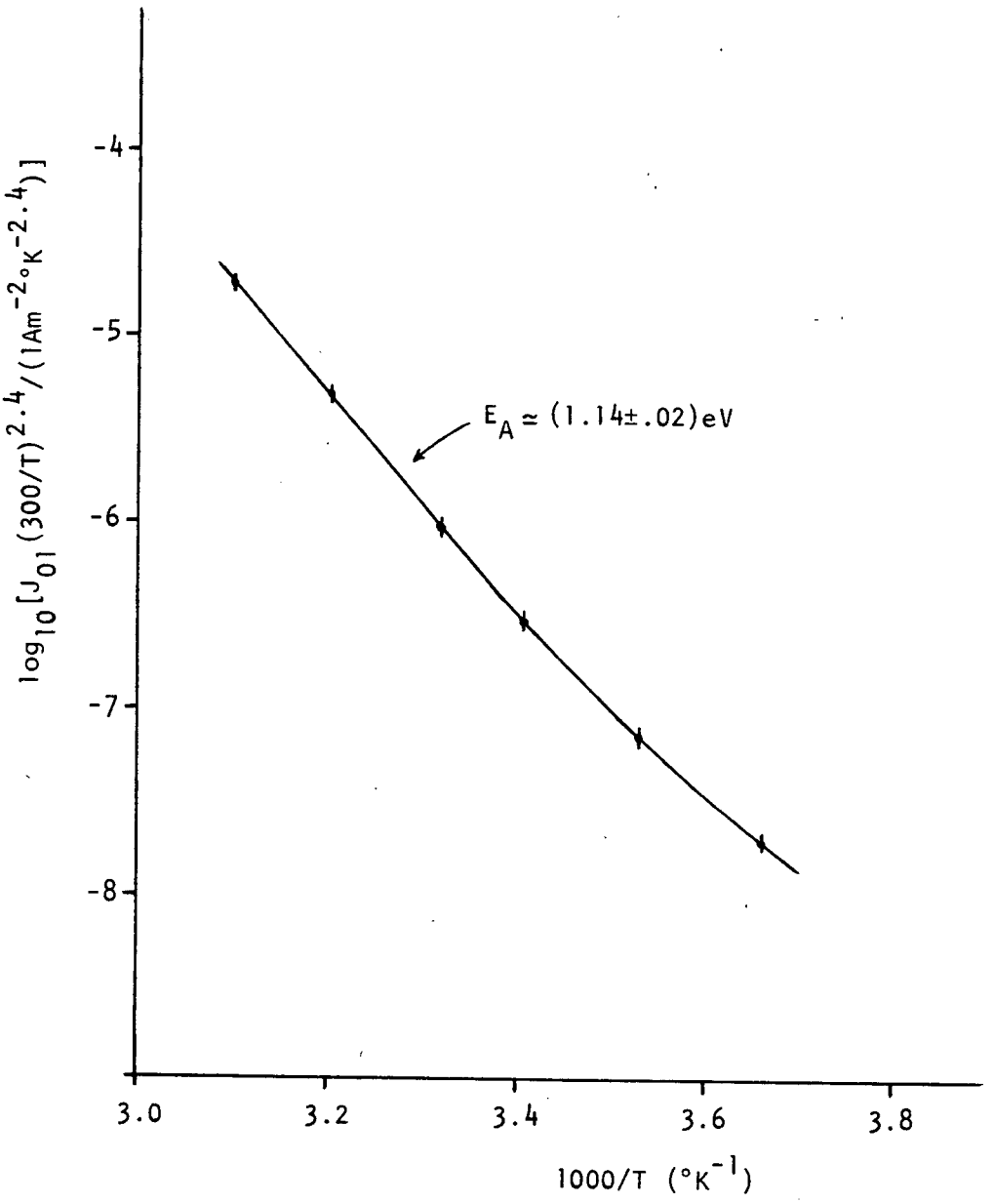

Figure 4.4(b) Temperature dependence of J_{01}.

From the above results it can be concluded that for current densities above about 1 mA/cm^2, the dark current in the Al-SiO_x-pSi diode whose characteristics are shown in Fig. 4.3 is carried almost exclusively by electrons injected from the Al contact diffusing into the quasi-neutral base. This demonstrates that it is possible to form minority carrier MIS diodes on p-type silicon substrates of resistivity greater than or approximately equal to 10 Ωcm. However, this experiment does not guarantee that minMIS devices can be formed on more heavily doped substrates.

4.3 MIS Solar Cells with Back Surface Fields

In the previous section it was shown that Al-SiO_x-pSi solar cells can be produced in which the open-circuit voltage is limited by recombination in the quasi-neutral base. It follows that further increases in the open-circuit voltage of these MIS cells can be achieved only by reducing the magnitude of the electron injection-diffusion dark current flowing into the base. As outlined in Section 2.3, this can be done either by increasing the base doping or, if the electron diffusion length in the base is greater than the base width, by reducing the back surface recombination velocity through the use of a back surface field (BSF). In Section 4.1, the application of the former technique to obtain open-circuit voltages exceeding 600 mV in Al-SiO_x-pSi [35,103] and Cr-SiO_x-pSi [94] cells was mentioned. In this section the first use of a BSF region to enhance the open-circuit voltage of MIS solar cells is described [21]. This experiment provides particularly convincing additional evidence for the existence of minority carrier MIS diodes.

The back surface field substrates used in the experiments described in this section were prepared at Applied Solar Energy Corporation (ASEC) following procedures currently employed in the commercial production of

back surface field space cells [134]. The starting material was boron-doped Czochralski silicon of 9 to 11 Ωcm resistivity and <100> orientation. Measurements carried out at ASEC using the surface photovoltage decay technique have shown that the electron diffusion length in this material is roughly 800 μm. Substrate thicknesses ranged from 350 to 450 μm, while the substrate surfaces were prepared by chemical polishing. The BSF region itself was formed using the aluminum paste alloying technique described in Section 2.3. In order to compare the properties of cells with and without back surface fields, a number of substrates were left without BSF regions.

At the University of British Columbia, Al-SiO_x-pSi front junctions were applied to the ASEC substrates following the process described in Appendix C. The cell geometry is illustrated in Fig. 3.6(a). The semi-transparent barrier metal layer and the thick, comb-like contact grid overlying this layer were both formed by the thermal evaporation of aluminum. The barrier metal layer was typically made 80 Å thick. To minimize cell series resistance, the contact grid should be made as thick as possible. Here limitations on the amount of aluminum which could be deposited in a single pump-down cycle of the evaporation system restricted the grid thickness to roughly 1 μm. The contact grid was defined using a metal shadow mask, giving a finger spacing of roughly 1.2 mm and a grid coverage of approximately 25%. Total device areas ranged from 1.5 to 3 cm^2. No antireflection coating was applied to the cells.

The characteristics of the finished MIS cells were measured under illumination from an ELH lamp, which consists of a tungsten-halogen bulb equipped with a dichroid reflector. Although ELH lamps have a spectral luminosity which is shifted towards near-infrared wavelengths compared

to natural sunlight, these lamps are widely used as crude simulators of AM1 illumination [138].

An uncoated aluminum layer 80 Å thick deposited on a silicon substrate can be expected to transmit only about 30% of incident light at visible wavelengths [93]. As a result, under simulated one-sun illumination the short-circuit current density of the Al-SiO_x-pSi cells was only about 10 mA/cm^2. For purposes of comparison, a modern commercial diffused-junction cell would be expected to give a photocurrent density somewhat greater than 30 mA/cm^2 under one-sun AM1 illumination. Since the electrical rather than the optical properties of the MIS junction were of primary interest here, the light level to which the MIS cells were exposed was therefore increased to give a photocurrent density of 30 mA/cm^2 in each device tested.

The fabrication of Al-SiO_x-pSi solar cells on ASEC BSF substrates was first carried out in early 1979. At that time MIS junctions were applied to pairs of substrates, with each pair consisting of one slice with an alloyed aluminum back surface field and a second slice lacking a BSF region. The thin interfacial oxide layer was grown by exposing the substrates to a dry oxygen flow at 500°C for 20 minutes. A total of six pairs of devices was fabricated. When illuminated to give a photocurrent density of 30 mA/cm^2, the mean open-circuit voltage of the BSF cells was found to be nearly 40 mV higher than that of the cells lacking back surface fields. However, the mean V_{oc} value for the MIS cells with back surface fields was still 15 mV less than that recorded for a control group of four ASEC N^+PP^+ cells fabricated on substrates cut from the same ingot. A more complete description of these results is given in Ref. [21].

By the fall of 1980, improvements in both the process used to produce

MIS junctions at UBC and in the quality of BSF regions formed at ASEC made the fabrication of a second set of Al-SiO_x-pSi solar cells on back surface field substrates worthwhile. For this second fabrication sequence the oxidation temperature was raised to 600°C and the oxidation time extended to 30 minutes. As a result, slightly thicker oxide layers should have grown than were present in the devices made earlier. The open-circuit voltages of the two devices produced in the course of the second fabrication sequence are listed in the first column of Table 4.2. As usual, these open-circuit voltages were measured at a photocurrent density of 30 mA/cm^2 and at a controlled temperature of 28°C. V_{oc} values for a control group of eight ASEC diffused junction space cells fabricated on identical 10 Ωcm substrates were also recorded at this time, under the same test conditions. This control group included six N^+PP^+ back surface field cells and two N^+P cells with ohmic back contacts.

The open-circuit voltages of the two MIS cells compare very favourably with those of the N^+PP^+ control cells, which were found to range from 579 to 598 mV with a mean of 588 mV. In contrast, the open-circuit voltages of the two N^+P cells with ohmic back contacts were found to be 546 and 547 mV.

Despite the use of a 600°C oxidation cycle, the fill factors of the Al-SiO_x-pSi back surface field cells produced in the second fabrication sequence were found to be among the highest for any devices fabricated during the course of this research program. When illuminated to yield a photocurrent density of 30 mA/cm^2, both cells gave fill factors of 0.70.

To demonstrate conclusively that the alloyed aluminum back surface field region was responsible for the high V_{oc} values quoted for the MIS cells, this region was removed and replaced with an ohmic back contact

TABLE 4.2 Open-circuit voltages (mV) for Al-SiO_x-pSi cells, measured at T = 28°C and J_{sc} = 30 mA/cm^2

Cell:	With alloyed aluminum BSF:	With Pd back contact:
#1	594	539
#2	593	543

using only room temperature processing. Extreme care was taken not to damage the front junction during this step. First the front side of each cell was covered with a commercial etch-resistant adhesive tape. The cells were then dipped in 10% HF for a few minutes to remove all traces of the aluminum back contact metallization. Next each cell was immersed in an agitated solution of one part 49% HF to nine parts 70% HNO_3 (so-called "white etch") for a period of one minute, to remove approximately 10 μm of material from the back of the slice. The cells were thoroughly washed, and then re-immersed in dilute HF to ensure removal of all traces of oxide from the back surface. Following a second washing, the tape was peeled away. Finally, a layer of palladium a few hundred angstroms thick was deposited on the back of the slices by flash evaporation from a tungsten filament to form a new rear contact. The substrates were only exposed to the hot filament for a few seconds during this evaporation, so heating of the cells should have been minimal. Palladium contacts to p-type silicon formed in this way have been found to give ohmic characteristics out to current densities of more than 100 mA/cm^2, with resistances of less than 0.1 Ωcm^2. (In a subsiduary experiment, the current-voltage characteristics of palladium contacts to freshly-etched p-type silicon were measured by applying such contacts to the front surface of 2 Ωcm slices with sintered aluminum back contacts).

The open-circuit voltages recorded for the two MIS cells following removal of the back surface field region are listed in the second column of Table 4.2. For both cells, the V_{oc} value measured after reprocessing is seen to be at least 50 mV less than that recorded when the back surface field region was intact. As expected, the open-circuit voltages for the reprocessed cells are very close to those of the N^+P control cells

with ohmic back contacts. The fact that a modification to the back surface of these MIS cells could reduce their open-circuit voltages by a full 50 mV demonstrates conclusively that the dark current in these devices is dominated by minority carrier injection-diffusion.

To ensure that the reduction in open-circuit voltage brought about on replacement of the back surface field region did not result from damage to the MIS front junction, two Al-SiO_x-pSi control cells were carried through the back contact refabrication procedure outlined above along with each MIS back surface field cell. These control cells had been fabricated on 2 Ωcm substrates with ohmic back contacts, and originally gave open-circuit voltages ranging from 558 to 572 mV. In no case did the open-circuit voltage of any control cell drop by more than 2 mV on replacement of the back contact. It can thus be concluded that the processes of taping, etching, tape removal and palladium deposition described above do not significantly alter the properties of an MIS front junction.

As pointed out in Section 2.3, a back surface field region should provide a small increase in photocurrent response at long wavelengths. To check for the presence of this effect, the short-circuit photocurrent of one of the MIS back surface field cells was recorded under infrared illumination. (A source rich in infrared was obtained by simply operating an unfiltered tungsten-halogen lamp at one-third its rated voltage; the light intensity was monitored and held constant to within ±1% using a reference silicon photodiode). With the back surface field region intact, the infrared photocurrent for this cell was found to be 2.22 mA. Following replacement of the back surface field with a palladium ohmic contact, the photocurrent under the same illumination conditions dropped to 1.75 mA.

4.4 Variation of MIS Solar Cell Characteristics with Insulator Thickness

In Section 3.5, it was predicted that MIS solar cells with thick insulating layers would have illuminated current-voltage characteristics which were concave-upwards over a certain bias range, as illustrated in Fig. 3.8. Further, it was noted that the numerical analysis carried out by Shewchun et al. [25] predicts fill factors less than 0.25 for MIS cells with very thick insulators. In contrast, conventional homojunction cells always have illuminated current-voltage characteristics which are everywhere concave downwards, and thus must have fill factors greater than 0.25. Although MIS cells with insulators thick enough to cause photocurrent suppression are clearly of little use for photovoltaic energy conversion, the observation of an illuminated current-voltage characteristic resembling Fig. 3.8 in an experimental cell would help confirm the validity of the semiclassical model of the MIS junction.

In order to produce MIS cells with thick insulators, a group of Al-SiO_x-pSi devices were fabricated in accordance with the procedure outlined in Section 4.1 and in Appendix C, with the exception that oxidation temperatures ranging from 600°C to 660°C were used. The oxidation time was held constant at 30 minutes. The substrates selected for this experiment were of 2 Ωcm resistivity and <100> orientation, and had chem-mechanically polished front surfaces. Following oxidation, a thick layer of aluminum was deposited on the back of the wafers to form an ohmic contact. The contact was then sintered at a temperature of 500°C for 30 minutes in a nitrogen atmosphere. Finally, the semi-transparent barrier layer and thick contact grid were deposited, giving a total junction area of 2 cm^2 and a grid coverage of about 25%.

The illuminated current-voltage characteristics of the completed

Al-SiO_x-pSi cells are shown in Fig. 4.5. As usual, these characteristics were recorded at a temperature of 28°C under illumination sufficient to give a photocurrent density of 30 mA/cm^2. The characteristics of those cells fabricated using oxidation temperatures of 650°C or greater are seen to be concave upwards over all or part of the power-output quadrant, as predicted in Section 3.5. Further, the device oxidized at 660°C has a fill factor of less than 0.25, as predicted by Shewchun et al. MIS cells with fill factors less than 0.25 have also been fabricated by Card [79] and by St. Pierre et al. [103].

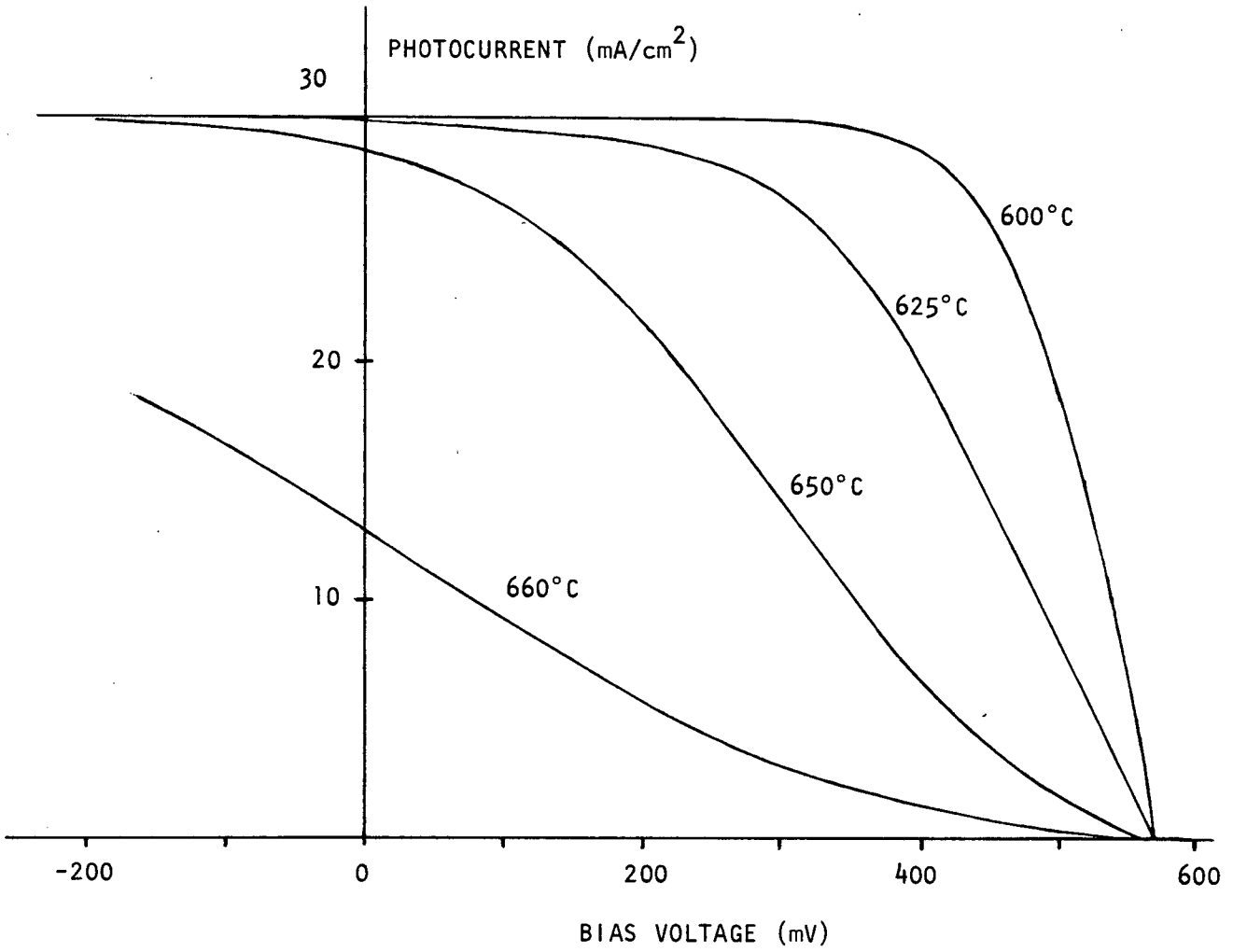

Figure 4.5 Illuminated current-voltage characteristics for Al-SiO_x-pSi solar cells with various insulator thicknesses, as measured experimentally. Oxidation temperature is specified for each characteristic. J_{upc}=30mA/cm^2, T=28°C.

CHAPTER 5

MINORITY CARRIER REFLECTING NEGATIVE BARRIER MIS CONTACTS

According to the definition given in Chapter 1, in a negative barrier Schottky or MIS junction the semiconductor surface is accumulated at equilibrium. Junctions of this kind can be formed by depositing a low work function metal on an n-type substrate, or a high work function metal on a p-type substrate, provided that the surface state density has been reduced to negligible levels. In practice, strong accumulation can only be achieved in MIS junctions, where the growth of the thin interfacial layer passivates the semiconductor surface (see Section 3.1).

It has long been known that it should be possible to use negative barrier Schottky junctions to form low resistance metal-semiconductor contacts [34]. However, it is only recently, and only through the use of the MIS tunnel junction technology, that low resistance negative barrier contacts to silicon have been successfully fabricated [112].

In 1976 Green, Godfrey and Davies recognized that with a correct selection of barrier metal and insulator thickness, it should be possible to form negative barrier MIS contacts which would not only offer negligible impedance to the flow of majority carriers, but which would reflect minority carriers in the same manner as a metallurgical high-low junction [35]. A negative barrier junction of this type could thus be used as a rear contact in an induced back surface field solar cell. Although Green et al did succeed in fabricating low resistance negative barrier MIS contacts to both n- and p-type silicon, they were unable to produce contacts with demonstrable minority carrier reflecting properties [36].

In the first section of this chapter, an approximate analytic model of current flow in the negative barrier MIS contact is developed by a

simple extension of the results obtained in Chapter 3 [37]. (The only other theoretical study of minority carrier reflection at the negative barrier MIS junction so far reported [35] was undertaken by Green et al. using numerical analysis. The results of this investigation have never been published.) The remainder of the chapter is devoted to the experimental demonstration of the minority carrier reflecting properties of the negative barrier junction. In Section 5.2, the use of negative barrier Mg-SiO_x-nSi contacts to form induced back surface field regions for P^+N cells with diffused front junctions is discussed [37]. Section 5.3 then considers the formation of minority carrier reflecting MIS contacts on p-type substrates using platinum as the barrier metal. Induced back surface field action was obtained by applying Pt-SiO_x-pSi back contacts to both N^+P diffused front junction cells, and to cells with Al-SiO_x-pSi minMIS front junctions. Although the yield of good devices in all the experiments mentioned above was never high, the open-circuit voltages of the best induced back surface field cells were in every case comparable to those obtained with conventional diffused or alloyed back surface fields.

5.1 Current Flow in the Negative Barrier MIS Junction: Theory

For notational convenience, it will be assumed that the negative barrier MIS junctions considered in this section have been formed on p-type substrates. However, the conclusions drawn here apply equally well to n-type material if the roles of electrons and holes are interchanged.

The band diagram for a negative barrier MIS contact formed on a p-type substrate is shown in Fig. 5.1(a). This band diagram represents a non-equilibrium situation in which excess electrons have been introduced into the semiconductor either through illumination or by injection from

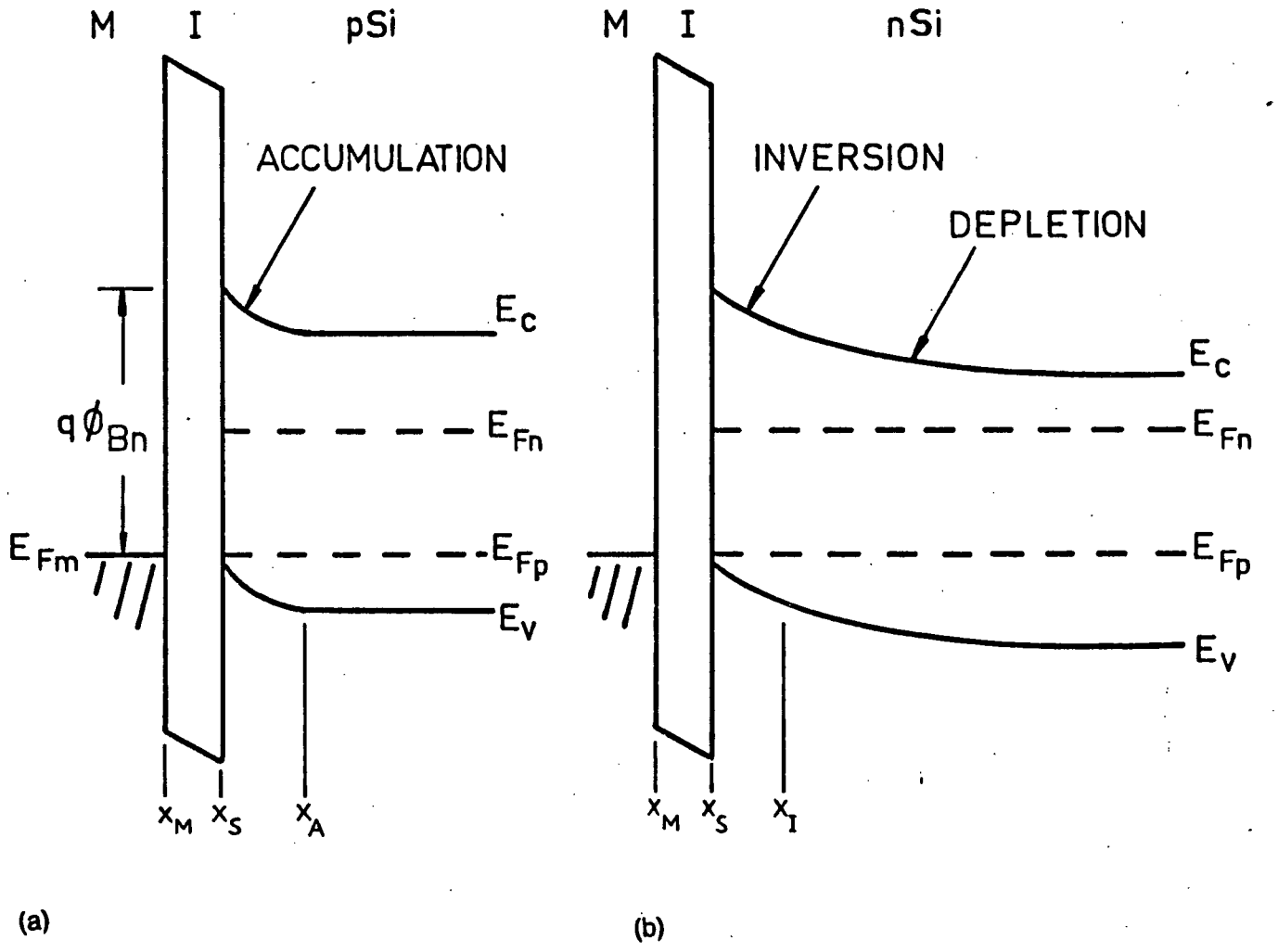

Figure 5.1 Band diagrams for (a) a negative barrier MIS junction, and (b) the corresponding positive barrier MIS junction formed by depositing the same metal on a substrate of the opposite doping type. Note the similarity between the semiconductor surface regions of the two structures. Both diagrams represent non-equilibrium situations.

a P^+N junction to the right. Fig. 5.1(a) is in many respects similar to the band diagram for the corresponding positive barrier junction formed by depositing the same metal on a substrate of the opposite doping type, which is shown in Fig. 5.1(b). This observation is the key to the analysis of current flow in the negative barrier junction. In particular, the band structure of the accumulation layer - insulator - metal region in Fig. 5.1(a) is nearly identical to that of the inversion layer - insulator - metal region in Fig. 5.1(b). Differences between the two band structures can result only from the storage of charge in the depletion region of the positive barrier junction. Provided the semiconductor surface is strongly inverted in one case and strongly accumulated in the other, these differences should be small.

If a negative barrier MIS junction is to provide essentially no impedance to the flow of majority carriers between the metal and the semiconductor, then the interfacial insulator must be sufficiently thin that the majority carrier quasi-fermi level at the semiconductor surface is effectively pinned to the fermi level in the metal under normal operating conditions. Further, since the hole concentration in the accumulation layer is extremely large, and since this region can be no more than a few hundred angstroms thick, E_{Fp} must be very nearly constant across the accumulation layer. It follows that over the normal operating range both the hole distribution and the electrostatic potential distribution in the junction region must remain "frozen" in their equilibrium forms. The energy difference between the conduction band edge at the semiconductor surface and the fermi level in the metal must therefore be fixed at its equilibrium value, which, as in the case of the positive barrier junction, will be denoted as $q\phi_{Bn}$.

In drawing Fig. 5.1(a), it has been assumed that the electron quasi-fermi level is constant across the accumulation layer. As usual, after computing the minority carrier flow through the junction, the accuracy of this assumption can be checked using the methods of Section 2.2. From the results of Chapter 3, the net electron current flowing between the conduction band and the metal is given by

$$J_{CM} = \theta_{CM} A_e^* T^2 \exp[-(E_C(x_S) - E_{Fn}(x_S))/kT] \cdot(1 - \exp[-(E_{Fn}(x_S) - E_{FM})/kT]) \quad (5.1)$$

For the situations of interest here, $E_{Fn}(x_S)$ lies above E_{FM} by many multiples of kT, allowing the rightmost exponential term in (5.1) to be set equal to zero. Therefore

$$J_{CM} = \theta_{CM} A_e^* T^2 \exp(-q\phi_{Bn}/kT) \exp(q\Delta\phi/kT) \quad (5.2)$$

where $q\Delta\phi$ is now defined to be the separation between E_{Fn} and E_{Fp} in the junction region ($\Delta\phi$ will be taken as positive when E_{Fn} lies above E_{Fp}). Since the electron concentration $n_p(x_A)$ at the edge of the accumulation region is related to the thermal equilibrium electron concentration n_{p0} in the quasi-neutral base by

$$n_p(x_A) = n_{p0} \exp(q\Delta\phi/kT) , \quad (5.3)$$

(5.2) becomes

$$J_{CM} = \left[\frac{\theta_{CM} A_e^* T^2 \exp(-q\phi_{Bn}/kT)}{n_{p0}} \right] n_p(x_A) \quad . \tag{5.4}$$

(5.4) can be written as

$$J_{CM} = q\, S_{eff}\, n_p(x_A) \tag{5.5a}$$

where

$$S_{eff} = \frac{\theta_{CM} A_e^* T^2 \exp(-q\phi_{Bn}/kT)}{q\, n_{p0}} \quad . \tag{5.5b}$$

Thus so far as minority carrier flows are concerned, the negative barrier MIS contact can be described by an effective surface recombination velocity S_{eff}. More specifically, the distribution of minority carriers in the quasi-neutral base would be unchanged if the negative barrier contact were replaced by a surface with recombination velocity S_{eff} positioned at the edge of the accumulation layer. The quantity S_{eff} defined in (5.5b) is thus completely analogous to the effective surface recombination velocity used to describe the current flow in solar cells with diffused back surface fields (see Section 2.3).

From (5.5) it can be seen that the effective surface recombination velocity at a negative barrier contact can be reduced by selecting the barrier metal work function to maximize ϕ_{Bn}, or by increasing the oxide thickness in order to reduce the tunnelling probability factor θ_{CM}. However, if the oxide is made too thick the impedance of the contact to majority carrier flow may become excessive. If the negative barrier junction is to be used to form an induced back surface field solar cell,

a majority carrier current equal in magnitude to the one-sun photocurrent must be able to pass between the metal and the semiconductor without significant displacement of $E_{Fp}(x_s)$ from E_{FM}.

In deriving (5.5), no allowance was made for the recombination of electrons with holes through the process of carrier trapping by surface states. In general, if such processes are possible the electron current flowing into the junction region will be greater than that specified by (5.5). Thus (5.5b) gives a lower bound on the effective surface recombination velocity of a negative barrier MIS contact.

A particularly simple relationship exists between the effective surface recombination velocity S_{eff} for a negative barrier MIS contact defined above and the value of J_{0Th} associated with the electron thermionic emission current in the corresponding positive barrier junction. From (5.5b) and (4.2),

$$S_{eff} = J_{0Th}/n_{p0} \cdot \tag{5.6}$$

(5.6) emphasizes that the problem of minimizing the effective surface recombination velocity in a negative barrier MIS contact is equivalent to the problem of minimizing the majority carrier thermionic emission current in the corresponding positive barrier junction. In the case of the positive barrier device, increasing the insulator thickness reduces the majority carrier current, but also lowers the maximum minority carrier current which can be injected before the tunnel limited regime is entered. Similarly, in the negative barrier contact an increase in the insulator thickness lowers S_{eff} while simultaneously reducing the maximum majority carrier current which can be passed through the contact before

tunnel resistance effects become appreciable.

5.2 Induced Back Surface Field Solar Cells on n-Silicon Substrates

When the experiments on negative barrier MIS junctions described in this chapter were begun in the fall of 1979, a substantial body of evidence had been published indicating that minority carrier MIS diodes could be formed by depositing aluminum or magnesium on p-type silicon substrates [20,21,19]. In contrast, in only one instance had an open-circuit voltage exceeding 450 mV been reported for an MIS solar cell formed on n-type silicon [19]. The low open-circuit voltages obtained for these MIS cells suggested that it would be difficult, if not impossible, to form a minority carrier MIS diode on n-type silicon. For this reason it was decided that the first attempt to fabricate a minority carrier reflecting negative barrier MIS contact should be made using an n-type substrate. Furthermore, it was decided that the most convincing evidence for the minority carrier reflecting properties of the negative barrier junction could be obtained by employing this structure as the back contact in an induced back surface field solar cell.

To determine if a negative barrier MIS back contact could enhance solar cell open-circuit voltage in the same manner as a diffused back surface field, a group of 2cm X 2cm P^+NN^+ BSF cells fabricated on 10 Ωcm substrates of <100> orientation were obtained from Applied Solar Energy Corporation. These cells had been prepared in accordance with current industrial procedures. Four of the cells from this group were retained for use as controls. The front surfaces of the remaining seven cells were then protected with tape, after which the diffused N^+ back surface field region was etched away. Any traces of native oxide left on the back

surface after this etching process were removed by immersing the slices in 10% HF for one minute. The slices were then washed thoroughly, and the protective tape was peeled away. The samples were next oxidized in dry oxygen at 500°C for 20 minutes. Following oxidation, a thick layer of magnesium was deposited on the back of the slices by thermal evaporation to form the negative barrier MIS junction. Since magnesium oxidizes rapidly on exposure to the atmosphere, this magnesium layer was immediately overlaid with a protective coating of thermally evaporated aluminum. The structure of the completed cells is illustrated in Fig. 5.2.

The current-voltage characteristics of the completed MIS back contact cells were measured under simulated one-sun AM1 illumination at a controlled temperature of 28°C. As usual, a filtered tungsten-halogen bulb was used as the AM1 simulator. The short-circuit current density was found to be 34 mA/cm^2 in all cells tested. Open-circuit voltages were found to range from 565 to 583 mV. The V_{oc} values for the four best devices are listed in the first column of Table 5.1. Under identical operating conditions, the open-circuit voltages for the P^+NN^+ control cells ranged from 574 to 583 mV. It follows that the negative barrier MIS contact is capable of producing an effective surface recombination velocity for minority carriers which is as low as can be achieved using a conventional diffused back surface field. However, it is also apparent that some of the MIS contacts had relatively high effective surface recombination velocities. This inconsistent performance of the negative barrier contact has been tentatively attributed to variations in the roughness and degree of contamination of the etched back surfaces.

It is expected that a higher yield of minority carrier reflecting MIS contacts would be obtained if more attention were paid to achieving

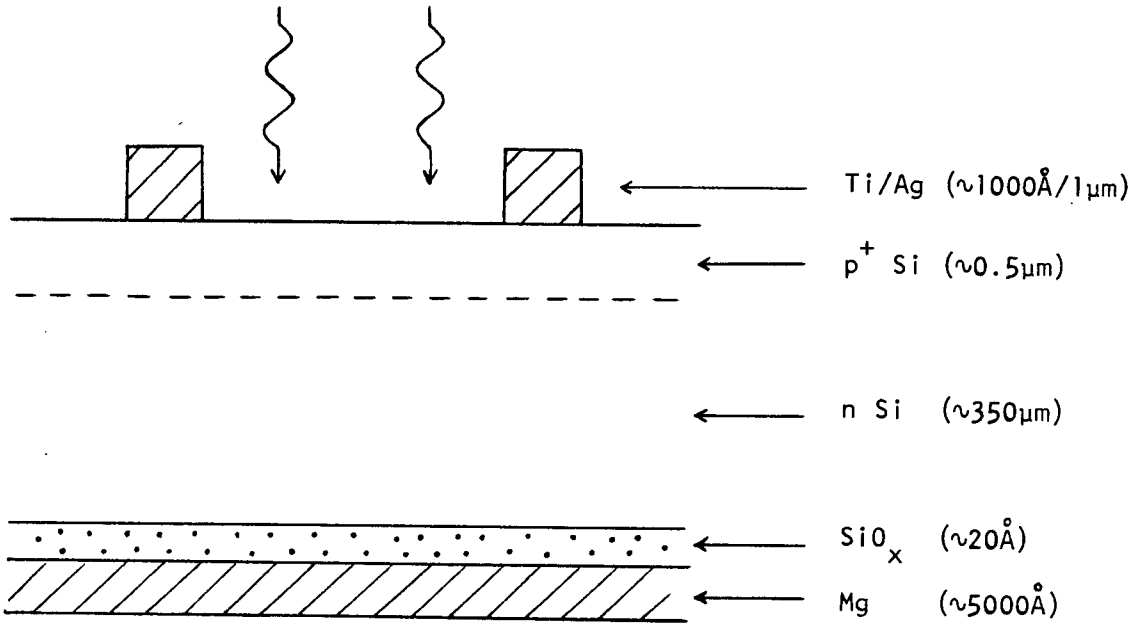

Figure 5.2 Structure of P^+N cell with negative barrier Mg-SiO_x-nSi back contact.

TABLE 5.1 Open-circuit voltages (mV) for selected P^+N cells with negative barrier MIS back contacts

Cell:	1st fabrication:[a]	2nd fabrication:[b]	3rd fabrication:[a]
P^+NIM#1	582	547	585
P^+NIM#2	583	549	577
P^+NIM#3	581	545	-
P^+NIM#4	570	546	-

[a] Oxidation/anneal at 500 °C in O_2 for 20 mins; Mg barrier

[b] Anneal at 450 °C in N_2 for 5 mins; Al barrier

a high surface finish in the etching process, and if the slices were subjected to the full cleaning procedure specified in Appendix C prior to fabrication of the back junction. (The tape used here to protect the front contact metallization could not withstand this full cleaning procedure, so the slices were simply dipped in 10% HF prior to oxidation). It is, of course, possible to form negative barrier back contacts on P^+N cells which have never undergone a back surface field diffusion. However, it is unlikely that cells formed in this way would give open-circuit voltages significantly greater than those of P^+N cells with ohmic back contacts. In general, the hole diffusion lengths in as-grown n-type material are too short for a back surface field to be of use in enhancing the open-circuit voltage of a standard 300 μm thick solar cell fabricated on such material. The high open-circuit voltages recorded for P^+NN^+ cells are thought to be made possible by the gettering action of the phosphorus diffusion used to form the N^+ back surface field region [135]. This gettering action is believed to raise the hole diffusion length to a point where the minority carrier reflecting properties of the back surface field can assist in reducing the hole injection-diffusion dark current component.

In order to ensure that the N^+ BSF diffusion had been completely removed from the substrates used in the experiments described above, the MIS back contact metallization and thin oxide were stripped from all seven devices. This was accomplished by applying protective tape to the front side of the cells, and then immersing the substrates in 10% HF for a few minutes. Following washing and tape removal, the slices were exposed to a dry nitrogen flow at 450°C for five minutes. New MIS back contacts were then formed by the deposition of thermally evaporated

aluminum. When applied to p-type substrates, this fabrication procedure has been found to yield Al-SiO_x-pSi solar cells with very low open-circuit voltages, demonstrating the presence of a large majority carrier thermionic emission dark current component. The process would therefore be expected to give high effective surface recombination velocities when used to form negative barrier contacts on n-type material.

The open-circuit voltages of the reprocessed cells ranged from 544 to 549 mV (see the second column of Table 5.1). For purposes of comparison, experiments conducted at Applied Solar Energy Corporation have shown that V_{oc} values between 545 and 550 mV are obtained when the N^+ layers are removed from P^+NN^+ cells and replaced with conventional sintered ohmic contacts. This confirms that the high V_{oc}'s recorded for the best MIS back contact devices in the first stage of the experiment did not result from the presence of residual traces of the original N^+ back surface field diffusion.

To provide final confirmation of the experimental results and to check that the low V_{oc}'s recorded after the second MIS back contact fabrication were not caused by spurious effects such as the degradation of the front contact or the junction during reprocessing, the MIS back contact metallization and oxide were stripped from the two best cells yet again. These cells were then reprocessed following the procedure used in the first stage of the experiment (that is, the substrates were oxidized for 20 minutes at 500°C, and magnesium was used for the barrier metal). The V_{oc} values obtained after this third fabrication sequence are listed in the third column of Table 5.1, and it can be seen that they agree closely with those recorded after the first MIS contact fabrication (column 1).

As noted in Section 5.1, in order for a negative barrier MIS junction to be of use in forming a practical induced back surface field solar cell, it is essential that the resistance of the junction to majority carrier flow be no greater than that of a conventional sintered contact. As yet, no formal experiments have been carried out here to determine the effective resistance of the Mg-SiO_x-nSi and Al-SiO_x-nSi negative barrier junctions. However, measurements of the fill factors of the induced back surface field solar cells described above indicate that this effective contact resistance is not excessive. The fill factors of these devices were found to lie in the range 0.6 - 0.65, except in those cases in which part of the front contact metallization was damaged during processing. Further experimentation will be required to determine if the series resistance associated with the negative barrier MIS contact can be made less than or equal to that of a diffused back surface field with a sintered contact.

5.3 Induced Back Surface Field Solar Cells on p-Silicon Substrates

Following the successful production of minority carrier reflecting negative barrier MIS contacts to n-type substrates, attention was turned to fabricating similar contacts to p-type material. Before this could be done, it was first necessary to develop a technique for forming minority carrier MIS diodes on n-type silicon. As noted in the previous section, the low open-circuit voltages reported by other investigators for MIS solar cells fabricated on n-type silicon [19] suggested that there would be little chance of success in this task.

In Chapter 3 it was pointed out that the chances of forming a minority carrier MIS diode on n-type material are greatest when using a barrier

metal with the highest possible work function. From the values of vacuum work function for the elements tabulated by Sze [113], it can be seen that the metals platinum, irridium, rhenium and palladium have the highest work functions. Of these metals, palladium and platinum are the most readily available, and the easiest to obtain in a form suitable for thermal evaporation.

5.3.1 minMIS Diodes on n-Silicon Substrates

In the first stage of the experiments described in this section, small-area MIS solar cells were fabricated on n-type silicon substrates using either palladium or platinum for the barrier metal. The substrates used were of <100> orientation and 5 Ωcm resistivity. The front surfaces of these wafers had been prepared by the standard industrial technique of chem-mechanical polishing. Following cleaning in accordance with the procedure specified in Appendix C, the wafers were exposed to a dry oxygen flow for 20 minutes. At first, oxidation was carried out at 500°C, but in later experiments oxidation temperatures as high as 650°C were investigated. The substrates were not removed from the furnace immediately after oxidation, but were instead exposed to a dry nitrogen flow for an additional 20 minutes. This last step may help reduce Q_{FC}, the fixed positive charge associated with the Si-SiO_x interface [114], and thus allow the attainment of higher barrier heights [136]. Following the oxidation/annealing sequence, a thick layer of thermally evaporated aluminum was deposited on the backs of the wafers to form a negative barrier MIS back contact. (The minority carrier reflecting properties of this Al-SiO_x-nSi contact were not of interest here; the negative barrier MIS technology simply offered a convenient technique for forming a low-resist-

ance back contact to the lightly-doped n-type substrates). The rectifying MIS front junction was then formed by the deposition of a semi-transparent layer of thermally evaporated palladium or platinum. The procedures followed in the evaporation of these metals are discussed in Appendix C. The barrier metal layer was made approximately 100 Å thick, and was delineated using a metal shadow mask to give a total device area of about 0.1 cm^2. Finally, a small contact dot composed of the same metal used in the barrier layer was deposited near the edge of each cell.

In 5 Ωcm n-type silicon, reasonable estimates for the hole lifetime and mobility are 0.3 μs and 0.05 $m^2V^{-1}s^{-1}$ respectively (see Appendix A). Substituting these estimates for τ_p and μ_p into (2.28), it is found that a minority carrier MIS solar cell formed on such a substrate should give an open-circuit voltage of about 490 mV at a photocurrent density of 30 mA/cm^2 and a temperature of 28°C.

The completed palladium-barrier cells were found to have characteristics similar to those expected for Schottky diodes fabricated using conventional techniques. When illuminated to give a photocurrent density of 30 mA/cm^2, these cells yielded an open-circuit voltage of approximately 250 mV at a temperature of 28°C. This low open-circuit voltage indicates that the dark current in these devices is dominated by majority carrier thermionic emission. The reason for the poor performance of these cells was discovered later when the palladium layer was removed by etching in aqua regia (a mixture of 3 parts hydrochloric acid to 1 part nitric acid). Although the aqua regia rapidly dissolved all traces of metallic palladium, even after prolonged exposure to the acid at elevated temperatures a pinkish residue remained on the silicon surface where the cells had been. It thus appears that the condensing palladium actually penetrated

the thin oxide layer at the substrate surface and reacted with the underlying silicon to form palladium silicide. Rather than producing an MIS junction, this process results in the formation of an intimate-contact Pd_2Si-Si Schottky barrier. Although every effort was made to minimize heating of the substrates during the evaporation, palladium silicides are known to form at temperatures as low as 250°C [115].

In contrast to the results obtained with palladium, the platinum-barrier cells gave open-circuit voltages ranging from 490 to 510 mV at a photocurrent density of 30 mA/cm^2 and a temperature of 28°C. These V_{oc} values are the second highest ever reported for MIS cells fabricated on n-type silicon [19], and agree quite well with the crude estimate made above for the open-circuit voltage of a minMIS cell formed on a 5 Ωcm n-type substrate. Further, when the platinum layer was removed in aqua regia, no insoluble residue was visible at the silicon surface. It was therefore tentatively concluded that the platinum cells were true MIS devices, with the structure Pt-SiO_x-nSi.

To determine if strong inversion of the semiconductor surface had been achieved in the Pt-SiO_x-nSi cells, the small-signal capacitance C of these devices was measured as a function of reverse bias. The resulting plot of $1/C^2$ versus V for a representative diode is shown in Fig. 5.3. Using the method of least squares, the slope and voltage-axis intercept V_C of the line best fitting the data of Fig. 5.3 were computed. The slope was found to correspond to a doping density of $1.0*10^{15}$ cm^{-3}, which agrees closely with the doping level expected for 5 Ωcm n-type silicon. The strong inversion potential for material of this doping density is 590 mV, while V_C was found to be 620 mV, confirming that the silicon surface was indeed strongly inverted.

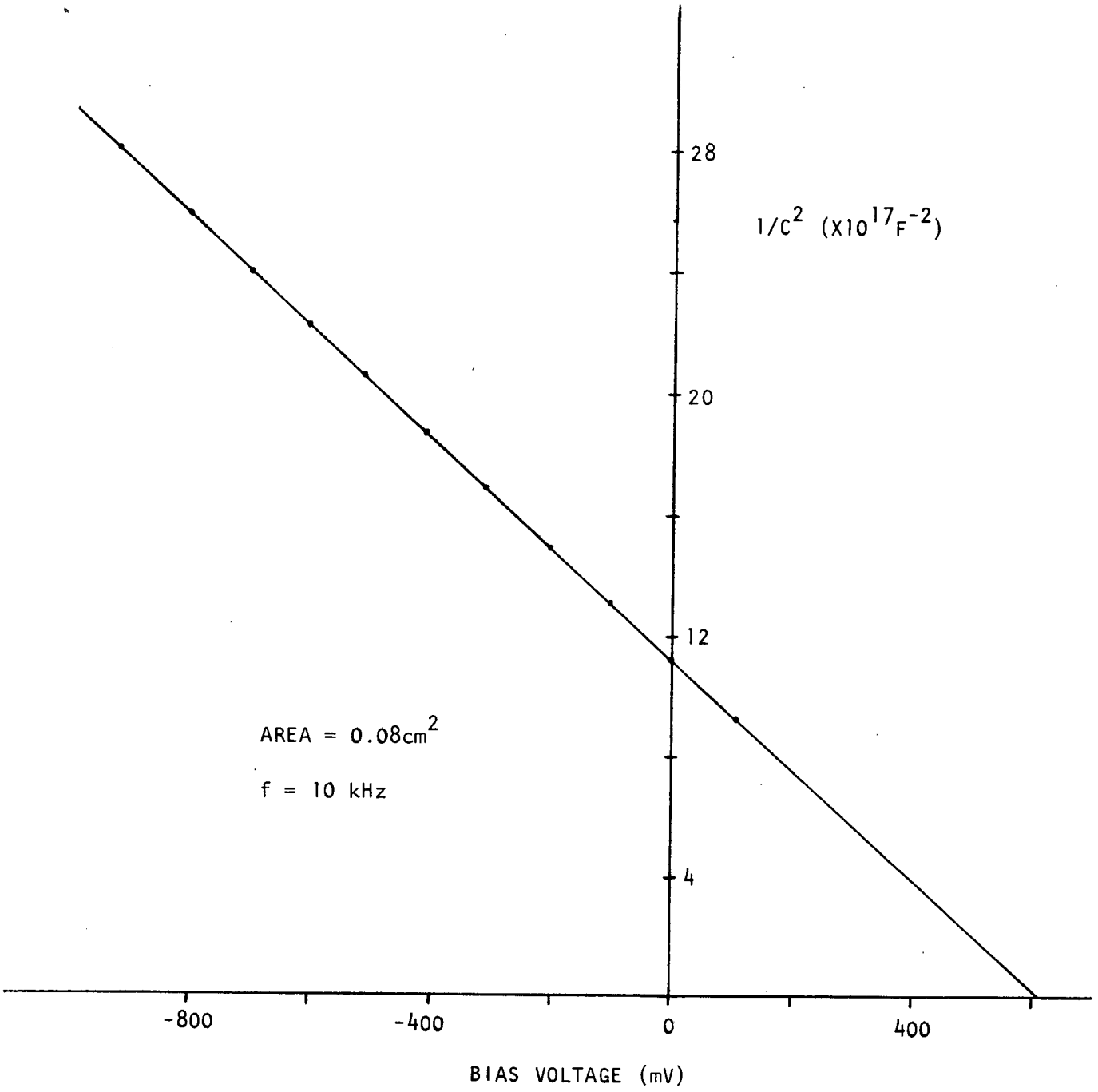

Figure 5.3 Capacitance-voltage characteristic for reverse-biased Pt-SiO_x-nSi dot diode.

Once it had been established that strong inversion of the semiconductor surface could be achieved in a Pt-SiO_x-nSi diode, a preliminary investigation of the variation of the characteristics of these devices with insulator thickness was conducted. This was done by raising the temperature at which the oxidation/annealing treatment described above was carried out, while holding the oxidation time constant. The illuminated current-voltage characteristics of the cells produced in this experiment closely resembled those of the Al-SiO_x-pSi cells discussed in Section 4.4. First, no significant variation of open-circuit voltage with oxidation temperature was observed. Secondly, cells fabricated using a 600°C oxidation/annealing sequence were found to have characteristics similar to those of cells incorporating oxides grown at 500°C; the fill factors of these devices were always greater than 0.5. However, oxidation at 650°C produced cells whose illuminated current-voltage characteristics were concave upwards over part of the power-output quadrant. As discussed in Chapter 3 and in Section 4.4, characteristics of this kind result from the tunnel resistance associated with excessively thick insulating layers.

5.3.2 Minority Carrier Reflecting Pt-SiO_x-pSi Contacts

On the basis of the experiments described above, it was concluded that there was a reasonable probability that the Pt-SiO_x-nSi cells were in fact minority carrier MIS diodes. Rather than attempting to confirm this hypothesis by, for example, measuring the temperature dependence of the current-voltage characteristics of these devices, it was decided to immediately attempt the fabrication of a minority carrier reflecting Pt-SiO_x-pSi negative barrier contact. From equation (5.6), it can readily be shown that the formation of a minority carrier reflecting contact on

a moderately doped p-type substrate is possible if and only if a minority carrier MIS diode can be formed on moderately doped n-type material. Following the general pattern of the experiments on negative barrier contacts to n-type material discussed in Section 5.2, the effective surface recombination velocity of the Pt-SiO_x-pSi contact was investigated by incorporating this structure in an induced back surface field solar cell. Pt-SiO_x-pSi back contacts were applied to both N^+P diffused front junction cells and to cells with Al-SiO_x-pSi minMIS front junctions. In accordance with the terminology introduced by Green et al, devices of the latter kind will be referred to as MISIM cells. Similarly, cells in the former class will be termed N^+PIM devices.

The substrates employed in the experiments on Pt-SiO_x-pSi contacts described in this section were supplied by Applied Solar Energy Corporation, and were cut from the same ingots used in the production of back surface field space cells. These substrates were identical to those used in the experiments discussed in Section 4.3. The substrates were of 10 Ωcm resistivity and <100> orientation, with thicknesses ranging from 350 to 400 μm. Both the front and back surfaces of the slices were chemically polished. A shallow N^+ layer was formed at the front of some of the substrates by diffusion from a phosphorus source. All slices were then shipped to the University of British Columbia for MIS contact processing.

Prior to MIS junction fabrication, all substrates were cleaned as specified in Appendix C. A thin oxide layer was then grown on the slices by exposure to dry oxygen at 600°C for 30 minutes. Following the procedure used when fabricating positive barrier junctions to n-type silicon, the furnace tube was flushed with a strong flow of dry, high-purity nitrogen

for 20 minutes before the slices were removed. For those slices lacking a diffused front junction, a thin (≈80 Å thick) semi-transparent layer of aluminum was evaporated on one surface to create a rectifying minMIS front junction. This barrier layer was then overlaid with a thick aluminum contact grid. Contact to the N^+ region of the diffused front junction substrates was made by deposition of a titanium-silver grid, which was then sintered at 500°C in hydrogen for 10 minutes. This treatment may also have helped reduce the surface state density at the back of the N^+P substrates. Processing was completed by the deposition of a platinum layer roughly 500 Å thick over the back of all the slices to form the negative barrier MIS back contact. The structure of both the N^+PIM and MISIM cells is illustrated in Fig. 5.4.

The current-voltage characteristics of the finished cells were measured under ELH lamp illumination at a controlled temperature of 28°C. Since a significant fraction of the light incident on these uncoated experimental devices was lost to reflection, the light intensity was not set to simulate one-sun illumination, but rather was adjusted to give a photocurrent density of 30 mA/cm^2 in each cell tested. This photocurrent density is slightly less than that presently attained under AM1 illumination in ASEC N^+P cells equipped with optimized anti-reflection coatings.

The ten MISIM and seven N^+PIM cells fabricated here yielded open-circuit voltages spanning a wide range, from 540 to 586 mV. Possible causes for this large spread in V_{oc} values are considered below. The significant result is that the V_{oc} values recorded for the two best N^+PIM devices were 582 and 586 mV, while the two best MISIM cells gave V_{oc}'s of 577 and 581 mV (see Table 5.2). In comparison, under the same test

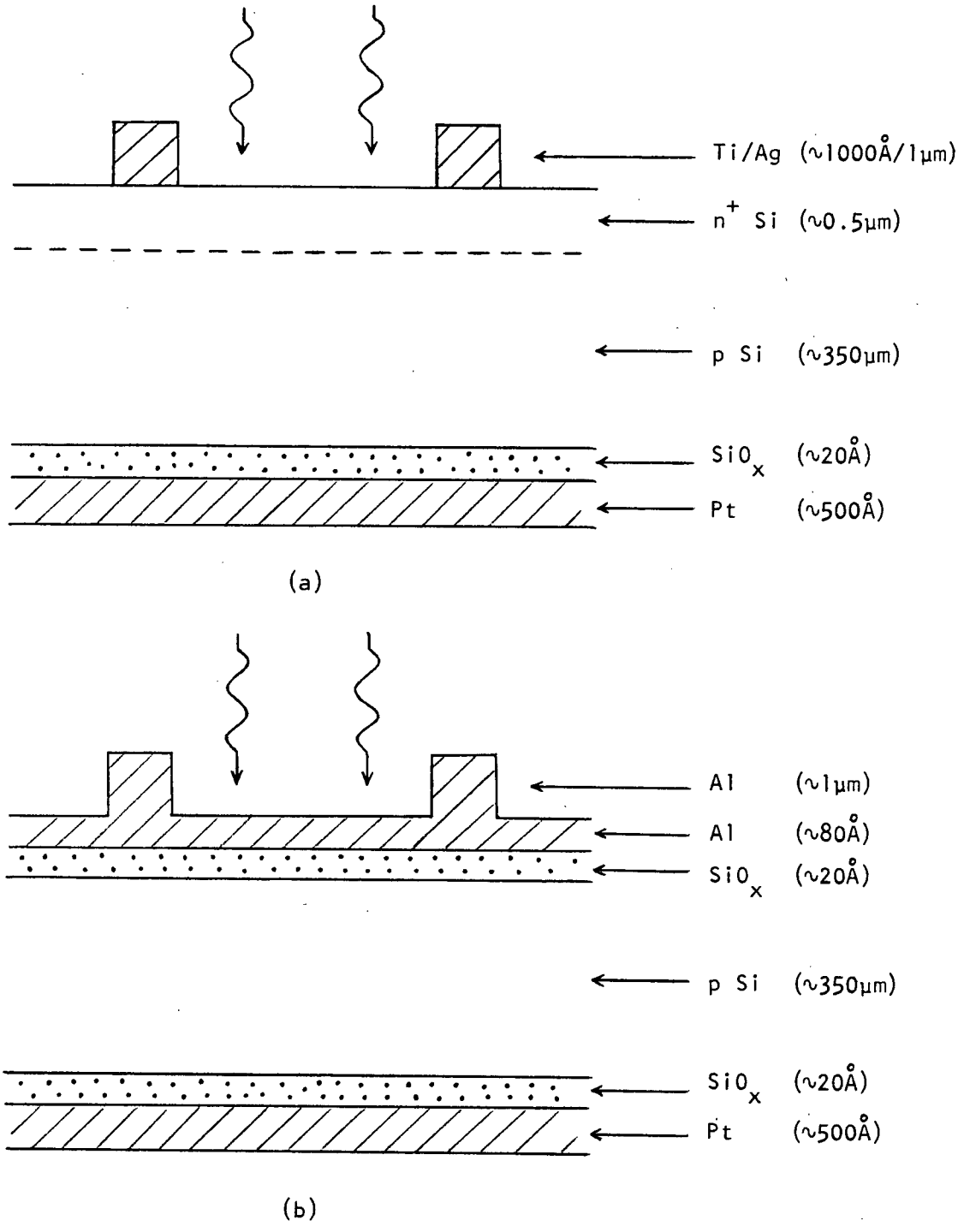

Figure 5.4 Structure of (a) N^+PIM and (b) MISIM solar cells.

conditions the group of N^+PP^+ control cells with alloyed aluminum back surface fields referred to in Section 4.3 gave a mean open-circuit voltage of 588 mV. ASEC N^+P cells lacking back surface field regions but fabricated on otherwise identical 10 Ωcm substrates give open-circuit voltages not exceeding 550 mV under these conditions. On the basis of these V_{oc} measurements, it was tentatively concluded that the negative barrier MIS back contacts to the best N^+PIM and MISIM devices were functioning as efficient minority carrier reflectors.

To provide convincing evidence that the best MISIM and N^+PIM cells were indeed exhibiting induced back surface field action, the platinum MIS back contacts to these devices were removed and replaced with ohmic contacts using only room temperature processing. Removal of the platinum metallization was accomplished by simply immersing the cells in warm methanol; the methanol rapidly undermined and lifted the platinum layers. The front metallization was then protected by applying etch-resistant adhesive tape, and the slices were dipped in 10% HF solution to remove all traces of silicon oxide from the back surface. After this oxide etch the tape was peeled away, and approximately 1,000 Å of palladium was deposited on the back of the slices by flash thermal evaporation. As discussed in Section 4.3, palladium contacts to freshly-etched p-type silicon fabricated in this fashion give ohmic characteristics with a resistance of approximately 0.1 Ωcm^2. Section 4.3 also describes control experiments carried out to ensure that the processes of taping, tape removal and palladium deposition do not harm an Al-SiO_x-pSi front junction. These processes can, of course, have virtually no effect on the properties of a diffused junction.

The V_{oc} values obtained for the reprocessed cells with palladium

TABLE 5.2 Open-circuit voltages (mV) for selected N^+PIM and MISIM cells

Cell:	With Pt MIS back contact:	With Pd back contact:
N^+PIM#1	586	543
N^+PIM#2	582	542
MISIM#1	581	545
MISIM#2	577	-

ohmic back contacts are listed in the second column of Table 5.2. On average, the open-circuit voltage dropped 40 mV after back contact refabrication, demonstrating unequivocally that the original Pt-SiO_x-pSi negative barrier contact had been significantly reducing the recombination rate at the cell back surface.

Although the open-circuit voltages of the best MISIM and N^+PIM cells fabricated to date compare favourably with those of the N^+PP^+ control cells, the yield of good devices has not been high. This low yield most likely results from difficulties in controlling the flash platinum evaporation used to create the negative barrier Pt-SiO_x-pSi contact (see Appendix C). If the deposition rate is too rapid, the heat released by the condensing platinum may raise the temperature of the substrate back surface to such an extent that the platinum will diffuse through the thin SiO_x layer and make intimate contact with the underlying silicon. Conversely, if the evaporation proceeds too slowly, tungsten may be introduced into the deposited platinum due to alloying of the tungsten filament with the molten platinum charge. Tungsten contamination is likely to lower the work function of the deposited layer, and thus reduce the barrier height of the MIS contact. From (5.5b), it can be seen that such a reduction in barrier height will increase the effective surface recombination velocity of the contact.

In Section 2.3 it was noted that the application of a minority carrier reflecting back contact to a solar cell in which the minority carrier diffusion length is greater than the base width should give a small increase in long-wavelength photocurrent response. To determine if the negative barrier Pt-SiO_x-pSi contact could provide a similar photocurrent enhancement, the photocurrent generated by cell N^+PIM#1 was

measured under infrared illumination. As described in Section 4.3, a light source rich in infrared was obtained by operating an unfiltered tungsten-halogen bulb at one-third its rated voltage. The illumination level was held constant to within ±1% by monitoring the lamp output with a reference silicon photodiode. With the original Pt-SiO_x-pSi back contact, cell N^+PIM#1 gave an infrared photocurrent of 7.2 mA. When the platinum MIS contact was replaced with a palladium ohmic contact, the photocurrent at the same illumination level dropped to 6.2 mA.

If a negative barrier MIS back contact is to be of use in increasing the efficiency of a solar cell, it is essential that it not add appreciable series resistance to the cell. Although the effective resistance of the Pt-SiO_x-pSi contact has not yet been studied in any detail, the fill factors obtained for the N^+PIM and MISIM cells fabricated thus far have been generally good, given allowance for the non-optimized front contact grids. For example, the MISIM device with the highest V_{oc} had a quite reasonable fill factor of 0.68.

CHAPTER 6

SUMMARY

In this thesis, three major original contributions are made to present understanding of the MIS tunnel diode and of photovoltaic devices in general. The first contribution is developed in Chapter 2, and centers on the discovery that previous theoretical arguments put forward to establish the validity of the principle of dark current and photocurrent superposition for homojunction solar cells contain serious flaws. In the course of correcting these flaws, the first comprehensive investigation of the behaviour of the quasi-fermi energy levels in the depletion region of an illuminated solar cell is carried out [32,33]. While in the past it had invariably been assumed that the quasi-fermi levels would always be constant across the depletion region, it is found that for operation at short circuit or small forward bias E_{Fn} and E_{Fp} change dramatically over this region. However, for cells fabricated on substrates with reasonably high carrier lifetimes and mobilities, it is found that both quasi-fermi levels become effectively constant across the depletion region for operation close to the maximum power point. From this result it follows that the superposition principle must accurately describe the characteristics of such cells at all operating points, provided the minority carrier concentrations in the quasi-neutral regions remain at low injection levels. In particular, it is shown that the superposition principle should apply even if a significant fraction of both recombination and photogeneration occur in the depletion region. This contradicts the conclusions drawn by Lindholm *et al.* in a recent publication [31]. It is also found that the superposition principle may seriously overestimate the efficiency of

cells fabricated on substrates with very poor lifetimes and low mobilities, a point which had not been appreciated previously. Although the main results presented in Chapter 2 are obtained using simple analytic methods, these results are confirmed through direct numerical solution of the differential equations governing the potentials, carrier concentrations and current flows within a solar cell. The numerical analysis is applied to both silicon and gallium arsenide cells.

The second main contribution made in this thesis is the presentation of the first conclusive experimental evidence for the existence of minority carrier MIS tunnel diodes. (In a minority carrier MIS diode, the dark current flow at moderate forward bias is dominated by the injection of minority carriers into the quasi-neutral base). Although the possibility of forming such devices had been proposed on theoretical grounds by Green et al. in 1974 [16], until the completion of the experiments described in Chapter 4 their existence remained a subject of considerable controversy. Two independent experiments were carried out here to establish that these devices could in fact be made. In the first experiment, the current-voltage characteristics of Al-SiO_x-pSi diodes were recorded as a function of temperature [20]. From this data, an activation energy describing the temperature dependence of the dark current was extracted. This activation energy was found to agree exactly with that expected for a minority carrier injection-diffusion current, and to be significantly larger than that possible for a majority carrier thermionic emission current. In the second experiment, Al-SiO_x-pSi solar cells were fabricated on substrates with alloyed aluminum back surface fields [21]. When the back surface field regions were removed by chemical etching and replaced with ohmic contacts, the open-circuit voltages of these

cells were found to drop by as much as 50 mV. This demonstration that a change in the properties of the back surface of an MIS solar cell could significantly alter the open-circuit voltage provided further irrefutable evidence for the existence of minority carrier MIS diodes.

The third principal contribution of this thesis involves a theoretical and experimental study of the properties of the negative barrier MIS junction [37]. In Chapter 5, a simple analytic model of current flow in the negative barrier junction is developed. This model predicts that with a suitable choice of insulator thickness and barrier metal work function, it should be possible to form negative barrier MIS contacts which present a very low effective surface recombination velocity to minority carriers, yet which offer negligible impedance to the flow of majority carriers. The minority carrier reflecting properties of the negative barrier MIS junction were demonstrated experimentally by utilizing this structure to form induced back surface field solar cells. Using magnesium as the barrier metal, negative barrier MIS contacts were employed to form induced back surface fields on n-type silicon substrates [37]. Diffused front junction P^+N cells were used in this experiment. Later, Pt-SiO_x-pSi negative barrier contacts were applied to form induced back surface fields on p-type material. In this second experiment, both diffused front junction N^+P cells and cells with positive barrier minMIS front junctions were used. Although the yield of Mg-SiO_x-nSi and Pt-SiO_x-pSi junctions with strong minority carrier reflecting properties was never high, the best induced back surface field cells in each class mentioned above gave open-circuit voltages comparable to those obtained with conventional back surface fields formed by diffusion or alloying. The minority carrier reflecting properties of the

negative barrier MIS back contacts were confirmed by replacing these contacts with ohmic back contacts without damaging the front junction. When this was done, the cell open-circuit voltage dropped significantly. It was also shown that a Pt-SiO_x-pSi induced back surface field could enhance the infrared photocurrent response of an N^+P cell. Although no direct measurements of the effective resistance of the Mg-SiO_x-nSi and Pt-SiO_x-pSi negative barrier contacts were made, the fill factors of the induced back surface field cells incorporating these contacts were found to be reasonably high.

In addition to the three main contributions outlined above, a theoretical model of current flow in the positive barrier MIS junction is developed in Chapter 3. This model is based largely on earlier theoretical studies carried out by Green et al. [16,17] and by Card and Rhoderick [26-28]. However, the model presented here has the advantages of being purely analytic, unlike that developed by Green et al, and of allowing for strong inversion of the semiconductor surface, unlike that proposed by Card and Rhoderick. The main drawback of the model is its inability to account for the effects of surface states on current flows or on the electrostatic potential distribution across the junction. In any case, surface state effects are best handled by resorting to entirely numerical methods, as did Green et al. Perhaps the most interesting prediction made by the model is that the illuminated current-voltage characteristics of thick-insulator MIS solar cells will be concave-upwards over a certain bias range. Experimental confirmation of this prediction is provided in Chapter 4. The development of the MIS junction model was motivated in part by suggestions made recently that the MIS tunnel diode is a fundamentally different device than the non-ideal Schottky diode. In Chapter 3

it is shown that the operation of both these devices can be explained using the same basic model.

Although the metal-insulator-semiconductor tunnel junction has been the subject of well over one hundred scientific papers in the past decade, much research remains to be done on this structure. A number of possible topics for future study arise as straightforward extensions of the results presented in this thesis. First, a direct demonstration that minority carrier MIS diodes can be formed on n-type silicon would be of interest. On a more fundamental front, the analytic model of the MIS junction developed in Chapter 3 should be modified to allow for degenerate carrier concentrations at the semiconductor surface. Above all, a comprehensive investigation should be undertaken to determine whether negative barrier MIS junctions can simultaneously supply lower effective surface recombination velocities and lower contact resistances than back surface field regions formed using conventional techniques. The development of more effective back surface field structures is a subject of considerable importance in view of the recent trend towards the use of lightweight silicon cells only 50 to 100 μm thick for space applications [134]. In order to function efficiently, such cells must incorporate high quality back surface fields.

APPENDIX A

NUMERICAL SOLUTION OF THE BASIC SEMICONDUCTOR EQUATIONS

The operation of any semiconductor device is governed by the basic equations of semiconductor physics: the current equations, the continuity equations, and Poisson's equation. An exact analytic solution of these coupled non-linear differential equations is possible only in the simplest circumstances. The first application of numerical methods to solve the basic equations was reported in 1964 by Gummel [116], who obtained solutions for the carrier concentrations and flows in one-dimensional diode and bipolar transistor structures under steady-state conditions. The algorithm introduced by Gummel was later modified and extended by DeMari [117] and Arandjelovic [118]. Unfortunately, in 1972 Choo [119] discovered that Gummel's algorithm would not converge in many situations of practical interest. This failure to converge was also demonstrated on analytic grounds at this time by Mock [120].

In response to the failure of Gummel's algorithm, Seidman and Choo [51] developed a completely new method for the numerical solution of the basic equations in their steady-state, one-dimensional form ((2.3)-(2.7)). The algorithm devised by Seidman and Choo is at once intuitively pleasing, simple to implement, and computationally efficient. It is thus hardly surprising that this algorithm and its variants have seen extensive use in the modelling of semiconductor devices in recent years [121-123]. In this appendix, the application of Seidman and Choo's algorithm to the modelling of silicon and GaAs homojunction solar cells is considered in detail. For notational convenience, the algorithm is developed in reference to NP devices, after which the few simple modif-

ications required to treat PN cells are considered.

Before any progress can be made in the solution of (2.3)-(2.7), an explicit relationship between the free carrier concentrations n and p and the recombination rate U must be specified, as must boundary conditions on n, p and ψ. Band-to-band recombination is likely to be important in GaAs, which is a direct bandgap material [125]. However, for simplicity only recombination through trapping centers will be considered here. Seidman and Choo assumed that the dependence of U on n and p could be accurately described by a Shockley-Read-Hall model [124] with a single trapping level at midgap. In this case,

$$U = (np - n_i^2)/[\tau_p(n + n_i) + \tau_n(p + n_i)]. \qquad (A.1)$$

The boundary conditions imposed on (2.3)-(2.7) will be those described in subsection 2.2.2 (see equations (2.8)-(2.9) and associated discussion).

NORMALIZATION

All numerical methods for the solution of (2.3)-(2.7) begin with a normalization of variables designed to eliminate as many constant factors from the equations as possible, and thus minimize computational time. The normalization procedure followed here is that introduced by DeMari [117], and is summarized in Table A.1. For the remainder of this appendix, all symbols will refer to normalized quantities unless otherwise specified.

In terms of normalized variables, (2.3)-(2.7) become

$$dJ_n/dx = U - G \qquad (A.2)$$

$$dJ_p/dx = -U + G \qquad (A.3)$$

TABLE A.1 Normalization factors

Variable to be normalized:	Divide by:
x	L_D (= $[\varepsilon kT/q^2 n_i]^{1/2}$)
n,p	n_i
ψ	V_{Th} (= kT/q)
J_n,J_p	$qD_0 n_i/L_D$
D_n,D_p	D_0 (= 1 $m^2 s^{-1}$)
τ_n,τ_p	L_D^2/D_0
U,G	$D_0 n_i/L_D^2$
N_A,N_D,N_T,n_1,p_1	n_i
S_F,S_B	D_0/L_D

$$J_n = D_n[-n(d\psi/dx) + dn/dx] \tag{A.4}$$

$$J_p = -D_p[p(d\psi/dx) + dp/dx] \tag{A.5}$$

$$d^2\psi/dx^2 = -(p + N_D - N_A - n) \tag{A.6}$$

while boundary conditions (2.8) and (2.9) become

$$-J_n(x_B) = S_B[n_p(x_B) - n_{p0}(x_B)] \tag{A.7}$$

and

$$-J_p(x_F) = S_F[p_n(x_F) - p_{n0}(x_F)]. \tag{A.8}$$

The SRH expression for the recombination rate becomes

$$U = (pn - 1)/(\tau_p n + \tau_n p + \tau_p + \tau_n) \tag{A.9}$$

for a trapping center at midgap.

At this stage Seidman and Choo found it convenient to introduce two new variables u and v defined according to

$$u = ne^{-\psi} \tag{A.10}$$

and

$$v = pe^{\psi}. \tag{A.11}$$

u and v bear the following simple relationship to the quasi-fermi

potentials ϕ_n and ϕ_p:

$$\phi_n = -\ln(u) \tag{A.12}$$

and

$$\phi_p = \ln(v). \tag{A.13}$$

In terms of u and v, the current equations can be written in a particularly simple form. For example, noting that

$$du/dx = (dn/dx)e^{-\psi} - ne^{-\psi}(d\psi/dx) = [-n(d\psi/dx) + dn/dx]e^{-\psi}$$

it can be seen by comparison with (A.4) that

$$J_n = D_n e^{\psi}(du/dx). \tag{A.14}$$

Similarly,

$$J_p = -D_p e^{-\psi}(dv/dx). \tag{A.15}$$

Defining a quantity

$$B = \tau_p n + \tau_n p + \tau_p + \tau_n = \tau_p u e^{\psi} + \tau_n v e^{-\psi} + \tau_p + \tau_n \tag{A.16}$$

the current and continuity equations can be combined to give

$$-\frac{d}{dx}[D_n e^{\psi}(du/dx)] + \frac{uv}{B} = \frac{1}{B} + G \tag{A.17}$$

and

$$-\frac{d}{dx}[D_p e^{-\psi}(dv/dx)] + \frac{vu}{B} = \frac{1}{B} + G. \qquad (A.18)$$

LINEARIZATION OF THE BASIC EQUATIONS

Seidman and Choo proposed that (A.17) and (A.18) could be linearized as follows. On any given iteration, let $\bar{u}$, $\bar{v}$ and $\bar{\psi}$ be the estimates for u, v and ψ obtained on the preceding iteration. Then a linear approximation to (A.17) is

$$-\frac{d}{dx}[D_n e^{\bar{\psi}}(du/dx)] + \frac{u\bar{v}}{\bar{B}} = \frac{1}{\bar{B}} + G \qquad (A.19)$$

while a linear approximation to (A.18) is

$$-\frac{d}{dx}[D_p e^{-\bar{\psi}}(dv/dx)] + \frac{v\bar{u}}{\bar{B}} = \frac{1}{\bar{B}} + G. \qquad (A.20)$$

Poisson's equation can also be linearized by letting $\psi = \bar{\psi} + \delta$. To first order in δ, (A.6) becomes

$$-d^2\delta/dx^2 + \delta(\bar{u}e^{\bar{\psi}} + \bar{v}e^{-\bar{\psi}}) = d^2\bar{\psi}/dx^2 - \bar{u}e^{\bar{\psi}} + \bar{v}e^{-\bar{\psi}} + N_D - N_A. \qquad (A.21)$$

Each of equations (A.19)-(A.21) is of the form

$$-(\alpha y')' + \beta y = f \qquad (A.22)$$

where ' denotes differentiation with respect to x. To solve (A.22) numerically, a set of grid points $\{x_j, j=1,M\}$ is introduced, and derivatives with respect to x are approximated by taking finite differences. At each interior point (that is, a point for which $2 \le j \le M-1$) grid spacings

$$h_j^- = x_j - x_{j-1} \tag{A.23}$$

and

$$h_j^+ = x_{j+1} - x_j \tag{A.24}$$

are defined. Then midway between points x_j and x_{j-1}, a reasonable approximation to $\alpha y'$ is

$$\alpha y' \simeq \frac{(\alpha_{j-1} + \alpha_j)}{2} \cdot \frac{(y_j - y_{j-1})}{h_j^-}$$

(Here the notation $\alpha_j = \alpha(x_j)$, $y_j = y(x_j)$, etc. is used).
Similarly, between points x_j and x_{j+1}, a reasonable approximation to $\alpha y'$ is

$$\alpha y' \simeq \frac{(\alpha_j + \alpha_{j+1})}{2} \cdot \frac{(y_{j+1} - y_j)}{h_j^+} \quad .$$

Therefore at point x_j

$$(\alpha y')'\Big|_{x_j} \simeq \left[\frac{(\alpha_j + \alpha_{j+1})}{2} \cdot \frac{(y_{j+1} - y_j)}{h_j^+} - \frac{(\alpha_j + \alpha_{j-1})}{2} \cdot \frac{(y_j - y_{j-1})}{h_j^-} \right] \frac{1}{(h_j^-/2 + h_j^+/2)} \quad . \tag{A.25}$$

Defining

$$\chi_j^+ = (\alpha_j + \alpha_{j+1})/h_j^+ \qquad (A.26a) \qquad \chi_j^- = (\alpha_j + \alpha_{j-1})/h_j^- \qquad (A.26b)$$

and

$$\eta_j^+ = \chi_j^+/(h_j^+ + h_j^-) \qquad (A.27a) \qquad \eta_j^- = \chi_j^-/(h_j^+ + h_j^-) \qquad (A.27b)$$

(A.25) becomes

$$-(\alpha y')'|_{x_j} \simeq [-\eta_j^+ y_{j+1} - \eta_j^- y_{j-1} + (\eta_j^+ + \eta_j^-)y_j]. \qquad (A.28)$$

Thus at any interior grid point the differential equation (A.22) takes the finite difference form

$$a_j y_j + b_j y_{j-1} + c_j y_{j+1} = f_j \qquad (A.29a)$$

where

$$a_j = \eta_j^+ + \eta_j^- + \beta_j \ , \qquad (A.29b)$$

$$b_j = -\eta_j^- \qquad (A.29c)$$

and

$$c_j = -\eta_j^+ . \qquad (A.29d)$$

The only problem now remaining is the imposition of boundary conditions at x_1 and x_M. At x_1, the values of u and ψ are fixed once the bias V is specified. Similarly, v and ψ are fixed at x_M. With boundary conditions of this type, (A.29) still holds with $a_1 = 1$, $b_1 = 0$, $c_1 = 0$ and $f_1 = y_1$, and $a_M = 1$, $b_M = 0$, $c_M = 0$ and $f_M = y_M$. In finite difference form (A.7) becomes

$$[\chi_M^-/2 + S_B \exp(\bar{\psi}_M)]\, u_M - u_{M-1}\,(\chi_M^-/2) = S_B\, n_{p0}(x_B) \qquad (A.30)$$

where the value of χ_M^- is that appropriate to (A.19). Similarly, (A.8) becomes

$$[\chi_1^+/2 + S_F \exp(-\bar{\psi}_1)]\, v_1 - v_2\,(\chi_1^+/2) = S_F\, p_{n0}(x_F) \qquad (A.31)$$

where χ_1^+ is appropriate to (A.20). Clearly both (A.30) and (A.31) are of the form (A.29a).

SOLUTION OF THE LINEARIZED BASIC EQUATIONS

Equation (A.29a) can be expressed in matrix form as

$$A\,\vec{y} = \vec{f} \qquad (A.32a)$$

where

$$A = \begin{bmatrix} a_1 & c_1 & & & & & \\ b_2 & a_2 & c_2 & & & & \\ & \cdot & \cdot & \cdot & & & \\ & & \cdot & \cdot & \cdot & & \\ & & & \cdot & \cdot & \cdot & \\ & & & & b_{M-1} & a_{M-1} & c_{M-1} \\ & & & & & b_M & a_M \end{bmatrix} \qquad (A.32b)$$

and $\vec{y}$ and $\vec{f}$ are column vectors with jth element y_j and f_j respectively. The matrix A has non-zero elements only on the main diagonal and on the two adjacent diagonals, and so is termed a tridiagonal band matrix. In order to solve for y, it is necessary to invert A. This can be done

conveniently using the following algorithm, which is derived by simple row-echelon reduction of A [126]:

1. Define arrays d and γ according to:

$$d_1 = a_1$$

$$\gamma_1 = c_1/d_1$$

$$d_j = a_j - b_j \gamma_{j-1} \qquad \text{(for j = 2 to M)}$$

$$\gamma_j = c_j/d_j \qquad \text{(for j = 2 to M)}$$

2. Define an array g according to:

$$g_1 = f_1/d_1$$

$$g_j = (f_j - b_j g_{j-1})/d_j \qquad \text{(for j = 2 to M)}$$

3. y is given by:

$$y_M = g_M$$

$$y_i = g_i - \gamma_i y_{i+1} \qquad \text{(for i = M-1 to 1).}$$

In order to minimize the storage space required by a computer program implementing the above algorithm, the members of the following pairs of arrays can share the same memory locations:

d and a

γ and c

g and b

INITIALIZATION AND COMPUTATIONAL PROCEDURE

To carry through one iteration of Seidman and Choo's algorithm, equations (A.19) and (A.20) are first solved in finite difference form as described above to generate improved estimates for u and v. These new values for u and v are then substituted in (A.21), which is turn solved in finite difference form to determine the correction term δ to be added

to ψ. Once the corrected value of ψ has been computed, the next iteration begins. In order to start the iterative process, it is clearly necessary to have reasonably good initial estimates for u,v and ψ. Here an estimate for ψ was obtained at each bias point V by assuming that the electrostatic potential drop $V_{bi} - V$ over the cell appears only across the depletion region, and then applying the depletion approximation. Knowing ψ, initial estimates for u and v were obtained by specifying the position of the quasi-fermi energy levels. The majority carrier quasi-fermi level was taken to be constant over each quasi-neutral region, and to extend at this constant value across the depletion region. The separation of the quasi-fermi levels in the depletion region was thus set equal to qV. Finally, the minority carrier quasi-fermi level was set to coincide with the majority carrier quasi-fermi level in each quasi-neutral region. Although this last initialization condition must seriously underestimate the minority carrier concentrations at any $V > 0$, it has not resulted in computational problems. In generating the results presented in subsection 2.2.4, the iterative process was continued until the solution for the total current flow in the diode varied by less than 0.1% between successive iterations. This generally required fewer than 20 iterations starting from the initialization outlined above.

CARRIER LIFETIMES AND MOBILITIES

The relationship between the carrier mobilities and the total substrate doping level N_T in the silicon and GaAs cells modelled here was specified by simply making a piecewise-linear approximation to the plot of the logarithm of the mobility versus the logarithm of N_T presented by Sze [127]; the points used in the piecewise linear fit are listed in Table A.2.

TABLE A.2 Data used to compute mobility

a) Data for silicon

N_T: (m^{-3})	μ_n: $(m^2V^{-1}s^{-1})$	μ_p: $(m^2V^{-1}s^{-1})$
10^{21}	$1.4*10^{-1}$	$5.8*10^{-2}$
10^{22}	$1.1*10^{-1}$	$5.0*10^{-2}$
10^{23}	$7.0*10^{-2}$	$3.3*10^{-2}$
10^{24}	$3.4*10^{-2}$	$2.0*10^{-2}$
10^{25}	$1.2*10^{-2}$	$8*10^{-3}$

b) Data for GaAs

N_T: (m^{-3})	μ_n: $(m^2V^{-1}s^{-1})$	μ_p: $(m^2V^{-1}s^{-1})$
10^{21}	$7.0*10^{-1}$	$3.7*10^{-2}$
10^{22}	$6.0*10^{-1}$	$3.2*10^{-2}$
10^{23}	$4.5*10^{-1}$	$2.3*10^{-2}$
10^{24}	$3.0*10^{-1}$	$1.3*10^{-2}$
10^{25}	$1.5*10^{-1}$	$7*10^{-3}$

For $N_T < 10^{21}$ m^{-3}, μ_n and μ_p are assigned the values listed for $N_T = 10^{21}$ m^{-3}. Otherwise, μ_n and μ_p are computed by linear interpolation or extrapolation.

When modelling silicon cells, the electron and hole lifetimes were related to the doping level through the formulas

$$\tau_p = \tau_{0p}/(1 + N_T/N_{0p}) \qquad \text{(A.33a)}$$

and

$$\tau_n = \tau_{0n}/(1 + N_T/N_{0n}) \qquad \text{(A.33b)}$$

where

$$N_T = N_A + N_D \qquad \text{(A.33c)}$$

as suggested by Fossum [128]. τ_{0n} and τ_{0p} were set equal to $1.7*10^{-5}$ s and $3.5*10^{-7}$ s respectively, while N_{0n} and N_{0p} were both set equal to $7.1*10^{15}$ cm^{-3}. Since relatively little information concerning minority carrier lifetimes in GaAs is available, τ_n and τ_p were assumed to be independent of the doping level in this material. Following Hovel [129] and Milnes and Feucht [130], τ_n was set equal to 10^{-9} s, while τ_p was set equal to 10^{-8} s.

PHOTOGENERATION

Unless otherwise stated, the photogeneration distribution G(x) was computed at each grid point from the formula

$$G(x_j) = \sum_i \exp[-\alpha(\lambda_i)\, x_j]\, M(\lambda_i)\, \Delta\lambda_i \qquad \text{(A.34)}$$

which is simply a finite-difference approximation to the integral (2.1), taking $R(\lambda) = 0$. Fifteen wavelength intervals $\Delta\lambda_i$ were used to span the solar spectrum from the wavelength corresponding to the silicon bandgap

TABLE A.3 Data used to compute photogeneration distribution

Wavelength Interval: (μm)	α_{Si}: (m^{-1})	M: (m^{-2} s^{-1})
0.28 - 0.32	$1.8*10^{8}$	$7.52*10^{18}$
0.32 - 0.36	$1.2*10^{8}$	$4.48*10^{19}$
0.36 - 0.40	$1.2*10^{7}$	$6.87*10^{19}$
0.40 - 0.44	$4.4*10^{6}$	$1.18*10^{20}$
0.44 - 0.48	$2.3*10^{6}$	$1.69*10^{20}$
0.48 - 0.52	$1.4*10^{6}$	$1.79*10^{20}$
0.52 - 0.56	$9.0*10^{5}$	$1.76*10^{20}$
0.56 - 0.60	$6.3*10^{5}$	$1.75*10^{20}$
0.60 - 0.64	$4.0*10^{5}$	$1.90*10^{20}$
0.64 - 0.68	$3.0*10^{5}$	$1.83*10^{20}$
0.68 - 0.72	$2.0*10^{5}$	$1.83*10^{20}$
0.72 - 0.76	$1.6*10^{5}$	$1.71*10^{20}$
0.76 - 0.80	$1.0*10^{5}$	$1.61*10^{20}$
0.80 - 1.00	$4.1*10^{4}$	$7.00*10^{20}$
1.00 - 1.20	$5*10^{2}$	$5.91*10^{20}$ †

α_{Si} is the absorption coefficient for silicon.

For the GaAs cell, a uniform photogeneration distribution was used.

The total photogeneration in the GaAs cell was set equal to $1.88*10^{21}$ m^{-2}.

† with energies greater than the silicon bandgap

to the ultraviolet; λ_i is the central wavelength of the ith interval. The absorption coefficient $\alpha(\lambda_i)$ was extracted from the graphical data presented by Sze [40], while the total photon flux $M(\lambda_i)\Delta\lambda_i$ in the interval was computed from the AM1 spectral composition specified in Ref.[131]. These data are summarized in Table A.3. Although far more accurate representations of $\alpha(\lambda)$ and the solar spectral irradiance are available, this procedure was deemed adequate for the purpose of testing the validity of the superposition principle. Any reader intending to use the programs presented in this appendix for very accurate modelling of solar cell performance should investigate the techniques employed to compute the photogeneration distribution by Fossum [128] and by Dunbar and Hauser [123], rather than using the crude approximation to G(x) given here.

GRID SELECTION

The selection of an appropriate grid geometry is a central part of any numerical analysis problem. The grid spacing must be sufficiently fine that derivatives can be adequately approximated by finite differences, yet with too fine a grid truncation or round-off errors may seriously affect the computations. In a typical solar cell the widths of the emitter and depletion region are roughly one hundred times smaller than the width of the base. For such a device a non-uniform grid is clearly required. The basic grid structure used here contained 100 evenly-spaced points in each of the emitter, depletion and base regions. This grid structure was found to provide accurate solutions for the potentials and currents in silicon cells operated in the dark and in GaAs cells. However, when modelling illuminated silicon cells it was found advantageous to add another 100 grid points in the region extending from the depletion region/base boundary to a depth of 10 μm into the base. This modification

ensured that there would be a reasonably fine grid throughout the region of maximum photogeneration in a silicon cell. To check that a sufficiently fine grid had been chosen, under various operating conditions the spacing between grid points was halved, thereby doubling the number of points. In no circumstance did the solution for the total current change by more than 0.1% on halving the grid spacing. With 400 grid points, 20 iterations of Seidman and Choo's algorithm can be carried out in roughly 1 second of CPU time on the Amdahl 470.

Another simple check on the validity of the numerical model can be made by computing the total current -- that is, the sum of J_n and J_p -- at each grid point. This sum should be constant throughout a device, since Seidman and Choo's algorithm is based on the steady-state form of the basic equations. Here the total current was indeed found to be independent of position, except in the case of very small current flows through very heavily doped emitter regions. In such cases truncation error became a problem when computing the majority carrier current from the gradient of the majority carrier quasi-fermi potential. The solutions for the potentials and carrier concentrations themselves were unaffected by this error.

PROGRAMS

Listings and brief descriptions of the four FORTRAN programs written to implement Seidman and Choo's algorithm are given below. Although the programs listed below were written to apply to devices with n-type emitters and p-type base regions, PN structures can be treated by simply interchanging the electron and hole mobilities and lifetimes. The relationship between the FORTRAN variables appearing in the programs and the notation used in the discussion above is documented in Table A.5. The programs

were compiled with the FORTRAN G compiler, and run under MTS control. All input data supplied to the programs should be in MKS units.

SC.PARSET establishes the grid over which computations proceed, and assigns values for the doping, lifetimes, mobilities and photogeneration at each grid point. The grid is built up of an arbitrary number of sections of width WSECT, each containing NSEG segments. The input values of WSECT and NSEG used in obtaining the data presented in subsection 2.2.4 are listed in Table A.4. The input of a value of NSEG ≤ 0 terminates the grid construction. In the form listed below the program assumes that the cell has been fabricated on a uniformly-doped p-type silicon substrate without a back surface field. The doping profile is assumed to be Gaussian, but the program accepts values for the metallurgical junction depth XJNCT, surface doping concentration N_{D0}, substrate doping N_A and surface recombination velocities S_F and S_B as input data. Values for $\alpha(\lambda)$ and the photon flux are read in from the file SPDTFL. All quantities computed by this program are written to the sequential file GPARFL.

SC.INIT computes initial values for u, v and ψ in accordance with the procedure specified above. The program requires the terminal voltage VOLT to be specified as input data. Values for u, v and ψ are written to the sequential file UVPSFL.

SC.CALC uses Seidman and Choo's algorithm to obtain improved estimates for u, v and ψ. The number of iterations to be performed NCNTRL, the terminal voltage and the number-of-suns illumination RSUNS are supplied as input data.

SC.READOUT computes and outputs values for n, p, ψ, J_n, J_p and total current J_T at selected grid points. The input data for this program specifies the grid point JSTART at which sampling is to begin, the grid point JSTOP at which sampling is to end, and the spacing INCR between points sampled.

TABLE A.4 Parameters used for grid construction

a) Silicon cell

NSEG:	WSECT:
100	0.5D-6
100	0.5D-6
50	2.5D-6
50	6.5D-6
100	240.0D-6

b) GaAs cell

NSEG:	WSECT:
100	0.2D-6
100	0.2D-6
100	9.6D-6

TABLE A.5 Explanation of variables used in FORTRAN programs

FORTRAN VARIABLE:	QUANTITY REPRESENTED:
VTH	kT/q
NI	n_i
LDEBYE	L_D
EPSI	ε
Q	q
TO	τ_0
HJM	h_j^-
HJP, H(J)	h_j^+
HSUM	$h_j^+ + h_j^-$
XJ	x_j
JMAX	M (number of grid points)
VBI	V_{bi}
WO	W_0 (depletion region width at V = 0)
XJNCT	(metallurgical junction depth)
NA	N_A
NDO	N_{D0}
NT	N_T
LNT	$\log_{10}(N_T)$
NNOF	$n_{n0}(x_F)$
PNOF	$p_{n0}(x_F)$
PPOB	$p_{p0}(x_B)$
NPOB	$n_{p0}(x_B)$
PFLX	$M(\lambda_i)\Delta\lambda_i$
GO	G_0 (photogeneration at surface)

FORTRAN VARIABLE:	QUANTITY REPRESENTED:
MU	μ
MUN	μ_n
MUP	μ_p
LNDT,LMUNDT,LMUPDT	(data used to compute mobility)
DN(J),DNJ	$D_{n,j}$
DNJP	$D_{n,j+1}$
DP(J),DPJ	$D_{p,j}$
DPJP	$D_{p,j+1}$
TN(J),TNJ	$\tau_{n,j}$
TP(J),TPJ	$\tau_{p,j}$
N(J)	$N_A - N_D$
U(J),UJ	u_j
V(J),VJ	v_j
PSI(J),PSIJ	ψ_j
PSIJM	ψ_{j-1}
PSIJP	ψ_{j+1}
DELTA	δ_j
F(J),FJ	f_j
XPSIJ	$\exp(\psi_j)$
XPSIJP	$\exp(\psi_{j+1})$
CHIJMU,CHIJMV	χ_j^-
CHIJPU,CHIJPV	χ_j^+
ETAJM	η_j^-
ETAJP	η_j^+
AU(J),AV(J),APSI(J),A(J)	a_j
BU(J),BV(J),BPSI(J),B(J)	b_j
CU(J),CV(J),CPSI(J),C(J)	c_j

FORTRAN VARIABLE:	QUANTITY REPRESENTED:
VOLT	V
VBAR	$V_{bi} - V$
RSUNS	(number-of-suns)
NCNTRL	(number of iterations)
JN	J_n
JP	J_p
JT	J_T
PHIP	ϕ_p
PHIN	ϕ_n

```
C PROGRAM SC.PARSET
C WRITTEN BY GARRY TARR FEB/81
C
      IMPLICIT REAL*8 (A-H,O-Z)
      INTEGER FREE,SPDTFL,GPARFL
      REAL*4 H,DN,DP,TN,TP,G,N
      REAL*8 LDEBYE,NI,NA,ND0,NN0F,NP0B,
     #K,KS,NT,N0TN,N0TP,LNDT,LMUNDT,LMUPDT,MUN,MUP,LNT,ND
      DIMENSION H(801),N(801),DN(801),DP(801),TN(801),TP(801),
     #G(801),FREE(1),PFLX(100),ALPHA(100),
     #LNDT(5),LMUNDT(5),LMUPDT(5)
C
      DATA FREE/'*'/,KR/5/,LP/6/,IMUDT/5/,SPDTFL/4/,GPARFL/3/,
     #K/1.38054D-23/,Q/1.6021D-19/,EPSI0/8.854D-12/,T/300.0D0/,
     #NI/1.45D16/,KS/11.7D0/,
     #NA/5.0D21/,ND0/1.0D25/,XJNCT/0.5D-6/,SF/1.0D3/,SB/1.0D30/,
     #N0TN/7.1D21/,N0TP/7.1D21/,TN0/1.7D-5/,TP0/3.5D-7/,
     #LNDT/2.1D1,2.2D1,2.3D1,2.4D1,2.5D1/,
     #LMUPDT/-1.236D0,-1.30D0,-1.48D0,-1.70D0,-2.10D0/,
     #LMUNDT/-0.845D0,-0.96D0,-1.16D0,-1.46D0,-1.92D0/
C
C
      J=1
C
100   READ(KR,FREE,ERR=51,END=51) NSEG,WSECT
      IF(NSEG .LE. 0) GOTO 300
C
      HH=WSECT/NSEG
      DO 200 JJ=1,NSEG
      H(J)=HH
      J=J+1
200   CONTINUE
      GOTO 100
300   JMAX=J
      IF(JMAX .LE. 810) GOTO 400
      WRITE(LP,101)
101   FORMAT(1X,'TOO MANY GRID POINTS')
      STOP
400   H(JMAX)=0.0
C
      READ(KR,FREE,ERR=52,END=500) NA,ND0,XJNCT,SF,SB
C
500   EPSI=EPSI0*KS
      VTH=K*T/Q
      LDEBYE=DSQRT(EPSI*VTH/Q/NI)
      T0=LDEBYE*LDEBYE
      NN0F=(ND0-NA)/NI
      PN0F=NI/(ND0-NA)
      PP0B=NA/NI
      NP0B=NI/NA
      SF=SF*LDEBYE
      SB=SB*LDEBYE
      VBI=VTH*DLOG(NN0F*PP0B)
      W0=DSQRT(2.0D0*EPSI*VBI/Q/NA)/LDEBYE
C
      REWIND SPDTFL
```

```
      DO 600 I=1,100
600   READ(SPDTFL,FREE,ERR=4,END=700) ALPHA(I),PFLX(I)
      GOTO 4
C
700   ISPDT=I-1
      CDIFF=DLOG(ND0/NA)/XJNCT/XJNCT
      XJNCT=XJNCT/LDEBYE
C
C
      XJ=0.0D0
      DO 1000 J=1,JMAX
      ND=0.0D0
      XX=XJ*XJ*CDIFF
      IF(XX .GT. 1.0D2) GOTO 800
      ND=ND0*DEXP(-XX)
800   NT=ND+NA
      N(J)=(ND-NA)/NI
      LNT=DLOG10(NT)
      CALL FINDMU(LNT,MUN,LNDT,LMUNDT,IMUDT)
      DN(J)=VTH*MUN
      CALL FINDMU(LNT,MUP,LNDT,LMUPDT,IMUDT)
      DP(J)=VTH*MUP
      TN(J)=TN0/(1.0D0+NT/N0TN)/T0
      TP(J)=TP0/(1.0D0+NT/N0TP)/T0
C
      G(J)=0.0
      DO 900 I=1,ISPDT
      G0=PFLX(I)*ALPHA(I)/NI*T0
      XX=XJ*ALPHA(I)
      IF(XX .GT. 1.0D2) GOTO 900
      G(J)=G(J)+G0*DEXP(-XX)
900   CONTINUE
C
      XJ=XJ+H(J)
      H(J)=H(J)/LDEBYE
1000  CONTINUE
C
C
      WRITE(LP,102) XJ,JMAX
102   FORMAT(1X/1X,'DEVICE WIDTH = ',D17.6,5X,'NUMBER OF
     #GRID POINTS = ',I4)
      REWIND GPARFL
      WRITE(GPARFL) H,JMAX,VTH,NI,LDEBYE,XJNCT,NA,ND0,
     #NN0F,PN0F,PP0B,NP0B,VBI,W0,SF,SB,N,DN,DP,TN,TP,G
C
      STOP
4     STOP 4
51    STOP 51
52    STOP 52
      END
```

```
      SUBROUTINE FINDMU(LNT,MU,LNDT,LMUDT,IMUDT)
C
      IMPLICIT REAL*8 (A-H,O-Z)
      REAL*8 LNT,MU,LNDT,LMUDT,LMU
     .DIMENSION LNDT(IMUDT),LMUDT(IMUDT)
C
      DATA TEN/1.0D1/
C
      LMU=LMUDT(1)
      IF(LNT .LE. LNDT(1)) GOTO 300
      ISTOP=IMUDT-1
      DO 100 I=1,ISTOP
      IF( (LNT .GE. LNDT(I)) .AND. (LNT .LT. LNDT(I+1)) ) GOTO 200
100   CONTINUE
      I=ISTOP
C
200   LMU=LMUDT(I)-(LMUDT(I)-LMUDT(I+1))/(LNDT(I+1)-LNDT(I))*
     #(LNT-LNDT(I))
300   MU=TEN**LMU
C
      RETURN
      END
```

```
C PROGRAM SC.INIT
C WRITTEN BY GARRY TARR FEB/81
C
      IMPLICIT REAL*8 (A-H,O-Z)
      INTEGER FREE,GPARFL,UVPSFL
      REAL*8 LDEBYE,NI,NA,ND0,NN0F,NP0B
      REAL*4 H
      DIMENSION U(801),V(801),PSI(801),H(801),FREE(1)
C
      DATA NCNTRL/0/,RSUNS/0.0D0/,FREE/'*'/,KR/5/,UVPSFL/2/,
     #GPARFL/3/
C
C
      READ(KR,FREE,ERR=5,END=5) VOLT
C
      REWIND GPARFL
      READ(GPARFL,ERR=3,END=3) H,JMAX,VTH,NI,LDEBYE,XJNCT,NA,
     #ND0,NN0F,PN0F,PP0B,NP0B,VBI,W0
C
      VBAR=VBI-VOLT
      DVBAR=DEXP(VBAR/VTH)
      W=W0*DSQRT(VBAR/VBI)
C
      XJ=0.0D0
      DO 100 J=1,JMAX
      IF(XJ .GE. XJNCT) GOTO 200
      PSI(J)=0.0D0
      U(J)=NN0F
      V(J)=PN0F
      XJ=XJ+H(J)
100   CONTINUE
C
200   JJ=J
      RJ=0.0D0
      DO 300 J=JJ,JMAX
      RJ=RJ+H(J)/W
      IF(RJ .GT. 1.0D0) GOTO 400
      PSI(J)=2.0D0*VBAR*(0.5D0*RJ*RJ-RJ)/VTH
      U(J)=NN0F
      V(J)=PP0B/DVBAR
300   CONTINUE
C
400   JJ=J
      DO 500 J=JJ,JMAX
      PSI(J)=-VBAR/VTH
      U(J)=NP0B*DVBAR
      V(J)=PP0B/DVBAR
500   CONTINUE
C
      REWIND UVPSFL
      WRITE(UVPSFL) U,V,PSI,VOLT,RSUNS,NCNTRL
C
      STOP
3     STOP 3
5     STOP 5
      END
```

```
C PROGRAM SC.CALC
C WRITTEN BY GARRY TARR FEB/81
C
      IMPLICIT REAL*8 (A-H,O-Z)
      INTEGER FREE,GPARFL,UVPSFL
      REAL*8 LDEBYE,NI,NA,ND0,NN0F,NP0B
      REAL*4 H,N,DN,DP,TN,TP,G
      DIMENSION U(801),AU(801),BU(801),CU(801),F(801),
     #V(801),AV(801),BV(801),CV(801),
     #PSI(801),APSI(801),BPSI(801),CPSI(801),DELTA(801),
     #H(801),N(801),DN(801),DP(801),TN(801),TP(801),G(801)
     #FREE(1)
      EQUIVALENCE (BU,APSI),(CU,BPSI),(BV,CPSI),(CV,DELTA)
C
      DATA ZERO/0.0D0/,ONE/1.0D0/,TWO/2.0D0/,
     #KR/5/,UVPSFL/2/,GPARFL/3/,FREE/'*'/
C
C
      READ(KR,FREE,END=5,ERR=5) NCNTRL,VOLT,RSUNS
      REWIND UVPSFL
      READ(UVPSFL,ERR=2,END=2) U,V,PSI
      REWIND GPARFL
      READ(GPARFL,ERR=3,END=3) H,JMAX,VTH,NI,LDEBYE,XJNCT,NA,
     #ND0,NN0F,PN0F,PP0B,NP0B,VBI,W0,SF,SB,N,DN,DP,TN,TP,G
C
      DO 50 J=1,JMAX
      G(J)=G(J)*RSUNS
50    CONTINUE
      DVBAR=DEXP((VBI-VOLT)/VTH)
      U(JMAX)=NP0B*DVBAR
      V(JMAX)=PP0B/DVBAR
      PSI(JMAX)=-(VBI-VOLT)/VTH
      JSTOP=JMAX-1
C
C
C
      DO 1000 ICNTRL=1,NCNTRL
C
C
      DNJ=DN(1)
      DPJ=DP(1)
      XPSIJ=DEXP(PSI(1))
      HJP=H(1)
      DNJP=DN(2)
      DPJP=DP(2)
      XPSIJP=DEXP(PSI(2))
      CHIJPU=(DNJ*XPSIJ+DNJP*XPSIJP)/HJP
      CHIJPV=(DPJ/XPSIJ+DPJP/XPSIJP)/HJP
C
      AU(1)=ONE
      CU(1)=ZERO
C
      AV(1)=CHIJPV/TWO+SF/XPSIJ
      CV(1)=-CHIJPV/TWO
C
      DNJ=DNJP
```

```
      DPJ=DPJP
      HJM=HJP
      CHIJMU=CHIJPU
      CHIJMV=CHIJPV
      XPSIJ=XPSIJP
C
      DO 100 J=2,JSTOP
      XPSIJP=DEXP(PSI(J+1))
      DNJP=DN(J+1)
      DPJP=DP(J+1)
      HJP=H(J)
      HSUM=HJM+HJP
      UJ=U(J)
      VJ=V(J)
      TNJ=TN(J)
      TPJ=TP(J)
      FJ=ONE/(TPJ*UJ*XPSIJ+TNJ*VJ/XPSIJ+TPJ+TNJ)
C
      CHIJPU=(DNJ*XPSIJ+DNJP*XPSIJP)/HJP
      ETAJM=CHIJMU/HSUM
      ETAJP=CHIJPU/HSUM
      AU(J)=ETAJM+ETAJP+VJ*FJ
      BU(J)=-ETAJM
      CU(J)=-ETAJP
C
      CHIJPV=(DPJ/XPSIJ+DPJP/XPSIJP)/HJP
      ETAJM=CHIJMV/HSUM
      ETAJP=CHIJPV/HSUM
      AV(J)=ETAJM+ETAJP+UJ*FJ
      BV(J)=-ETAJM
      CV(J)=-ETAJP
C
      F(J)=FJ+G(J)
      DNJ=DNJP
      DPJ=DPJP
      HJM=HJP
      CHIJMU=CHIJPU
      CHIJMV=CHIJPV
      XPSIJ=XPSIJP
100   CONTINUE
C
      AU(JMAX)=CHIJMU/TWO+SB*XPSIJ
      BU(JMAX)=-CHIJMU/TWO
      AV(JMAX)=ONE
      BV(JMAX)=ZERO
      F(1)=U(1)
      F(JMAX)=SB*NP0B
      CALL INVRT(U,AU,BU,CU,F,JMAX)
C
      F(1)=SF*PN0F
      F(JMAX)=V(JMAX)
      CALL INVRT(V,AV,BV,CV,F,JMAX)
C
C
      PSIJM=PSI(1)
      PSIJ=PSI(2)
```

```
      HJM=H(1)
      APSI(1)=ONE
      CPSI(1)=ZERO
C
      DO 200 J=2,JSTOP
      HJP=H(J)
      PSIJP=PSI(J+1)
      XPSIJ=DEXP(PSIJ)
      UJ=U(J)
      VJ=V(J)
      HSUM=HJM+HJP
      ETAJM=TWO/HJM/HSUM
      ETAJP=TWO/HJP/HSUM
      F(J)=ETAJP*PSIJP+ETAJM*PSIJM-(ETAJP+ETAJM)*PSIJ
     #+N(J)-UJ*XPSIJ+VJ/XPSIJ
      APSI(J)=ETAJP+ETAJM+UJ*XPSIJ+VJ/XPSIJ
      BPSI(J)=-ETAJP
      CPSI(J)=-ETAJM
      PSIJM=PSIJ
      PSIJ=PSIJP
      HJM=HJP
200   CONTINUE
C
      APSI(JMAX)=ONE
      BPSI(JMAX)=ZERO
      F(1)=ZERO
      F(JMAX)=ZERO
      CALL INVRT(DELTA,APSI,BPSI,CPSI,F,JMAX)
      DO 300 J=1,JMAX
      PSI(J)=DELTA(J)+PSI(J)
300   CONTINUE
C
C
1000  CONTINUE
C
C
C
      REWIND UVPSFL
      WRITE(UVPSFL) U,V,PSI,VOLT,RSUNS,NCNTRL
C
      STOP
2     STOP 2
3     STOP 3
5     STOP 5
      END
```

```
      SUBROUTINE INVRT(Y,A,B,C,F,JMAX)
C
      IMPLICIT REAL*8 (A-H,O-Z)
      DIMENSION Y(JMAX),A(JMAX),B(JMAX),C(JMAX),F(JMAX)
C
      DATA ZERO/0.0D0/,ONE/1.0D0/
C
C
      JSTOP=JMAX-1
C
      A(1)=A(1)
      C(1)=C(1)/A(1)
      DO 100 J=2,JSTOP
      A(J)=A(J)-B(J)*C(J-1)
100   C(J)=C(J)/A(J)
      A(JMAX)=A(JMAX)-B(JMAX)*C(JSTOP)
C
      B(1)=F(1)/A(1)
      DO 200 J=2,JMAX
200   B(J)=(F(J)-B(J)*B(J-1))/A(J)
C
      Y(JMAX)=B(JMAX)
      DO 300 J=1,JSTOP
      I=JMAX-J
300   Y(I)=B(I)-C(I)*Y(I+1)
C
      RETURN
      END
```

```
C PROGRAM SC.READOUT
C WRITTEN BY GARRY TARR FEB/81
C
      IMPLICIT REAL*8 (A-H,O-Z)
      INTEGER FREE,UVPSFL,GPARFL
      REAL*8 LDEBYE,NI,NA,ND0,NN0F,NP0B
      REAL*4 H,N,DN,DP,TN,TP,G
      DIMENSION U(801),V(801),PSI(801),
     #H(801),N(801),DN(801),DP(801),TN(801),TP(801),G(801),
     #FREE(1)
      COMMON VTH,NI,LDEBYE,U,V,PSI,DN,DP,H,JMAX
C
      DATA FREE/'*'/,KR/5/,LP/6/,GPARFL/3/,UVPSFL/2/
C
C
      REWIND GPARFL
      READ(GPARFL,ERR=3,END=3) H,JMAX,VTH,NI,LDEBYE,XJNCT,NA,
     #ND0,NN0F,PN0F,PP0B,NP0B,VBI,W0,SF,SB,N,DN,DP,TN,TP,G
      REWIND UVPSFL
      READ(UVPSFL,ERR=2,END=2) U,V,PSI,VOLT,RSUNS,NCNTRL
C
      WRITE(LP,101) NCNTRL,VOLT,RSUNS
101   FORMAT('1',10X,'ITERATION NUMBER: ',I2,5X,'VOLTAGE: ',
     #F8.5,5X,'ILLUMINATION LEVEL: ',F6.2,1X,'SUNS'//
     #1X,'J:',7X,'PSI:',12X,'PHIP:',16X,'PHIN:',15X,'P:',12X,
     #'N:',11X,'JP:',11X,'JN:',11X,'JTOT:'/)
C
100   READ(KR,FREE,ERR=5,END=500) JSTART,JSTOP,INCR
C
      DO 200 J=JSTART,JSTOP,INCR
      CALL NPCRNT(J)
200   CONTINUE
C
      WRITE(LP,102)
102   FORMAT(1X)
C
      GOTO 100
C
500   WRITE(LP,103)
103   FORMAT(1X/1X/11X,'ALL QUANTITIES IN MKS UNITS'///)
C
      STOP
2     STOP 2
3     STOP 3
5     STOP 5
      END
```

```
      SUBROUTINE NPCRNT(J)
C
      IMPLICIT REAL*8 (A-H,O-Z)
      REAL*8 JN,JP,JT,NI,LDEBYE
      REAL*4 N,P,H,DN,DP
      DIMENSION U(801),V(801),PSI(801),DN(801),DP(801),H(801)
      COMMON VTH,NI,LDEBYE,U,V,PSI,DN,DP,H,JMAX
C
      DATA Q/1.6021D-19/,TWO/2.0D0/,FOUR/4.0D0/,LP/6/
C
C
      C=Q*NI/LDEBYE
      XPSIJ=DEXP(PSI(J))
      PHIN=-VTH*DLOG(U(J))
      PHIP=VTH*DLOG(V(J))
      N=U(J)*XPSIJ*NI
      P=V(J)/XPSIJ*NI
      PSIJ=PSI(J)*VTH
C
      IF(J .EQ. 1) GOTO 100
      IF(J .EQ. JMAX) GOTO 200
      HJM=H(J-1)
      HJP=H(J)
      XPSIJM=DEXP(PSI(J-1))
      XPSIJP=DEXP(PSI(J+1))
      CHIJM=(DN(J-1)*XPSIJM+DN(J)*XPSIJ)/HJM
      CHIJP=(DN(J)*XPSIJ+DN(J+1)*XPSIJP)/HJP
      JN=(CHIJP*(U(J+1)-U(J))+CHIJM*(U(J)-U(J-1)))*C/FOUR
      CHIJM=(DP(J-1)/XPSIJM+DP(J)/XPSIJ)/HJM
      CHIJP=(DP(J)/XPSIJ+DP(J+1)/XPSIJP)/HJP
      JP=-(CHIJP*(V(J+1)-V(J))+CHIJM*(V(J)-V(J-1)))*C/FOUR
      GOTO 300
C
100   XPSIJP=DEXP(PSI(J+1))
      JN=(DN(J)*XPSIJ+DN(J+1)*XPSIJP)*(U(J+1)-U(J))/H(1)*C/TWO
      JP=-(DP(J)/XPSIJ+DP(J+1)/XPSIJP)*(V(J+1)-V(J))/H(1)*C/TWO
      GOTO 300
C
200   XPSIJM=DEXP(PSI(J-1))
      JN=(DN(J-1)*XPSIJM+DN(J)*XPSIJ)*(U(J)-U(J-1))/H(J-1)*C/TWO
      JP=-(DP(J-1)/XPSIJM+DP(J)/XPSIJ)*(V(J)-V(J-1))/H(J-1)*C/TWO
300   JT=JN+JP
C
C
      WRITE(LP,102) J,PSIJ,PHIP,PHIN,P,N,JP,JN,JT
102   FORMAT(1X,I4,2X,F13.10,2X,2(F19.16,2X),2(D12.5,2X),
     #2(D12.5,2X),D13.6)
C
      RETURN
      END
```

APPENDIX B

CALCULATION OF THE SHADOW AREA FOR AN ELLIPSOIDAL CONSTANT ENERGY SURFACE OF ARBITRARY ORIENTATION

In this appendix an expression for the shadow area σ of an ellipsoidal constant energy surface whose principal axes have an arbitrary orientation relative to the interface is derived. The shadow area can be computed most easily by working in a coordinate system in which the effective mass tensor is diagonal. In this coordinate system,

$$E(\vec{k}) = (\hbar^2/2)[k_x^2/m_x^* + k_y^2/m_y^* + k_z^2/m_z^*] \quad . \tag{B.1}$$

Thus the equation of the constant energy surface at energy E can be written in the form

$$F(k_x,k_y,k_z) = 0 \tag{B.2}$$

where

$$F(k_x,k_y,k_z) = k_x^2/a^2 + k_y^2/b^2 + k_z^2/c^2 - 1 \tag{B.3a}$$

and

$$a^2 = 2Em_x^*/\hbar^2, \quad b^2 = 2Em_y^*/\hbar^2, \quad c^2 = 2Em_z^*/\hbar^2 \quad . \tag{B.3b}$$

a, b and c are, of course, the half-lengths of the principal axes of the ellipsoidal constant energy surfaces defined by (B.2).

If the normal to the interface is represented by the vector $\hat{n} = (n_1,n_2,n_3)$, then Fig. B.1 shows that the points on the ellipsoid

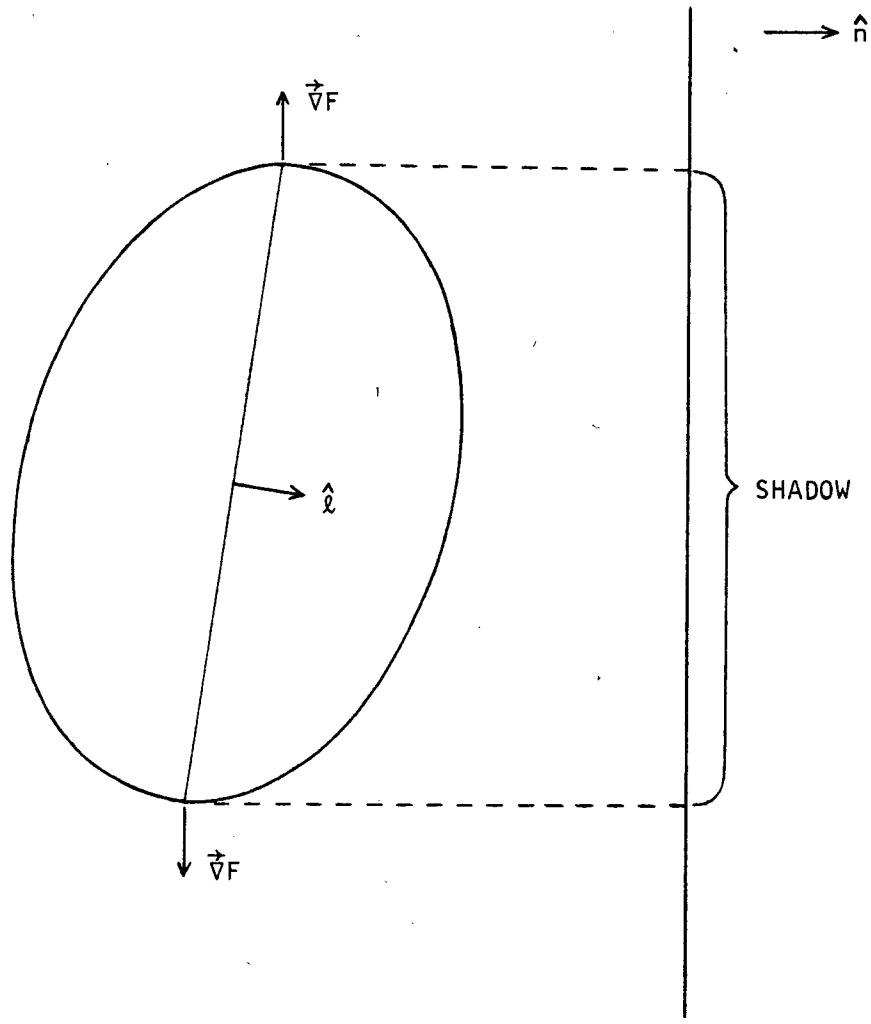

Figure B.1 Shadow of an ellipsoid.

which project to the boundaries of the shadow satisfy

$$\vec{\nabla}F\cdot\hat{n} = 0 \tag{B.4}$$

or

$$n_1 k_x/a^2 + n_2 k_y/b^2 + n_3 k_z/c^2 = 0 \ . \tag{B.5}$$

(B.5) is clearly the equation of a plane in k-space passing through the origin and with normal $\hat{\ell}$ given by

$$\hat{\ell} = (\ell_1,\ell_2,\ell_3) = (n_1/a^2, n_2/b^2, n_3/c^2)/L \tag{B.6a}$$

where

$$L = (n_1^2/a^4 + n_2^2/b^4 + n_3^2/c^4)^{1/2} . \tag{B.6b}$$

It is well known that the intersection of an ellipsoid with any plane passing through the center of the ellipsoid is an ellipse. Further, using the conventional techniques of linear algebra it can be shown that the area A of this ellipse is given by

$$A = \pi/[\ell_1^2/(b^2c^2) + \ell_2^2/(a^2c^2) + \ell_3^2/(a^2b^2)]^{1/2} \ . \tag{B.7}$$

where a, b and c are the half-lengths of the principal axes of the ellipsoid and $\hat{\ell}$ is the normal to the plane in question.

From Fig. B.1 it can be seen that the shadow area σ is related to A by

$$\sigma = A(\hat{\ell}\cdot\hat{n}). \tag{B.8}$$

Combining (B.6),(B.7) and (B.8) it is found that

$$\sigma = \pi[n_1^2b^2c^2 + n_2^2a^2c^2 + n_3^2a^2b^2]^{1/2} \ . \tag{B.9}$$

In terms of the energy E and the effective masses m_x^*, m_y^* and m_z^*,

$$\sigma = \pi(2E/\hbar^2)\ [n_1^2m_y^*m_z^* + n_2^2m_x^*m_z^* + n_3^2m_x^*m_y^*]^{1/2} \ . \tag{B.10}$$

On substituting this expression for σ into (3.19), it is found that J_{CM} is still given by (3.25), but that m_e^* is given by

$$m_e^* = [n_1^2m_y^*m_z^* + n_2^2m_x^*m_z^* + n_3^2m_x^*m_y^*]^{1/2} \ . \tag{B.11}$$

This agrees with the expression for J_{CM} Crowell [85] obtained using a direct integration over d^3k.

APPENDIX C

FABRICATION PROCEDURE FOR MIS JUNCTIONS

This appendix provides complete details of the procedure currently followed at UBC in the manufacture of both positive and negative barrier MIS junctions. This process has undergone a number of minor modifications in the past; the version described here is that in use as of late 1980. It is essential that all steps in the process be carried through without interruption, since thin silicon oxide layers grow at the rate of several angstroms per hour when exposed to the atmosphere [18].

SUBSTRATE CLEANING

Prior to junction fabrication, all substrates are subjected to the "RCA clean", a standard cleaning procedure used widely in the microelectronics industry to prepare silicon slices for high temperature processing [132]. The RCA clean recipe used here is outlined below. Normal safety precautions used in the handling of concentrated acids and bases must be observed when following this procedure. All concentrations are quoted by volume, and all chemicals should be of ACS reagent grade or higher quality. If possible, the resistivity of the deionized water should be 18 MΩcm. However, resistivities as low as 1 MΩcm have been used here without apparent effect on the properties of the finished junctions.

1. a) Immerse silicon for 10 minutes in a solution of 1 part 30% NH_4OH, 1 part 30% H_2O_2 and 5 parts deionized (DI) water held at a temperature of (80±5)°C. The solution should be prepared immediately before use, since H_2O_2 decomposes rapidly under these conditions. Further, it is important that the temperature of the solution not exceed 85°C. If the H_2O_2 concentration falls too low or the temperature rises too high, the silicon may be pitted.

b) Rinse silicon for at least 10 minutes in a DI water cascade or equivalent.

2. a) Immerse silicon for 1 minute in a solution of 1 part 49% HF to 9 parts DI water at room temperature.

   b) Rinse silicon for at least 10 minutes in DI water cascade.

3. a) Immerse silicon for 10 minutes in a solution of 1 part 36% HCl, 1 part 30% H_2O_2 and 6 parts DI water held at a temperature of (80±5)°C.

   b) Rinse silicon for at least 10 minutes in DI water cascade.

   c) Dry silicon by blowing water from surface with a jet of oil-free nitrogen.

The first step of the RCA clean is intended to remove thin layers of organic contaminants from the silicon surface. The second step strips away any native oxide layer which may be present, while the third step removes heavy metals [132].

The effectiveness of the RCA clean can be monitored by noting the condition of the silicon surface as the steps listed above are carried out. Silicon slices which have been exposed to contaminated atmospheres for long periods are usually found to be hydrophobic — that is, water droplets placed on a slice tend to bead up rather than wetting the surface. Following completion of the first step of the RCA clean, the silicon should be strongly hydrophilic — that is, water should readily wet the surface. If this is not the case, then the surface has not been thoroughly degreased. After immersion in hydrofluoric acid for a few seconds, the silicon should become hydrophobic, indicating that all traces of oxide have been removed. Exposure to the $HCl:H_2O_2$ solution regrows a thin oxide layer, making the silicon hydrophilic once again.

OXIDATION

Although a very thin oxide layer is grown at the silicon surface during the last step of the RCA clean, further oxidation at temperatures greater than 400°C is required to produce minority carrier MIS diodes. No formal experiments have been carried out here to determine an optimum oxidation time, but experience indicates that oxidation at a temperature of at least 500°C for a minimum period of 20 minutes is required to produce minority carrier Al-SiO_x-pSi devices on 1 to 10 Ωcm substrates. The Al-SiO_x-pSi back surface field cells described in Section 4.3 were fabricated using a 30 minute oxidation cycle at 600°C. These cells gave both the highest open-circuit voltages and among the highest fill factors of any devices produced during this research program. As demonstrated in Section 4.4, cells incorporating oxides grown at temperatures above 600°C have excessive tunnel resistance, and give correspondingly poor fill factors under one-sun illumination.

In all the experiments on MIS diodes reported here, high temperature treatments were carried out in a quartz tube furnace with gas flows of approximately 1 L/sec. Medical grade oxygen was used for oxidation, while pre-purified nitrogen containing less than 25 ppm oxygen and water vapour was used for sintering and annealing steps. Slices were always inserted into the furnace with the side on which the MIS junction was to be formed facing the gas flow.

OHMIC CONTACT FORMATION

When working with p-type silicon substrates, ohmic back contacts can be conveniently formed by depositing a thick layer of aluminum on the back of the slice and then sintering this layer in a nitrogen atmosphere at a temperature of 500°C for 10 minutes. This technique has been found

to yield contacts with highly linear characteristics and very low resistance, even when applied to substrates with thin oxide layers formed following the procedure outlined above. As a test of contact resistance, sintered aluminum contacts of this kind were applied to both sides of a 300 μm thick, 2 Ωcm substrate. The current-voltage characteristic of this structure was then recorded using a four-point probe technique to eliminate the effects of lead resistance. The characteristic was found to obey Ohm's law out to current densities of more than 100 mA/cm^2, while the resistance measured between the two contacts was only 0.1 Ωcm^2. This is not substantially greater than the bulk resistance associated with a slice of this doping and thickness.

BARRIER METAL DEPOSITION

In all the MIS junctions described in this thesis, the barrier metal layer and any overlying contact fingers were deposited by the process of thermal evaporation. In the microelectronics industry, metallization of silicon wafers is often carried out by the processes of electron-beam evaporation or RF sputtering. These techniques were not employed here since they lead to bombardment of the substrate with X-rays and high energy electrons. This bombardment is likely to create a high density of interface states, and thus seriously degrade the performance of the finished MIS junction. However, there is a chance that high-quality MIS devices could be produced by magnetron sputtering.

The vacuum system used for evaporation was a standard CHA SEC-600 unit equipped with a Varian VHS-6 diffusion pump. In the SEC-600 system, backstreaming of fluid from the diffusion pump is restricted to some extent through the use of an optically dense water-cooled baffle and a liquid nitrogen cold trap. Unfortunately, the CHA trapping system is

decidely inferior to that used on other commercially available diffusion pumps, in that it allows a direct line of sight from the water-cooled baffle into the work chamber. There was thus a rather high probability of the silicon substrates becoming coated with a thin film of diffusion pump fluid prior to metallization. This problem was compounded by the use of relatively high vapour pressure DC 704 fluid in the diffusion pump. The effect of this possible hydrocarbon contamination on the properties of the finished MIS junctions is not known. Evaporations were usually carried out a pressures ranging from $1*10^{-6}$ to $2*10^{-6}$ Torr. For deposition rates greater than about 1 Å/sec, these pressures were low enough to prevent significant contamination of the deposited films by reaction with residual gases in the work chamber. Where possible, the thicknesses of the deposited films were measured with a quartz crystal oscillator type thickness monitor.

The barrier metals investigated here included aluminum, magnesium, palladium and platinum. Of these materials, platinum is by far the most difficult to evaporate. Platinum both melts and reaches a vapour pressure of 10^{-4} Torr at a temperature of approximately 1750°C [133]. This precludes the self-evaporation of platinum wire. Moreover, the temperature required to evaporate platinum is so high that the selection of source materials is extremely limited. Although platinum is known to alloy with tungsten, tungsten filaments were chosen as the source here. Prior to use, these filaments were cleaned by heating to white heat for several minutes under high vacuum. When carrying out the actual evaporation, the procedure followed was to gradually heat the filament until the platinum charge melted, and then quickly open the shutter covering the source while applying a brief burst of power to the filament to flash-evaporate the

charge. The substrates were thus exposed to the white-hot source for only a few seconds. It was hoped that this procedure would minimize both the alloying of the platinum charge with the filament and the heating of the silicon substrates. The source temperature required for the platinum evaporation was so high that the thickness monitor could not be used to measure the deposition rate.

In an attempt to ascertain the degree of tungsten contamination of the deposited platinum films, a blank glass microscope slide was positioned in the path of the evaporant stream during one evaporation. The composition of the film deposited on the slide was then analyzed using X-ray fluorescence spectroscopy. (The instrument used in this analysis was the scanning electron microscope system operated by the Department of Metallurgy). No tungsten lines could be detected in the fluorescent X-ray spectrum, indicating that the deposited film contained less than approximately 1% tungsten.

Compared to platinum, the materials aluminum, magnesium and palladium can be evaporated with relative ease. Here aluminum was evaporated from tungsten filaments. Aluminum barrier layers and front-contact grids were generally deposited at a rate of 2-10 Å/sec. Magnesium was evaporated from a baffled tantalum boat designed for use with SiO. Although the rate of magnesium evaporation was difficult to control, deposition rates of 10-20 Å/sec were aimed for. Finally, when carrying out the experiments on positive barrier Pd-nSi junctions described in Section 5.3, the palladium was deposited by the self-evaporation of thin wires. Since the vapour pressure of palladium reaches 10^{-4} Torr at 1200°C, yet this metal does not melt until 1550°C [133], palladium wires can readily be self-evaporated. This procedure permits palladium films of extremely high

purity to be deposited. When depositing palladium on freshly-etched silicon to form an ohmic contact, a tungsten basket was used as the evaporation source.

REFERENCES

1. Solar Photovoltaic Energy Conversion, H. Ehrenreich, chairman (American Physical Society, New York, 1979).

2. D.L. Pulfrey, Photovoltaic Power Generation (Van Nostrand Reinhold, New York, 1978).

3. J. Javetski, Electronics, p. 105 (July 19, 1979).

4. L.P. Hunt, Proceedings of the 12th IEEE Photovoltaic Specialists Conference (IEEE, New York, 1976) p. 347.

5. See, for example, the many papers on novel techniques for the purification and crystallization of silicon in the Proc. 14th IEEE Photovoltaic Spec. Conf. (IEEE, New York, 1980).

6. J. Lindmayer, Proc. 12th IEEE Photovoltaic Spec. Conf., op. cit., p. 82.

7. K. Graff, H. Pieper and G. Goldback, Semiconductor Silicon 1973 (Electrochemical Society, Princeton, 1973) p. 170.

8. R.F. McOuat and D.L. Pulfrey, J. Appl. Phys. 47, 2113 (1976).

9. An excellent review of research on the Schottky barrier junction has been given by E.H. Rhoderick in Metal-Semiconductor Contacts (Oxford University Press, New York, 1978).

10. H.A. Bethe, MIT Radiation Laboratory Report 43-12 (1942).

11. A.Y.C. Yu and E.H. Snow, J. Appl. Phys. 39, 3008 (1968).

12. D.L. Scharfetter, Solid-State Electron. 8, 299 (1965).

13. A.Y.C. Yu and E.H. Snow, Solid-State Electron. 12, 155 (1969).

14. H.J. Hovel, "Solar Cells", Vol. 11 of Semiconductors and Semimetals, Edited by A.C. Beer and R.K. Willardson (Academic Press, New York, 1975) Chapter 6.

15. W.A. Anderson, A.E. Delahoy and R.A. Milano, J. Appl. Phys. 45, 3913 (1974).

16. M.A. Green, F.D. King and J. Shewchun, Solid-State Electron. 17, 551 (1974).

17. M.A. Green and J. Shewchun, Solid-State Electron. 17, 349 (1974).

18. A.M. Goodman and J.M. Breece, J. Electrochem. Soc. 117, 982 (1970).

19. For a review of experimental research on the MIS junction, see D.L. Pulfrey, IEEE Trans. Electron Dev. ED-25, 1308 (1978), and also Ref. 79.

20. N.G. Tarr and D.L. Pulfrey, Appl. Phys. Lett. 34, 295 (1979).

21. N.G. Tarr, D.L. Pulfrey and P.A. Iles, Appl. Phys. Lett. 35, 258 (1979).

22. V.A.K. Temple, M.A. Green and J. Shewchun, J. Appl. Phys. 45, 4934 (1974).

23. J. Shewchun and M.A. Green, J. Appl. Phys. 46, 5179 (1975).

24. M.A. Green and J. Shewchun, J. Appl. Phys. 46, 5185 (1975).

25. J. Shewchun, R. Singh and M.A. Green, J. Appl. Phys. 48, 765 (1976).

26. H.C. Card and E.H. Rhoderick, J. Phys. D4, 1589 (1971).

27. H.C. Card and E.H. Rhoderick, Solid-State Electron. 16, 365 (1973).

28. H.C. Card, Solid-State Electron. 20, 971 (1977).

29. See, for example, M.B. Prince, J. Appl. Phys. 26, 534 (1955); P. Rappaport, RCA Review 20, 373 (1959); and M. Wolf, Proc. IEEE 51, 674 (1963).

30. R.L. Cummerow, Phys. Rev. 95, 16 (1954).

31. F.A. Lindholm, J.G. Fossum and E.L. Burgess, IEEE Trans. Electron Dev. ED-26, 165 (1979); also F.A. Lindholm, J.G. Fossum and E.L. Burgess, Proc. 12th IEEE Photovoltaic Spec. Conf., op. cit., p. 33.

32. N.G. Tarr and D.L. Pulfrey, Solid-State Electron. 22, 265 (1979).

33. N.G. Tarr and D.L. Pulfrey, IEEE Trans. Electron Dev. ED-27, 771 (1980).

34. C.A. Mead, in Ohmic Contacts to Semiconductors, Edited by B. Schwartz (Electrochemical Society, New York, 1969) p. 3.

35. M.A. Green, R.B. Godfrey and L.W. Davies, Proc. 12th IEEE Photovoltaic Spec. Conf., op. cit., p. 896.

36. M.A. Green and R.B. Godfrey, Proceedings of the 1st CEC Photovoltaic Solar Energy Conference (D. Reidel, Dordrecht, Holland, 1977) p. 299.

37. N.G. Tarr, D.L. Pulfrey and P.A. Iles, J. Appl. Phys. 51, 3926 (1980).

38. See D.L. Pulfrey, Photovoltaic Power Generation, op. cit., pp. 18-20 and references listed therin.

39. H.J. Hovel, "Solar Cells", op. cit., Chapter 2.

40. S.M. Sze, Physics of Semiconductor Devices (Wiley, New York, 1969) p. 54.

41. A. Rothwarf, Proc. 13th IEEE Photovoltaic Spec. Conf. (IEEE, New York, 1978) p. 1312.

42. H.J. Hovel, "Solar Cells", op. cit., p. 57.

43. R. Sahai, D.D. Edwall and J.S. Harris, Proc. 13th IEEE Photovoltaic Spec. Conf., op. cit., p. 946.

44. W. Shockley, Bell System Tech. J. 28, 435 (1949).

45. S.M. Sze, Physics of Semiconductor Devices, op. cit., pp. 65-66.

46. R.J. Handy, Solid-State Electron. 10, 765 (1967).

47. A.S. Grove, Physics and Technology of Semiconductor Devices (Wiley, New York, 1967) Chapter 5.

48. M. Wolf, Proc. IEEE 51, 674 (1963).

49. A.S. Grove, Physics and Technology of Semiconductor Devices, op. cit., p. 184.

50. A.S. Grove, ibid., pp. 186-189.

51. T.I. Seidman and S.C. Choo, Solid-State Electron. 15, 1229 (1972).

52. H.J. Hovel, "Solar Cells", op. cit., pp. 188-190.

53. J.G. Fossum, F.A. Lindholm and M.A. Shibib, IEEE Trans. Electron Dev. ED-26, 1294 (1979).

54. H.J. Hovel and J.M. Woodall, Proc. 12th IEEE Photovoltaic Spec. Conf., op. cit., p. 945.

55. J.C.C. Fan, G.W. Turner, R.P. Gale and C.O. Bozler, Proc. 14th IEEE Photovoltaic Spec. Conf., op. cit., p. 1102.

56. M.P. Godlewski, H.W. Brandhorst and C.R. Baraona, Proc. 11th IEEE Photovoltaic Spec. Conf. (IEEE, New York, 1975) p. 32.

57. P.A. Iles and S.I. Soclof, Proc. 11th IEEE Photovoltaic Spec. Conf., op. cit., p. 19.

58. P.A. Iles, Proc. 8th IEEE Photovoltaic Spec. Conf. (IEEE, New York, 1970) p. 345.

59. J. Mandelkorn and J.H. Lamneck, Proc. 9th IEEE Photovoltaic Spec. Conf. (IEEE, New York, 1972) p. 66.

60. J.R. Hauser and P.M. Dunbar, Solid-State Electron. 18, 715 (1975).

61. M.P. Godlewski, C.R. Baraona and H.W. Brandhorst, Proc. 10th IEEE Photovoltaic Spec. Conf. (IEEE, New York, 1973) p. 40.

62. J.G. Fossum, IEEE Trans. Electron Dev. ED-24, 322 (1977).

63. K. Rajkanan, R. Singh and J. Shewchun, IEEE Trans. Electron Dev. ED-27, 250 (1980).

64. E.H. Rhoderick, J. Phys. D3, 1153 (1970).

65. W. Schottky, Naturwiss. 26, 843 (1938).

66. J. Bardeen, Phys. Rev. 71, 717 (1947).

67. S.M. Sze, Physics of Semiconductor Devices, op. cit., Chapter 6.

68. See, for example, J. Shewchun, M.A. Green and F.D. King, Solid-State Electron. 17, 563 (1974).

69. J. Ziman, Principles of the Theory of Solids, Second Edition (Cambridge University Press, 1972) Chapters 6, 7.

70. J. Ziman, Electrons and Phonons (Oxford University Press, New York, 1960) pp. 92-95.

71. J. Bardeen, Phys. Rev. Letters 6, 57 (1961).

72. W.A. Harrison, Phys. Rev. 123, 85 (1961).

73. C.B. Duke, "Theory of Metal-Barrier-Metal Tunneling", in Tunneling Phenomena in Solids, Edited by E. Burstein and S. Lundqvist (Plenum, New York, 1969) p. 31.

74. C.B. Duke, Tunneling in Solids (Academic Press, New York, 1969) pp. 25 et seq.

75. L.I. Schiff, Quantum Mechanics, Third Edition (McGraw-Hill, New York, 1968) pp. 101 et seq.

76. D.J. BenDaniel and C.B. Duke, Phys. Rev. 152, 683 (1966).

77. L.I. Schiff, Quantum Mechanics, op. cit., pp. 268 et seq.

78. L.D. Landau and E.M. Lifshitz, Quantum Mechanics (Pergamon Press, Oxford, 1965) pp. 171-175.

79. H.C. Card, "Tunnelling MIS Structures", Inst. Phys. Conf. Ser. 50 (1980) p. 140.

80. W. Franz, in Handbuch der Physik, Edited by S. Flugge, Vol. XVII (Springer Verlag, Berlin, 1956) p. 155.

81. Considerable controversy exists regarding the composition not only of ultra-thin silicon oxide layers, but also of the silicon/silicon oxide boundary layer in thick thermally grown oxides. An extensive and growing literature exists on this subject. See, for example, J.S. Johannesson, W.E. Spicer and Y.E. Strauser, J. Appl. Phys. 47, 3028 (1976); E. Taft and L. Cordes, J. Electrochem. Soc. 126, 131 (1979); and R. Flitsch and S.I. Raider, J. Vac. Sci. Technol. 12, 305 (1975).

82. O. Madelung, Introduction to Solid-State Theory (Springer Verlag, Berlin, 1978) Chapter 10.

83. C.R. Crowell and S.M. Sze, J. Appl. Phys. 37, 2683 (1966).

84. N.W. Ashcroft and N.D. Mermin, Solid State Physics (Holt, Reinhart and Winston, New York, 1976) p. 568.

85. C.R. Crowell, Solid-State Electron. 8, 395 (1965).

86. E.H. Rhoderick, J. Phys. D5, 1920 (1972).

87. E.H. Rhoderick, Metal-Semiconductor Contacts, op. cit., p. 87.

88. E.H. Rhoderick, Ibid., Chapter 3.

89. E.H. Rhoderick, "Transport Processes in Schottky Diodes", Inst. Phys. Conf. Ser. 22 (1974) p. 3.

90. C.R. Crowell and S.M. Sze, Solid-State Electron. 9, 1035 (1966).

91. A.Y.C. Yu, IEEE Spectrum 7, 83 (1970).

92. S.M. Sze, Physics of Semiconductor Devices, op. cit., p. 431.

93. H.J. Hovel, J. Appl. Phys. 47, 4968 (1976).

94. W.A. Anderson, A.E. Delahoy, J.K. Kim, S.H. Hyland and S.K. Dey, Appl. Phys. Lett. 33, 588 (1978).

95. R.B. Godfrey and M.A. Green, Appl. Phys. Lett. 34, 790 (1979).

96. R.B. Godfrey and M.A. Green, IEEE Trans. Electron Dev. ED-27, 737 (1980).

97. R.E. Thomas, C.E. Norman and R.B. North, Proc. 14th IEEE Photovoltaic Spec. Conf., op. cit., p. 1350.

98. M.A. Green and R.B. Godfrey, Appl. Phys. Lett. 29, 610 (1976).

99. M.A. Green, J. Appl. Phys. 47, 547 (1976).

100. H.J. Hovel, "Solar Cells", op. cit., pp. 62-63.

101. a) R.C. Jaklevic, D.K. Donald, J. Lambe and W.C. Vassell, Appl. Phys. Lett. 2, 7 (1963).
b) For a complete list of publications in this area, see Ref. 79.

102. H.C. Card and E.H. Rhoderick, J. Phys. D4, 1602 (1971).

103. J.A. St.Pierre, R. Singh, J. Shewchun and J.J. Loferski, Proc. 12th IEEE Photovoltaic Spec. Conf., op. cit., p. 847.

104. D.L. Pulfrey, Solid-State Electron. 20, 455 (1977).

105. N.W. Ashcroft and N.D. Mermin, Solid State Physics, op. cit., p. 575.

106. G.G. Macfarlane, J.P. McLean, J.E. Quarrington and V. Roberts, Phys. Rev. 111, 1245 (1958).

107. J.W. Slotboom and H.C. DeGraaf, Solid-State Electron. 19, 857 (1976).

108. S.M. Sze, Physics of Semiconductor Devices, op. cit., p. 39.

109. S.M. Sze, ibid., p. 48.

110. J.M. Feldman, The Physics and Circuit Properties of Transistors (Wiley, New York, 1972) pp. 331-335.

111. S.M. Vernon and W.A. Anderson, Appl. Phys. Lett. 26, 707 (1975).

112. M.A. Green and R.B. Godfrey, unpublished data.

113. S.M. Sze, op. cit., p. 366.

114. B.E. Deal, M. Sklar, A.S. Grove and D.H. Snow, J. Electrochem. Soc. 114, 266 (1967).

115. M.G. Coleman, R.A. Pryor and F.G. Sparks, Proc. 14th IEEE Photovoltaic Spec. Conf., op. cit., p. 793.

116. H.K. Gummel, IEEE Trans. Electron Dev. ED-11, 455 (1964).

117. A. DeMari, Solid-State Electron 11, 33 (1968).

118. V. Arandjelovic, Solid-State Electron. 13, 865 (1970).

119. S.C. Choo, IEEE Trans. Electron Dev. ED-19, 954 (1972).

120. M.S. Mock, Solid-State Electron. 15, 1 (1972).

121. E.D. Graham and J.R. Hauser, Solid-State Electron. 15, 303 (1972).

122. P. Ashburn, D.V. Morgan and M.J. Howers, Solid-State Electron. 18, 569 (1975).

123. P.M. Dunbar and J.R. Hauser, Solid-State Electron. 19, 95 (1976).

124. W. Shockley and W.T. Read, Phys. Rev. 87, 835 (1952).

125. R.A. Smith, Semiconductors, Second Edition (Cambridge University Press, New York, 1978) pp. 264-270.

126. E. Isaacson and H.B. Keller, Analysis of Numerical Methods, (Wiley, New York, 1966) p. 55.

127. S.M. Sze, Physics of Semiconductor Devices, op. cit., p. 40.

128. J.G. Fossum, Solid-State Electron. 19, 269 (1976).

129. H.J. Hovel, "Solar Cells", op. cit., p. 28.

130. A.J. Milnes and D.L. Feucht, Heterojunctions and Metal-Semiconductor Junctions (Academic Press, New York, 1975) p. 130.

131. International Commission on Illumination, CIE No. 20 (TC-2.2), Bureau Central de la CIE (Paris, 1972).

132. W. Kern, RCA Review 31, 187 (1970).

133. Evaporation Data Sheet, Sylvania Emissive Products, GTE Sylvania, Exeter, New Hampshire.

134. C.F. Gay, Proc. 13th IEEE Photovoltaic Spec. Conf., op. cit., p. 447.

135. J.G. Fossum and E.L. Burgess, Appl. Phys. Lett. 33, 238 (1978).

136. D.L. Pulfrey, IEEE Trans. Electron Dev. ED-23, 587 (1976).

137. M. Wolf and H. Rauschenbach, Advanced Energy Conversion 3, 455 (1963).

138. H.W. Brandhorst, Proc. 1st CEC Photovoltaic Solar Energy Conf., op. cit., p. 745.